CREEP DAMAGE AND FRACTURE MECHANICS OF HIGH TEMPERATURE MATERIALS

A Dissertation

Presented to the Faculty of the Graduate School

of Cornell University

In Partial Fulfillment of the Requirements for the Degree of

Doctor of Philosophy

by

Jing Ning

January 2013

CREEP DAMAGE AND FRACTURE MECHANICS OF HIGH TEMPERATURE MATERIALS

Jing Ning, Ph. D.

Cornell University 2013

This dissertation studies the deformation behavior of high temperature alloys with an aim to understand creep damage and fracture mechanics of these materials. First, we study the creep fatigue deformation of a unified viscoplastic material subjected to uniaxial cyclic loading using a dynamical system approach. We find oscillation of back stress significantly increases the inelastic strain accumulation in a cyclic test. The accumulated inelastic strain at long times are sensitive to the initial condition (e.g. whether one starts with tension or compression). We define a ratcheting ratio to quantify the interaction of creep and cyclic plasticity on the accumulated inelastic strain per cycle.

The second part of the dissertation focuses on solving the asymptotic stress and strain field near the tip of a plane strain Mode I stationary crack in a viscoplastic material. For small scale creep where the region of inelasticity is small in comparison with typical specimen dimensions, our asymptotic and finite element analysis show that the near tip stress field has the same singularity as elastic power law creeping materials with a time dependent amplitude. This amplitude is found to vanish at long times and the elastic K field dominates. For the case of cyclic loading, we study the effect of stress ratio on inelastic strain and find that the strain accumulated per cycle decreases with stress ratio.

The third part of the dissertation carries out finite element simulations on the planar deformation of random sized power law creeping grains with sliding and cavitating boundaries. Grain boundary sliding and grain boundary separation due to cavity nucleation and growth are incorporated into a cohesive zone model. Finite element simulation of a relaxation test shows that more grain boundary separation occurs in a microstructure with sliding resistant grain boundaries than in a microstructure with more freely sliding grain boundaries. The overall inelastic strain rate of the microstructure in uniaxial tension test is found to be greatly enhanced by grain boundary sliding and grain boundary cavitation.

Finally, we extend the cohesive zone model in the third part of the dissertation to account for interface embrittlement caused by grain boundary impurities. Finite element simulation of an uniaxial creep test using a two dimensional random grain structure shows that grain boundary cavitation and interface embrittlement are two competing mechanisms for grain boundary separation. The occurrence of one grain boundary separation mode would slow down or even inhibit the other.

BIOGRAPHICAL SKETCH

Jing Ning was born on January 24th 1985 in Jinzhou, Hebei Province in the People's Republic of China. She attended Northeastern University at Shenyang from 2002 to 2006 for her undergraduate study. Then she entered Tsinghua University in August 2006 and graduated with a M.S. degree in Mechanical Engineering in July 2008. She enrolled in Sibley School of Mechanical and Aerospace Engineering at Cornell University in August 2008 and defended her Ph.D. dissertation on December 6th, 2012.

To My Father, Mother, Brother and Sister

ACKNOWLEDGMENTS

I came to Cornell four and half years ago to pursue my PhD and it is hard to believe that I have finally come to this end. I've grown so much both personally and academically over my time here. The most vital person to this process is my advisor Chung Yuen Hui. I would like to thank him for his guidance during my dissertation work. None of this would have been possible without his help. On top of the specific academic skills he taught me, his passion and dedication to research, his patience for teaching made him the best advisor I could ever have. I am forever grateful to him for not only being a truly great advisor but also someone who cares greatly about his students and in this way I was very fortunate to have him at Cornell.

I would also like to thank my special committee members Leigh Phenix and Anthony Ingraffea for spending some of their precious time on me and making really useful suggestions on my research. I am very grateful to Professor Ingraffea for generously sharing the codes from his research group and to his student Albert Cerrone for the help with debugging and modifying the code.

I am very fortunate to have worked with Dr. Sam Sham at Oak Ridge National lab on a Department of Energy project which had funded me throughout the years. Numerous detailed discussions with Dr. Sham have greatly helped with the ultimate success of the project and it is deeply appreciated. My gratitude also extends to Professor Yanfei Gao at University of Tennessee who has helped this project with his expertise on micro-mechanical modeling.

Our research group provides a very good environment to exchange ideas and I consider myself very lucky to have worked and become friends with these pleasant people: Rong Long, Nichole Nadermann, Snow Xu, Abhishek Srivastava, Xinzeng Feng. I also want to thank Rong Long in particular for his insightful suggestions.

I have truly enjoyed my time at Cornell over the past four and half years and I have been fortunate to make many great friends who have helped me grow in so many ways. Special thanks go out to Boram Kim and Xiao Wang, whose unconditional support helped me go through all the difficult times. And I would always remember the time we spent together.

Above all, I would like to express my deepest gratitude to my family for their endless love and support over the years: to my sister who has always helped me; to my brother who has grown into a mature independent young man; finally to my mother and father, who have always trusted and believed in me.

TABLE OF CONTENTS

LIST OF FIGURES

LIST OF TABLES

LIST OF ABBREVIATIONS

FEM . . . . . Finite Element Method

CZM . . . . . Cohesive Zone Model

UVM . . . . . Unified Viscoplastic Model

RVE . . . . . Representative Volume Element

UEL . . . . . User Element Subroutine

PBC . . . . . Periodic Boundary Condition

GB . . . . . Grain Boundary

CHAPTER 1

INTRODUCTION

Creep rupture and fracture of high temperature materials has been a very active research topic due to its great importance in the aerospace and energy industry (see Figure 1.1). For example, the fatigue life of jet engine turbine blades depends on the creep and cyclic loading behavior of Nickel-based single crystals (Pierce 2009). Alloy 617, commonly used in the power plant components such as intermediate heat exchangers, may fail because of cavity nucleation and coalescence along grain boundaries (Rao et al. 1996).

Time dependent deformation or creep becomes a dominant deformation mechanism at temperatures above 1/3 of the melting temperature of most structural metals. Typical high temperature structural components are subjected to both monotonic and cyclic loadings at low stresses. The accumulation of creep strain cause material damage and creep-fatigue interaction often accelerates this process. In order to quantify the deformation and stress fields in structural components under cyclic loading, it is necessary to use visco-plastic constitutive models that are described in chapter 2 of this dissertation. For example, creep curves of Alloy 617 do not show the typical primary-secondary-tertiary creep regimes commonly observed in metals and they do not exhibit clear distinction between time-independent plasticity and time-dependent creep (Chomette et al. 2010; Schubert et al. 1984; Cook 1984; Schneider et al. 1984; Kurata and Nakajima 1995; Natesan et al. 2003; Shah et al. 2003). A more accurate way to describe the creep behavior of such materials is to use a unified viscoplastic model (UVM) where stress relaxation, ratcheting and cyclic softening/hardening behavior can be captured by state variables. Despite the success of UVM to represent high temperature material behavior, most of these models have

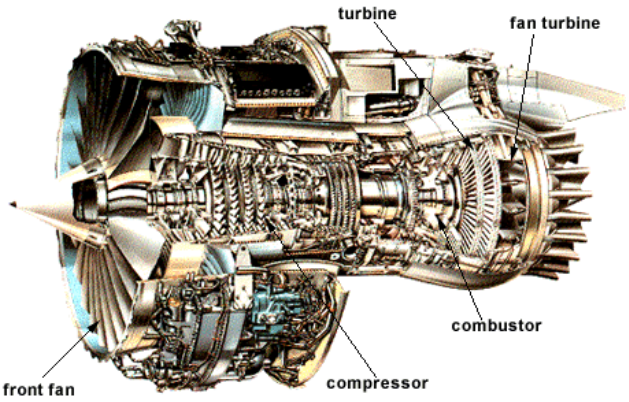

(a) aircraft jet engines (PilotFriend_Aero_Engines)

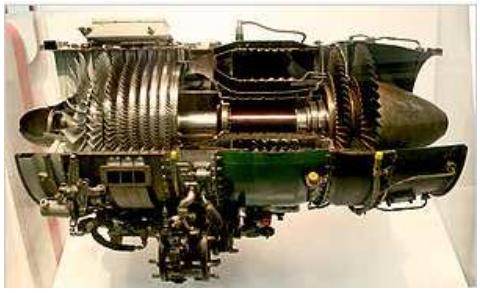

(b) industrial gas turbines (Wikipedia_Gas_turbine)

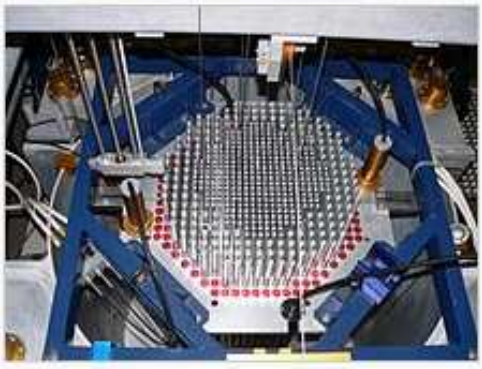

(c) nuclear reactors (Wikipedia_Nuclear_reactor)

Figure 1.1 High temperature material applications.

very complex mathematical structures. In chapter 2, we use a dynamical system approach to study the qualitative behavior of a specific unified viscoplastic model in a creep fatigue test. This approach will allow future investigators to gain insight into the interaction of creep and cyclic plasticity.

Cracks can initiate from defects near stress concentrators and propagate due to fatigue and creep at low applied stresses. Unlike structural components operating at low temperatures, the deformation near the crack tip depends on the stress history. The asymptotic strength of the crack tip stress field can be quantified by a time dependent loading parameter which can be used to correlate crack growth rate with applied load in complex structures. Most of the crack tip analyses in the literature are based on an elastic power law creeping (EPLC) solid (Hutchinson 1968; Rice and Rosengren 1968). In Chapter 3 of this dissertation, we determine the asymptotic stress and strain field near the tip of a plane strain Mode I stationary crack using a unified viscoplastic model due to Chaboche (1989). We address the long term creep behavior of the asymptotic fields in the regime of small scale creep. We also study the time dependent behavior of these crack tip fields under cyclic loading conditions in a single edge crack specimen.

A different mode of failure is creep rupture where materials fail by progressive damage instead of slow propagation of a macroscopic crack. Many power plants structural components are designed to last over 60 years. It is extremely difficult to conduct creep experiments for such long periods of time. Current approach is to extrapolate short-term, high stress creep rupture experimental data to long-term, low stress conditions and predict the creep rupture life of a component. Such extrapolation typically used empirically based time-temperature parameters even though the failure mechanisms in short term and long term tests can be very different. For example, the dominating failure mechanism for ferritic and austenitic steels at low stresses and

elevated temperatures is intergranular cavitation whereas at relatively lower temperature with impurity segregation, the dominating failure mechanism is transgranular brittle fracture (White et al. 1981; McMahon Jr 1968). In the low stress regime, cavities nucleate on grain boundaries that are under normal tension, and these cavities grow by grain boundary sliding (Evans 1971), stress-assisted diffusion of atoms from cavity surface to the grain boundaries (Hull and Rimmer 1959; Chuang et al. 1979b; Needleman and Rice 1980), and by creep deformation of the surrounding grains (Hancock 1976; Budiansky et al. 1982). Our ultimate goal is to develop a numerical model based on these well-established micro-mechanics of local failure to predict long time creep behavior. Previous works have incorporated some of these failure mechanisms into a finite element model consisting of periodic arrays of hexagonal grains. In chapter 4 of this dissertation, we extend these works to a random grain structure. The grain boundaries in our model can slide and separate due to cavity nucleation and growth. The nucleation and growth of cavities on a grain boundary can be represented by a cohesive zone model with two time dependent state variables. We carried out simulations using the cohesive zone model to study the creep rupture of random sized power law creeping grains with sliding and cavitating boundaries.

Chapter 5 extends the cohesive zone model in Chapter 4 to account for grain boundary decohesion due to interface embrittlement. Most high temperature materials contain impurities such as second phase particles to inhibit creep. Over time, these particles can segregate to the grain boundaries and lower the creep rupture resistance of these materials. In this chapter, we propose a phenomenological model for grain boundary embrittlement. We incorporate this embrittlement model into our finite element code to study the interaction of embrittlement and deformation caused by creep, cavities growth and grain boundary sliding.

Chapter 6 discusses the limitations of our approach and possible future work.

REFERENCES

Budiansky B, Hutchinson J, Slutsky S (1982) Void growth and collapse in viscous solids. Mech Solids:13-45

Chaboche JL (1989) Constitutive equations for cyclic plasticity and cyclic viscoplasticity. Int J Plast 5:247-302

Chomette S, Gentzbittel JM, Viguier B (2010) Creep behaviour of as received, aged and cold worked Inconel 617 at 850° C and 950° C. J Nucl Mater 399:266-274

Chuang TJ, Kagawa KI, Rice JR, Sills LB (1979) Overview no. 2: non-equilibrium models for diffusive cavitation of grain interfaces. Acta Metall 27:265-284

Cook R (1984) Creep properties of Inconel-617 in air and helium at 800 to 1000° C. Nucl Technol 66:283-288

Evans H (1971) The growth of creep cavities by grain boundary sliding. Philos Mag 23:1101-1112

Hancock J (1976) Creep cavitation without a vacancy flux. Met Sci 10:319-325

Hull D, Rimmer D (1959) The growth of grain-boundary voids under stress. Philos Mag 4:673-687

Hutchinson J (1968) Singular behaviour at the end of a tensile crack in a hardening material. J Mech Phys Solids 16:13-31

Kurata Y, Nakajima H (1995) Temperature dependence of creep properties of cold-worked Hastelloy XR. J Nucl Sci Technol 32:539-546

McMahon Jr C Temper Brittleness-An Interpretive Review. In: Temper Embrittlement of Steel , ASTM STP 407, Philadelphia, 1968. pp 127-167

Natesan K, Purohit A, Tam S (2003) Materials Behavior in HTGR Environments. Office of Nuclear Regulatory Research, Washington.

Needleman A, Rice J (1980) Plastic creep flow effects in the diffusive cavitation of grain boundaries. Acta Metall 28:1315-1332

Pierce CJ (2009) Creep and Fatigue Interaction Characteristics of PWA1484. DTIC Document,

PilotFriend_Aero_Engines. http://www.pilotfriend.com/aero_engines/aero_jet.htm

Rao KBS, Schuster H, Halford G (1996) Mechanisms of high-temperature fatigue failure in alloy 800H. Metallurgical and Materials Transactions A 27:851-861

Rice J, Rosengren G (1968) Plane strain deformation near a crack tip in a power-law hardening material. J Mech Phys Solids 16:1-12

Schneider K, Hartnagel W, Iischner B, Schepp P (1984) Creep behavior of materials for high-temperature reactor application. Nucl Technol 66:289-295

Schubert F, te Heesen E, Bruch U, Cook R, Diehl H, Ennis P, Jakobeit W, Penkalla H, Ullrich G (1984) Creep rupture behavior of candidate materials for nuclear process heat applications. Nucl Technol 66:227-240

Shah VN, Majumdar S, Natesan K, Technology UNRCOoNRRDoE (2003) Review and assessment of codes and procedures for HTGR components. Division of Engineering Technology, Office of Nuclear Regulatory Research, US Nuclear Regulatory Commission,Argonne National Laboratory,

White C, Padgett R, Swindeman R (1981) Sulfur and phosphorus segregation to creep cavities and grain boundaries in 304 SS. Scr Metall;(United States) 15

Wikipedia_Gas_turbine. http://en.wikipedia.org/wiki/Gas_turbine

Wikipedia_ Nuclear_reactors: http://en.wikipedia.org/wiki/Nuclear_reactor

CHAPTER 2

ANALYSIS OF CREEP FATIGUE BEHAVIOR OF A UNIFIED VISCOPLASITC MODEL

2.1 Introduction

A primary candidate for the next generation nuclear plant is a gas cooled reactor which uses helium as a heat transfer medium at temperatures up to 950^{o}C and pressures up to 7 MPa for a design life of 60 years (Guerin et al. 2009; Lee et al. 2010; Mo et al. 2011; Shah et al. 2003). A core component in the primary reactor circuit is the intermediate heat exchanger (IHX) which transfers heat from the primary reactor helium to a working fluid at a lower temperature. The leading candidate material for the IHX is Alloy 617, which is a solid-solution strengthened nickel based alloy with excellent high temperature strength and oxidation resistance (Ren and Swimdeman 2009; Shah et al. 2003).

Nickel based alloys exhibit complex deformation behavior, for example, creep curves of Alloy 617 do not show the typical primary-secondary-tertiary creep regimes commonly observed in metals and they do not exhibit clear distinction between time-independent plasticity and time-dependent creep (Chomette et al. 2010; Schubert et al. 1984; Cook 1984; Schneider et al. 1984; Kurata and Nakajima 1995; Natesan et al. 2003; Shah et al. 2003). However, current high temperature design procedures under creep or creep fatigue conditions mostly use the elastic-power-law-creep (EPLC) model or a model in which the inelastic strain is the sum of a rate independent plastic strain and rate dependent creep strain to represent material data (Wakai et al. 2002; Drubay et al. 2003; Yoon et al. 1992; Adefris et al. 1996a; Grover and Saxena 1999). As mentioned above, power law or secondary creep is not representative of the

deformation behavior of nickel based alloys; and in addition, does not model cyclic loading well. A growing body of research has demonstrated that much of the complex deformation behavior of super alloys, such as stress relaxation, ratcheting and cyclic softening/hardening behavior, can be captured by state variable models, commonly called unified viscoplastic models (UVM) (Bodner and Partom 1975; Miller 1976; Walker 1981; Chaboche and Rousselier 1983; Krempl 1987) where there is no separation between creep and plasticity.

A disadvantage of UVM is that they have very complex mathematical structures. In a typical model, a large number of material constants and coupled nonlinear differential equations are needed to describe the evolution of the state variables. As a result, existing work in this area tends to focus on either developing better models to fit experimental data or numerically solving these equations using a particular set of material constants appropriate for a specific engineering application or test. Instead of focusing on a specific application, we study and gain insight into the qualitative behavior of a viscoplastic model subjected to a simple class of cyclic loading in this chapter. Specifically, we use a simplified version of a UVM developed by Chaboche (1989) and model a load controlled creep fatigue test where the applied stress history $\sigma_{22}(t)$ is illustrated in Figure 2.1. As shown in the figure, the loading and unloading rates are assumed to be sufficiently fast with respect to other time scales in the problem so they are considered as instantaneous. Thus, the loading waveform is a piece-wise constant periodic function of time. In a cycle with period t_c, the applied stress σ oscillates between the maximum $\sigma_{max} > 0$ and the minimum stress σ_{min}. σ_{min} can be either positive (tension) or negative (compression). Each cycle consists of two hold times: peak stress ($\sigma = \sigma_{max}$) hold time t_1 and valley stress ($\sigma = \sigma_{min}$) hold time $t_2 = t_c - t_1 > 0$.

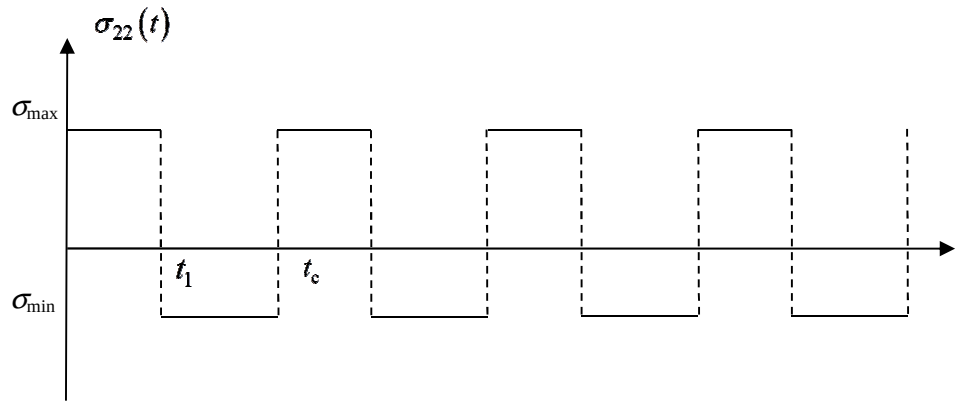

Figure 2.1 Schematics of a load controlled cyclic fatigue test.

We address the following questions in this chapter:

(1) If the system (bar) is driven by a periodic input shown in Figure 2.1, does there always exist a long time solution where the back stress approach steady state values or will the back stress exhibit oscillatory behavior? Using a dynamical system approach, we establish conditions for solutions with the different long time back stress behaviors.

(2) Does the long time inelastic strain depend on the initial conditions? For example, if the waveform in Figure 2.1 is shifted to the left by t_1 so that the specimen is subjected to compression (i.e., $\sigma(t=0^+)=\sigma_{\min}<0$) first instead of tension, will this lead to different long time inelastic strain? If this is the case, then the system is said to have long term memory.

(3) How does the ratcheting strain depends on the loading cycle (stress amplitude, frequency, hold period, etc.) and the material parameters?

2.2 UVM Equations Analysis in Uniaxial Test

The following version of UVM was developed by Chaboche (1989) and later used by Zhao and Tong and their group (Zhao and Tong 2008; Zhan and Tong 2007a, b) to study the effect of cyclic loads on a cracked specimen. The total strain rate $\dot{\varepsilon}_{ij}$ is the sum of the elastic and inelastic strain rate. The elastic strain rate $\dot{\varepsilon}_{ij}^{\mathrm{e}}$ is given by

$$\dot{\varepsilon}_{ij}^{\mathrm{e}}=\frac{\dot{\sigma}_{ij}}{E}+\frac{1-\upsilon}{E}\dot{\sigma}_{kk}\delta_{ij} \tag{2.1}$$

where E is the Young's modulus and υ is the Poisson's ratio of the material, and a dot denotes differentiation with respect to time t. The inelastic strain rate $\dot{\varepsilon}_{ij}^{\mathrm{I}}$, is

$$\dot{\varepsilon}_{ij}^{\mathrm{I}}=\frac{3}{2}\dot{p}\frac{\omega_{ij}}{\omega_{\mathrm{e}}} \tag{2.2}$$

where

$$\omega_{ij} \equiv s_{ij} - x'_{ij} \tag{2.3}$$

In (2.3), s_{ij} and x'_{ij} are the deviatoric part of applied stress σ_{ij} and back stress x_{ij} respectively, $\omega_e = \sqrt{3\omega_{ij}\omega_{ij}/2}$ is the effective stress and $\dot{p}$ is the *effective* strain rate given by

$$\dot{p} = \langle f / Z \rangle^n \tag{2.4}$$

where Z and n are material constants and the symbol $\langle\ \rangle$ is defined by

$$\langle z \rangle = \begin{cases} z & z \geq 0 \\ 0 & z < 0 \end{cases} \tag{2.5}$$

In (2.4), f is the yield function defined by

$$f = \omega_e - r - k \tag{2.6}$$

where r is an isotropic hardening variable and k is the initial radius of the yield surface, i.e., the elastic region is defined by $f \leq 0$. The hardening variable r in (2.6) evolves according to

$$\dot{r} = c_3(r_\infty - r)\dot{p} \tag{2.7}$$

Finally, the back stress x_{ij} evolves according to:

$$\dot{x}_{ij} = \dot{\alpha}_{ij} + \dot{\beta}_{ij} \tag{2.8}$$

$$\dot{\alpha}_{ij} = c_1\left(a_1\frac{\omega_{ij}}{\omega_e} - \alpha_{ij}\right)\dot{p} \tag{2.9}$$

$$\dot{\beta}_{ij} = c_2\left(a_2\frac{\omega_{ij}}{\omega_e} - \beta_{ij}\right)\dot{p} \tag{2.10}$$

where $c_1, c_2, c_3, a_1, a_2, r_\infty$ are material constants.

According to (2.8-2.10), the evolution of the back stress x_{ij} is driven by the effective stress ω_{ij}. Since this tensor is deviatoric ($\omega_{ii} = 0$), x_{ij} is also deviatoric, i.e.,

$$x_{11} + x_{22} + x_{33} = 0 \tag{2.11}$$

For uniaxial loading, $\sigma_{22} = \sigma, \sigma_{11} = \sigma_{33} = 0$. Denote $x = x_{22}$, (2.11) implies that

$$x_{11} = x_{33} = -\frac{x}{2} \tag{2.12}$$

$$\omega_{11} = -\frac{\sigma}{3} + \frac{x}{2}, \omega_{22} = \frac{2\sigma}{3} - x, \omega_{33} = -\frac{\sigma}{3} + \frac{x}{2}, \omega_{\mathrm{e}} = \left|\sigma - \frac{3x}{2}\right| \tag{2.13}$$

Since the goal of this chapter is to understand qualitative behavior and suggest a different and complementary approach to the study of viscoplastic models, we simplify these equations by setting $c_2 = c_3 = 0$. Most of the qualitative behavior of these equations will not be affected by this assumption (see discussion in section 2.5). Using this assumption, and denoting $\dot{\varepsilon} = \dot{\varepsilon}^{\mathrm{I}}_{22}$, the governing equations reduce to:

$$\dot{p} = \left\langle \frac{|\sigma - 3x/2| - k}{Z} \right\rangle^n \tag{2.14}$$

$$\dot{\varepsilon} = \frac{3}{2}\dot{p}\frac{\omega_{22}}{\omega_{\mathrm{e}}} = \left\langle \frac{|\sigma - 3x/2| - k}{Z} \right\rangle^n \operatorname{sgn}\left(\sigma - \frac{3x}{2}\right) \tag{2.15}$$

$$\dot{x} = c_1\left(\frac{2}{3}a_1 \operatorname{sgn}\left(\sigma - \frac{3x}{2}\right) - x\right)\dot{p} \tag{2.16}$$

The *sgn* function in (2.15) and (2.16) is defined by

$$\operatorname{sgn} z = \begin{cases} 1 & z > 0 \\ -1 & z < 0 \\ 0 & z = 0 \end{cases} \tag{2.17}$$

It is important to note that the inelastic strain rate can be either positive or negative, depending on the sign of $\sigma - 3x/2$. However, the *effective* inelastic strain rate $\dot{p}$ is always non-negative.

2.2.1 Normalization

We introduce the following normalized variables to reduce the number of parameters in (2.14)-(2.16):

$$S = \sigma / a, X = x / a, K = k / a, \tau = t / \left(Z / a \right)^n \tag{2.18}$$

where $a = 2a_1 / 3$ is the saturation value of the back-stress in tension (see (2.16)). With respect to these normalized variables, the governing equations for a cyclic loading test become

$$d\varepsilon / d\tau = \operatorname{sgn}\left(S(\tau) - \frac{3}{2} X \right) dp / d\tau \tag{2.19}$$

$$dp / d\tau = \left\langle \left| S(\tau) - \frac{3}{2} X \right| - K \right\rangle^n \tag{2.20}$$

$$dX / d\tau = c \left(\operatorname{sgn}(S(\tau) - \frac{3}{2} X) - X \right) \left\langle \left| S(\tau) - \frac{3}{2} X \right| - K \right\rangle^n \tag{2.21}$$

where $c = c_1$. The inelastic strain evolves according to (2.19), the effective inelastic strain *p* is governed by (2.20) and the back stress evolves according to (2.21).

2.2.2 State Vector

Since $\dot{p} \geq 0$, the effective inelastic strain is a non-decreasing function of time, hence steady state solution for (2.14),(2.15),(2.16) does not exist. A simple way to by pass this difficulty is to define

$$\Delta\varepsilon_k \equiv \varepsilon_k - \varepsilon_{k-1} \qquad k = 1, 2... \tag{2.22}$$

where $\varepsilon_k = \varepsilon(k\tau_c)$ and $\Delta\varepsilon_k$ denotes the *increment* of inelastic strain between cycle *k* and cycle *k+1*. Similarly, we denote $X_k = X(k\tau_c)$ and define the state vector $\vec{y}_k$ by

$$\vec{y}_k = \begin{pmatrix} X_k \\ \Delta\varepsilon_k \end{pmatrix} \tag{2.23}$$

In this chapter, steady state solution means that the state vector $\vec{y}_k$ approaches a limiting vector $\vec{y}_\infty = \begin{pmatrix} X_\infty \\ \Delta\varepsilon_\infty \end{pmatrix}$ as $k \to \infty$.

2.2.3 Back Stress Evolution and Periodic Solutions

In this section we study the behavior of the long time solution of (2.19), (2.20) and (2.21) subjected to the waveform displayed in Figure 2.1. There are two types of long time behavior: (1) the normalized back stress increases monotonically to its saturation value of *1* (case 1 and 2 below); (2) the back stress is oscillatory and periodic (case 3 below).

Consider the case that the system (viscoplastic bar) starts with tension (as shown in Figure 2.1). Because of the yield function, the inelastic strain rate $dp/d\tau$ will be zero if the peak tension $S_{\max}$ is too small and this is obviously not an interesting case. To ensure non-zero inelastic strain rate during peak stress hold, we enforce the condition $S_{\max} > 3/2 + K$ (see (2.19)). Using this condition and combining (2.19) and (2.20), the equations governing the evolution of back stress and the inelastic strain during peak stress hold become

$$dX/d\tau = c(1-X)\left(S_{\max} - \frac{3}{2}X - K\right)^n \tag{2.24}$$

$$d\varepsilon/d\tau = \left(S_{\max} - \frac{3}{2}X - K\right)^n \tag{2.25}$$

Since initially $X(0) = 0$, the normalized back stress has absolute value less than 1, that is, $(1-X) > 0$ in(2.24). This implies that the back stress is monotonically increasing during *any* peak stress hold.

The question is how the back stress evolves during valley stress hold. Its evolution is governed by (2.21) with $S(\tau) = S_{\min}$. To gain insight, we first establish possible behaviors of the back stress during valley stress hold. There are three possibilities:

(1) $$\left|S_{\min} - \frac{3}{2}X(\tau)\right| - K \le 0 \tag{2.26}$$

(2) $$\left|S_{\min} - \frac{3}{2}X(\tau)\right| - K > 0,\ \operatorname{sgn}(S_{\min} - \frac{3}{2}X) > 0 \tag{2.27}$$

(3) $$\left|S_{\min}-\frac{3}{2}X(\tau)\right|-K>0,\ \ \mathrm{sgn}(S_{\min}-\frac{3}{2}X)<0 \tag{2.28}$$

Case I(2.26): The back stress and inelastic strain evolution is governed by:

$$\begin{aligned} dX/d\tau &= 0 \\ d\varepsilon/d\tau &= 0 \end{aligned} \tag{2.29}$$

For this case, the back-stress does not evolve and there is no strain accumulation during valley stress hold. However, since the back stress continues to increase during peak stress hold, it will eventually reach the steady state value of *1*. As a result, the long term inelastic strain rate is

$$\dot{\varepsilon}_{\infty}=\begin{cases}\left(S_{\max}-3/2-K\right)^{n} & \text{peak stress hold}\\ 0 & \text{valley stress hold}\end{cases} \tag{2.30}$$

The increment of inelastic strain per cycle at long times, $\Delta\varepsilon_{\infty}$, is

$$\Delta\varepsilon_{\infty}=\left(S_{\max}-3/2-K\right)^{n}\tau_1 \tag{2.31}$$

In summary, for $S_{\max}>3/2+K$ and $\left|S_{\min}-\frac{3}{2}\right|<K$, the steady state vector is

$$\vec{y}_{\infty}=\begin{pmatrix}1\\ \left(S_{\max}-3/2-K\right)^{n}\tau_1\end{pmatrix} \tag{2.32}$$

An example of case I where $(S_{\max}=2, S_{\min}=1.5, K=0.4, n=3, c=20, \tau_1=\tau_2=4)$ is shown Figure 2.2 (a),(b). Figure 2.2(a) plots the evolution of the back stress with time. The trajectory of the state vector near equilibrium, i.e., in the neighborhood of $\vec{y}_{\infty}$, is shown in Figure 2.2(b).

Case II (2.27): For this case, back stress and inelastic strain evolution is governed by

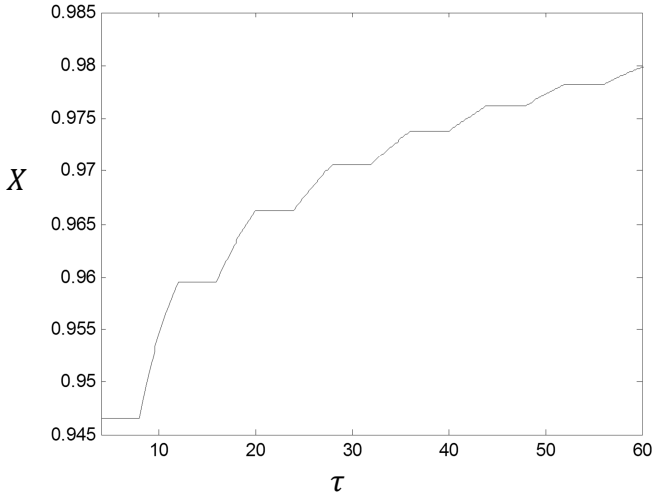

(a)

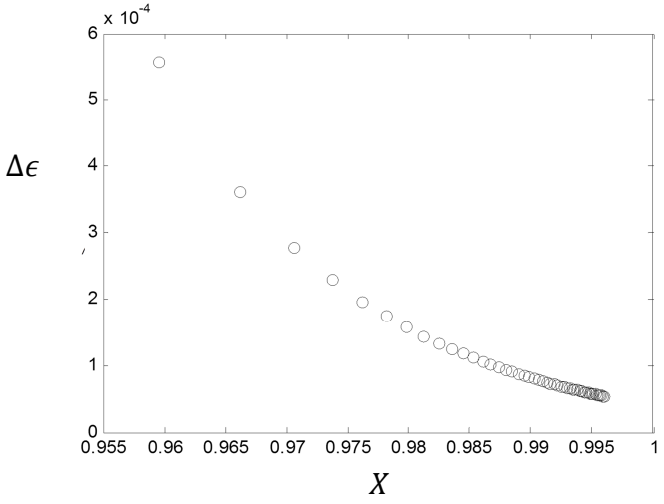

(b)

Figure 2.2 Example of case I with initial conditions $X(0) = \varepsilon(0) = 0$. (a) Back stress evolution (b) Trajectory of state vector

$$dX / d\tau = c(1-X)\left(S_{\min} - \frac{3}{2} X - K \right)^n$$
$$d\varepsilon / d\tau = \left(S_{\min} - \frac{3}{2} X - K \right)^n \tag{2.33}$$

Equation (2.33) implies that $dX / d\tau > 0$, hence the back-stress will continue to increase during valley stress hold. Eventually, it will approach its steady state value of 1. Therefore, the long time inelastic strain rate is

$$\dot{\varepsilon}_\infty = \begin{cases} \left(S_{\max} - 3/2 - K\right)^n & \text{peak stress hold} \\ \left(S_{\min} - 3/2 - K\right)^n & \text{valley stress hold} \end{cases} \tag{2.34}$$

Using (2.34), the long time state vector $\vec{y}_k$ is

$$\vec{y}_\infty = \begin{pmatrix} 1 \\ \left(S_{\max} - 3/2 - K\right)^n \tau_1 + \left(S_{\min} - 3/2 - K\right)^n \left(\tau_c - \tau_1\right) \end{pmatrix} \tag{2.35}$$

Note in Case II, the back stress and the inelastic strain are always increasing. These analytical results are verified by numerically integrating the governing equations for the case of $(S_{\max} = 2, S_{\min} = 1.8, K = 0.1, c = 300, n = 5, \tau_1 = \tau_2 = 0.01)$. As predicted by our analysis, Figure 2.4(a) shows that the back stress is increasing with time, that is, no oscillatory solution. Figure 2.4(b) shows the trajectory of the state vector near equilibrium, i.e., in the neighborhood of $\vec{y}_\infty$.

Case III (2.28): The back stress and inelastic strain behavior during valley stress hold is governed by

$$dX / d\tau = -c(1+X)\left(\frac{3}{2} X - S_{\min} - K \right)^n$$
$$d\varepsilon / d\tau = \left(\frac{3}{2} X - S_{\min} - K \right)^n \tag{2.36}$$

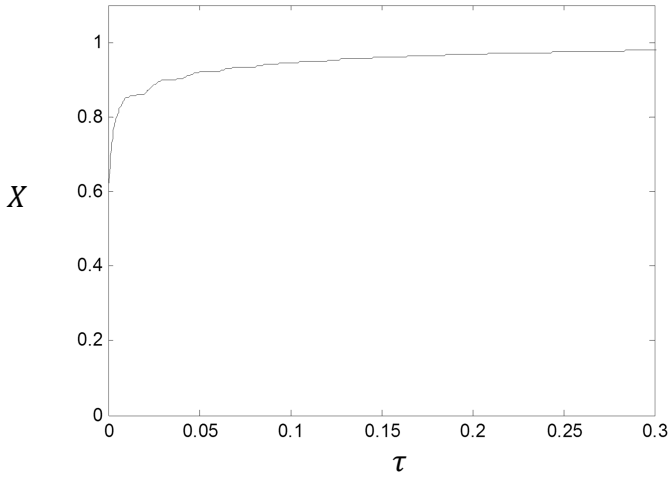

(a)

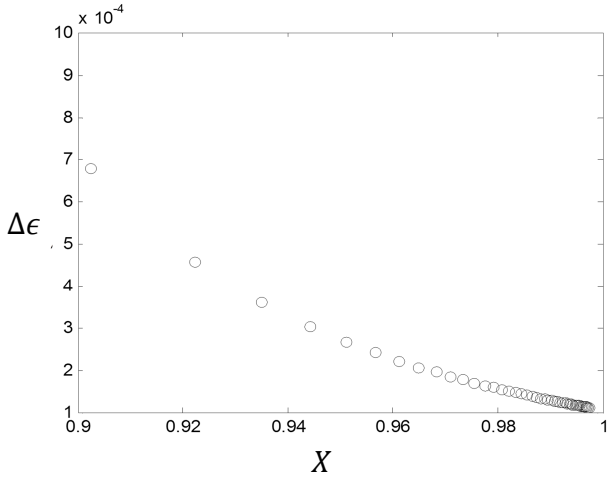

(b)

Figure 2.3 Example of case II with initial conditions $X(0) = \varepsilon(0) = 0$.(a) Back stress evolution (b) Trajectory of state vector

Equation (2.36) shows that the derivative of the back stress with time is negative, therefore the back stress decreases during valley stress hold. Since back stress increases during peak stress hold, the solution can be *oscillatory*. If this is the case, then the back-stress at long times will converge to a non-constant periodic function $X_\infty(\tau)$ with period τ_c

$$X_\infty(\tau+\tau_c) = X_\infty(\tau) \tag{2.37}$$

The periodic function $X_\infty(\tau)$ will oscillate between X_0 and X_1, where $0 \le X_0 \le X_1 \le 1$. In order for this situation to occur, $S_{\min}$ has to satisfy (2.28) during all valley stress hold, which can be rewritten as

$$S_{\min} < \frac{3}{2} X(\tau) - K \tag{2.38}$$

The periodicity of $X_\infty(\tau)$ implies that the increment of the inelastic strain per cycle is a constant, and is given by

$$\Delta\varepsilon_\infty = \int_0^{\tau_1} \left(\left| S_{\max} - \frac{3}{2} X_\infty(\tau) \right| - K \right)^n d\tau + \int_{\tau_1}^{\tau_c} \left(\left| S_{\min} - \frac{3}{2} X_\infty(\tau) \right| - K \right)^n d\tau \tag{2.39}$$

An example of this case ($S_{\max} = 1.7, S_{\min} = 0.1, K = 0.1, n = 5, c = 10, \tau_1 = \tau_2 = 0.01$) is shown in Figure 2.3.

Equations (2.24) and (2.33) suggest that the rate of convergence to the long time solution is governed by the material parameter *c*. The convergence rate of the state vector is shown in Figure 2.5 for several values of *c*. The numerical results show that long time periodic solution is reached after 3 cycles. Since the typical values of c are quite large, long time solution are reached after two or three cycles. Our numerical simulations show that rate of convergence is not particularly sensitive to parameters such as $n, \tau_1, \tau_c, K, S_{\min}, S_{\max}$.

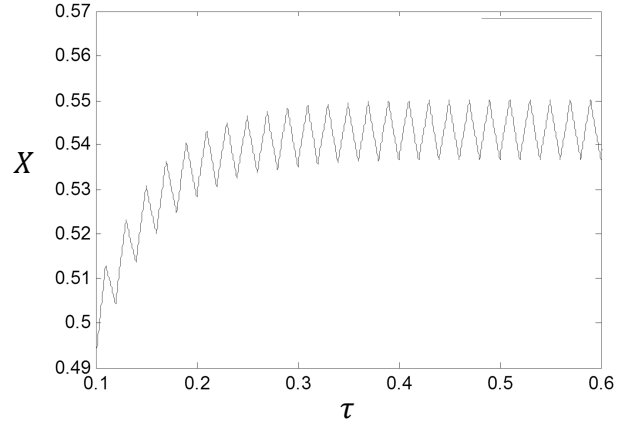

(a)

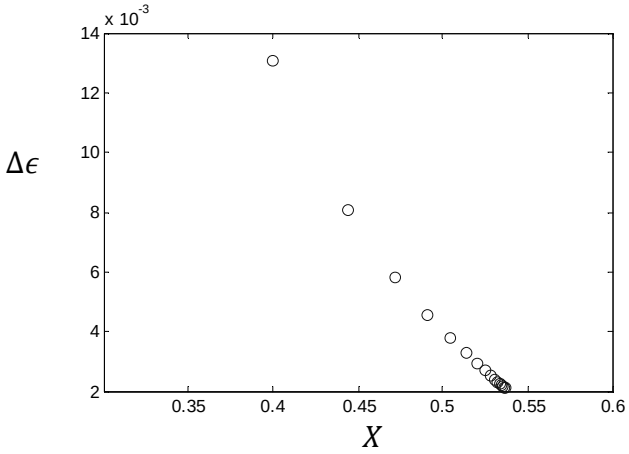

(b)

Figure 2.4 Example of case III with initial conditions $X(0) = \varepsilon(0) = 0$. (a) Back stress evolution (b) Trajectory of state vector

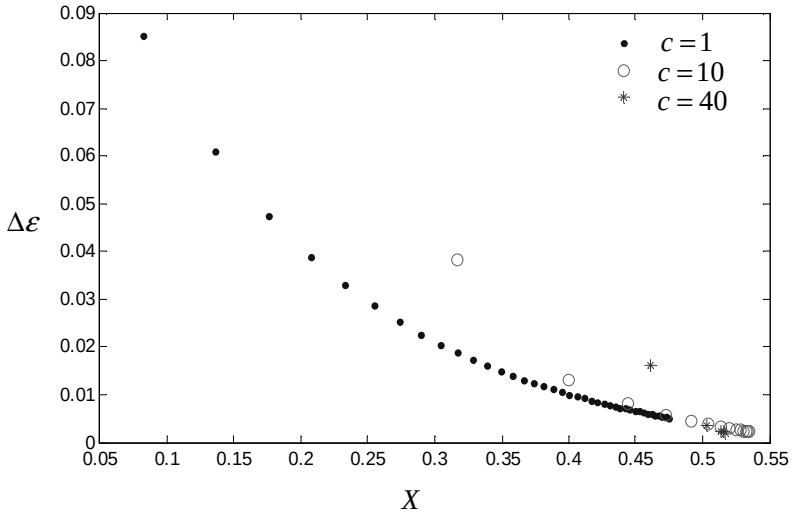

Figure 2.5 Effect of c on state vector convergence rate

It is important to note that c does not only affect the converging rate, but also the periodic solution of the system. As shown in Figure 2.5, the equilibrium value of the state vector changes with c.

Note that the system starts in case I, then it will stay in case I. However, this is not the case for case II and case III since it is possible for the solution to switch from one to the other (e.g. see situation (3) in section 2.2.4) in different cycles. Therefore, the analysis above does not cover all possible scenarios (e.g. only sufficient condition is established for the existence of periodic long time solution). The difficulty lies in the fact that the initial value of the back stress in each cycle depends on the previous cycle. Furthermore, the solution of the differential equations cannot be written in close form. In the following, we use a dynamic system approach to defeat these difficulties.

2.2.4 Phase Portrait Analysis

To complete the analysis, we study the back stress evolution during valley stress hold $\left(S(\tau)=S_{\min}\right)$ by examining the phase portrait of (2.21), i.e.,

$$dX/d\tau = c\left(\operatorname{sgn}(S_{\min}-\frac{3}{2}X)-X\right)\left\langle\left|S_{\min}-\frac{3}{2}X\right|-K\right\rangle^{n}. \tag{2.40}$$

The fixed points of (2.40), denoted by X^*, satisfy

$$\operatorname{sgn}(S_{\min}-\frac{3}{2}X^*)-X^*=0 \tag{2.41}$$

$$\left\langle\left|S_{\min}-\frac{3}{2}X^*\right|-K\right\rangle=0 \tag{2.42}$$

Equations (2.41),(2.42) show that the fixed points depend on the *sign* of $S_{\min}-3X^*/2$. Consider first where $\operatorname{sgn}(S_{\min}-3X^*/2)=1$. For this case, (2.41),(2.42) imply that the fixed points are

$$X_1^*=1,\ X^*\geq X_2^*\equiv\frac{2}{3}(S_{\min}-K) \tag{2.43}$$

Note that there is an *infinite number of fixed points* since any point satisfies $X^* \geq X_2^*$ is a fixed point of (2.42). For the case where $\text{sgn}(S_{\min} - 3X^*/2) = -1$, the fixed points are

$$X_3^* = -1,\ X^* \leq X_4^* = \frac{2}{3}(S_{\min} + K) \tag{2.44}$$

Similarly, (2.44) predicts that there exists an *interval* of fixed points $X^* \leq X_4^*$. Comparing (2.43) and (2.44), we found $X_2^* < X_4^*$ since $K > 0$.

Note that $\text{sgn}(S_{\min} - 3X^*/2) = 1$ implies $dX/d\tau \geq 0$ since $\left\langle \left| S_{\min} - 3X^*/2 \right| - K \right\rangle$ is non-negative and $c > 0$. Therefore, the only way to reach the fixed points X_1^*, X_2^* is from $dX/d\tau > 0$ (flow is in positive direction). Similarly, $\text{sgn}(S_{\min} - 3X^*/2) = -1$ implies that $dX/d\tau \leq 0$ so the fixed points X_3^*, X_4^* can only be reached from $dX/d\tau < 0$ (flow is in negative direction). Since the existence and arrangement of fixed points are determined by the sign of $S_{\min} - 3X^*/2$, the phase portrait of (2.40) is different for different $S_{\min}$ and K. To illustrate this dependence, phase portraits for a *fixed* $K = 0.4$ and for different values of $S_{\min}$ are shown in Figure 2.6(a-e)($c = 1, n = 5$). Darks lines indicate intervals of fixed points where back stress do not evolve. Arrows indicate flow direction, i.e., how X changes with time. Note that $-1 = X_3^* < X_1^* = 1, X_2^* < X_4^*$. Without loss in generality, we assume the initial back stress X_{ini} in valley hold cycle lies in $0 \leq X_{ini} \leq 1$.

In Figure 2.6(a), we choose $S_{\min}$ sufficiently large so that $X_2^* > X_1^* = 1$. This means that the interval of fixed points $X^* \geq X_2^*$ lie outside of [0,1]. Since X cannot exceed its saturation value 1, these fixed points can never be reached and hence is not shown in Figure 2.6(a). Note that $dX/d\tau > 0$ for all $0 < X_{\text{ini}} < 1$, so X will increase until it reaches $X_1^* = 1$. If we gradually reduce $S_{\min}$, then X_2^* will decrease until $X_2^* < X_1^* = 1$ ($X_2^* = 1$ when $S_{\min} = K + 3/2$); that is, the interval $X_2^* \leq X^* \leq X_1^*$ becomes part of $[-1,1]$ (dark line in Figure 2.6(b)). If X_{ini} lies in $\left[X_2^*, X_1^* \right]$, then $dX/d\tau = 0$ since any point inside $\left[X_2^*, X_1^* \right]$ is a fixed point, so the back stress remains unchanged, i.e.,

$X = X_{ini}$. If $0 \le X_{ini} < X_2^*$, then $dX/d\tau > 0$ by (2.40) so the back stress will increase until it reaches X_2^* (see Figure 2.6(b)), then remains there. Both $dX/d\tau > 0$ and $dX/d\tau < 0$ will occur as we decrease $S_{\min}$ below $K + 3/2$ as shown in Figure 2.6(c). For this case, $\text{sgn}(S_{\min} - 3X_2^*/2) = 1$ and $\text{sgn}(S_{\min} - 3X_4^*/2) = -1$ and the four fixed points appear in the order of $X_3^* < 0 < X_2^* < X_4^* < X_1^*$. According to (2.43),(2.44), every point in $\left[X_2^*, X_4^*\right]$ is a fixed point, so if $X_{\text{ini}} \in \left[X_2^*, X_4^*\right]$, the back stress do not evolve and $X = X_{\text{ini}}$. If $X_{\text{ini}} \in \left(0, X_2^*\right)$ where $dX/d\tau > 0$, the back stress will increase until it reaches X_2^*. If $X_{\text{ini}} \in \left(X_4^*, X_1^* = 1\right]$, then $dX/d\tau < 0$ and the back stress will decrease until it reaches X_4^* (see Figure 2.6(c)). As $S_{\min}$ decreases further so that $S_{\min} < K$ which implies that $X_2^* < 0$, the interval of fixed points becomes $\left(0, X_4^*\right]$, $-1 < X_4^* < 1$, (see Figure 2.6(d)). For this case, if $X_{\text{ini}} \in \left[X_4^*, 1\right]$, the back stress will decrease until it reaches X_4^*, then stays there. Figure 2.6(d) shows the case where $1 > X_4^* > 0$. Note that the phase diagram has identical feature if $-1 < X_4^* < 0$. Finally, if $S_{\min}$ is reduced further so that $X_4^* < X_3^* < 0$ (see Figure 2.6(e)). Equation (2.40) implies that $dX/d\tau < 0$ for all $0 < X_{\text{ini}} < 1$. Since $X_4^* < X_3^* < -1$, the only accessible fixed point is $X_3^* = -1$, so the back stress will decrease until it reaches X_3^*.

Having established the back stress behavior during valley stress hold, we are in position to address the existence of periodic solution. Recall that the back stress *always increases during peak stress hold*, so the existence of periodic or oscillatory solution will require the back stress to decrease during valley stress hold. There are three situations:

(1): For the situation shown in Figure 2.6(a,b), a periodic solution does not exist since back stress also increases during valley stress hold.

(2): For the situation shown in Figure 2.6(e), the back stress will always decrease during valley stress hold given any X_{ini}, so a periodic solution exists.

(3): For the situation shown in Figure 2.6(c,d), if $0 < X_{\text{ini}} \le X_4^*$, the back stress will

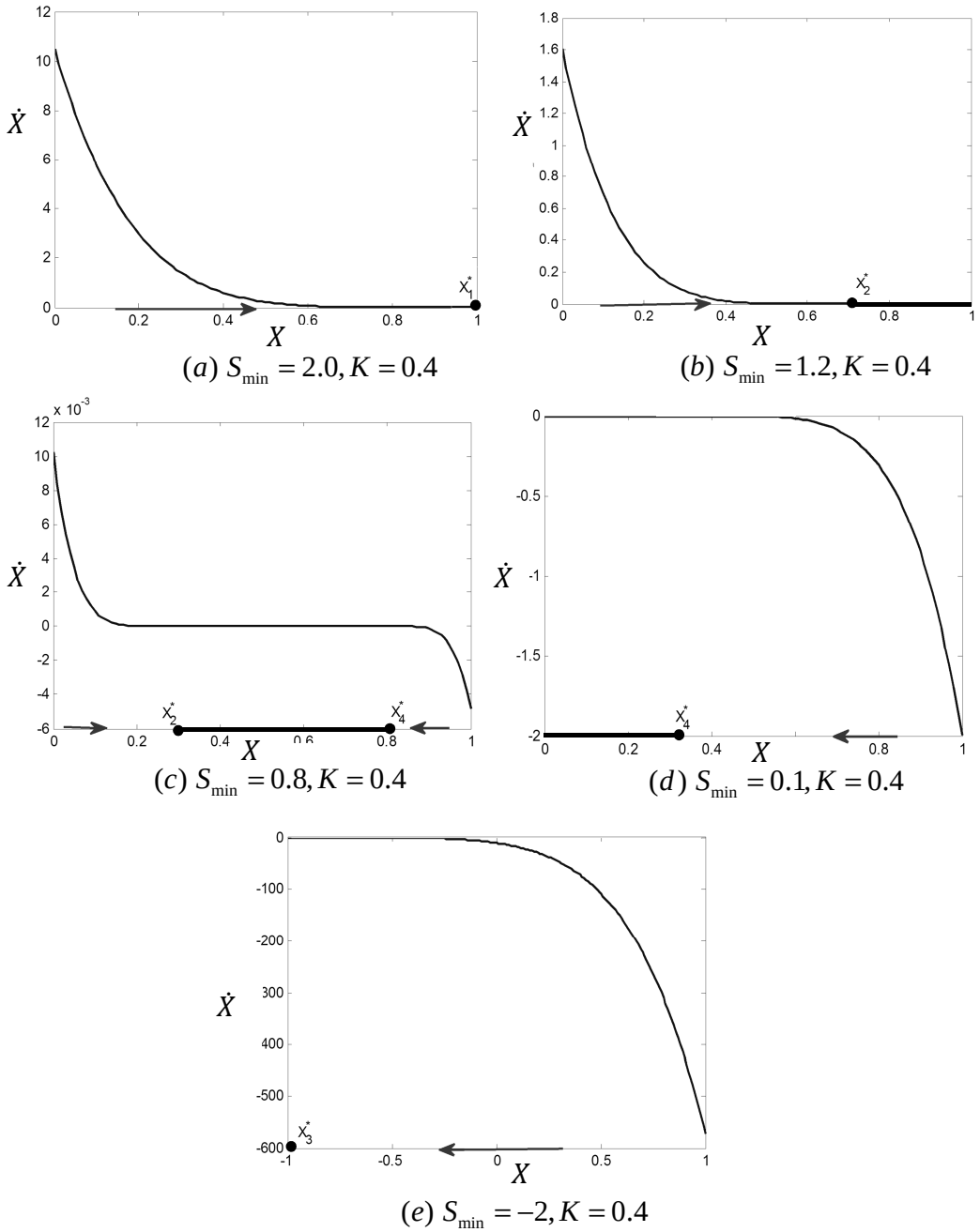

$(a)\ S_{\min} = 2.0, K = 0.4$ $(b)\ S_{\min} = 1.2, K = 0.4$

$(c)\ S_{\min} = 0.8, K = 0.4$ $(d)\ S_{\min} = 0.1, K = 0.4$

$(e)\ S_{\min} = -2, K = 0.4$

Figure 2.6 Phase portrait of back stress evolution during valley stress hold

either stay as a constant (if $X_2^* \le X_{\text{ini}} \le X_4^*$) or increase (if $0 \le X_{\text{ini}} < X_2^*$) during valley stress hold. However, after a finite number of cycles, *the back stress will increase beyond* X_4^* *(since back stress increases during peak stress hold*), then it will start to decrease towards X_4^* during valley stress hold. This process will continue indefinitely. Hence, periodic solution will be reached at sufficiently long times.

The analysis above shows that the phase portrait and the existence of periodic solution depend on the order of the fixed points X_1^*, X_2^*, X_3^* and X_4^*. Recall Figure 2.6(a-e) are generated by fixing $K = 0.4$ and varying $S_{\min}$. The general case where $S_{\min}$ and $K > 0$ vary independently can also be analyzed based on the same idea. These results are summarized in a two parameter map which divides the ($S_{\min}, K$) plane into six regions (①-⑥) based on the order of the four fixed points (Figure 2.7). Recall that by definition (2.43) and (2.44), $X_3^* < X_1^*, X_2^* < X_4^*$. The boundary lines separating the different regions in Figure 2.7 are:

(1): $S_{\min} = \frac{3}{2} + K$, $X_1^* = X_2^*$; (2): $S_{\min} = K$, $X_2^* = 0$;

(3): $S_{\min} = \frac{3}{2} - K$, $X_1^* = X_4^*$;(4): $S_{\min} = -\frac{3}{2} - K$, $X_3^* = X_4^*$;

At a given temperature, *K* is a constant as indicated by the vertical line AB in Figure 2.7. This line goes through five regions ①, ②, ④, ⑤,⑥. The corresponding phase portraits for each region are shown in Figure 2.7(a-e) (for example, region 1 corresponds to Figure 2.7(a) etc.). To make contact with the phase portraits in Figure 2.7(a-e), the arrow on AB indicates the direction of decreasing *S*. If a different *K* is used, then the corresponding line CD will go through regions ①, ②,③, ⑤,⑥ (see Figure 2.7). The resulting phase portraits are similar except region ④ is replaced by region ③. In region ③, $X_2^* < 0$, and $(0,1]$ is an interval of fixed points, that is, if $X_{\text{ini}} \in (0,1]$, the back stress does not change.

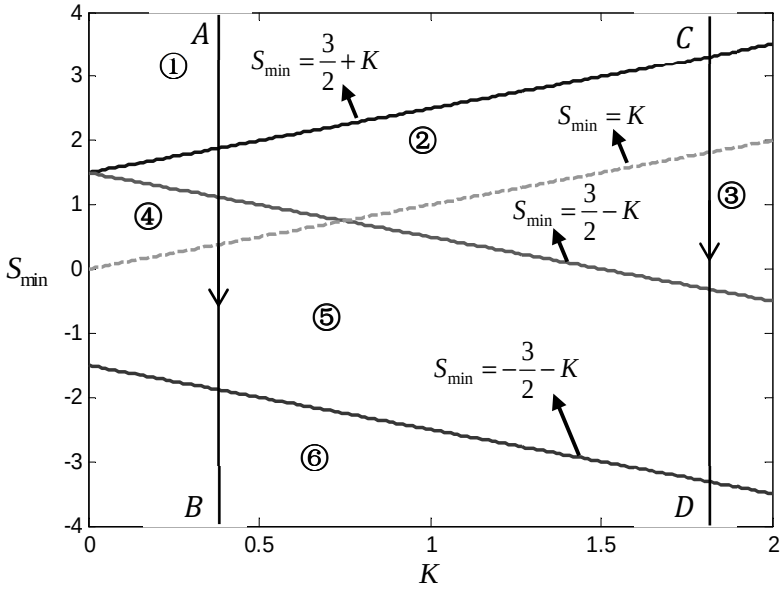

Figure 2.7 Parameter map divided into six regions

In summary, if ($S_{\min}, K$) lies in a region above the boundary line $S_{\min} = 3/2 - K$, (in regions ①, ② and ③), periodic solutions do not exist. On the other hand, existence of periodic solution is guaranteed if ($S_{\min}, K$) lies below the line, (in regions ④, ⑤ and ⑥). *Thus, a necessary and sufficient condition for periodic solution is*

$$S_{\min} < 3/2 - K \tag{2.45}$$

Equation (2.45) states that the back stress is oscillatory for sufficiently small valley stress or yield stress.

2.3 Long Term Memory

A very interesting and important feature of the present UVM is that the inelastic strain evolution can be completely different if there is a phase shift of the loading waveform (see Figure 2.8). In other words, it matters in the long term whether we start loading the specimen in tension or in compression. That is, the dynamical system has long term memory. To illustrate this feature, consider the special case where $S_{\max} = S, S_{\min} = -S$ with hold times τ_1 (peak hold) and $\tau_2 = \tau_c - \tau_1$ (valley hold) respectively. As before, we assume $S > 3/2 + K$ so that $\dot{p} > 0$ during peak/valley stress hold. Note for this case, the long time behavior of the back stress is a periodic since $S_{\min} = -S = -3/2 - K$ which satisfies (2.45). Consider the following two loading histories in Figure 2.8:

(1) Tension-compression loading (Figure 2.8(a)): the loading cycle starts with tension holding during $0 \le \tau < \tau_1$ and is followed by compression holding during $\tau_1 \le \tau < \tau_c$.

(2) Compression-tension loading (Figure 2.8(b)), i.e, the loading cycle starts with compression holding during $0 \le \tau < \tau_2$ and is followed by tension holding for $\tau_2 \le \tau < \tau_c$. i.e, the loading waveform is obtained by shifting the waveform in Figure 2.8(a) to the left by τ_1.

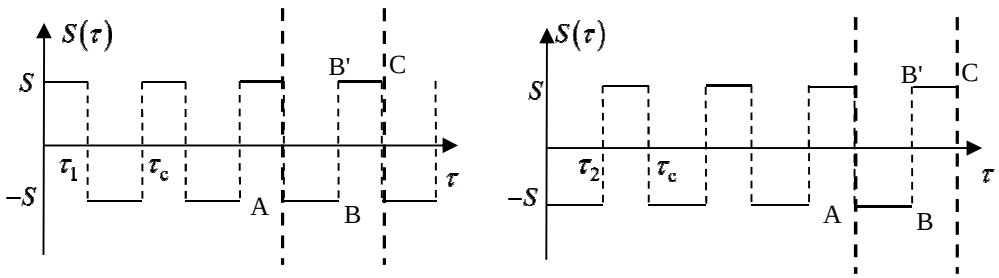

(a) (b)

Figure 2.8 Loading history (a) tension-compression loading. (b) Compression-tension loading

Denote $X_{\text{t-c}}(\tau), \varepsilon_{\text{t-c}}(\tau)$ as the back stress and accumulated inelastic strain at τ for tension-compression loading. Likewise, let $X_{\text{c-t}}(\tau), \varepsilon_{\text{c-t}}(\tau)$ denote the back stress and accumulated inelastic strain at τ for compression-tension loading. Intuitively, one would expect that phase shifts should have no effect on the long time inelastic strain accumulation. In other words, after a sufficiently large number of cycles, $\varepsilon_{\text{t-c}}(\tau)$ and $\varepsilon_{\text{c-t}}(\tau)$ in the time interval A-B-B'-C in Figure 2.8(a,b) should satisfy the condition

$$\varepsilon_{\text{t-c}}(\tau) = \varepsilon_{\text{c-t}}(\tau + \tau_1) \tag{2.46}$$

However, the counter-example below showed otherwise.

During tension hold, $S(\tau) = S_{\max} = S$, the back stress and inelastic strain evolves according to

$$dX / d\tau = c(1 - X)\left(S - \frac{3}{2}X - K\right)^n \tag{2.47}$$

$$d\varepsilon / d\tau = \left(S - \frac{3}{2}X - K\right)^n \tag{2.48}$$

During compression hold, $S(\tau) = S_{\min} = -S$, the back stress and inelastic strain evolves according to

$$dX / d\tau = c(-1 - X)\left(S + \frac{3}{2}X - K\right)^n \tag{2.49}$$

$$d\varepsilon / d\tau = -\left(S + \frac{3}{2}X - K\right)^n \tag{2.50}$$

Let $Y = -X, \delta = -\varepsilon$, (2.49), (2.50) can be rewritten as

$$dY / d\tau = c(1 - Y)\left(S - \frac{3}{2}Y - K\right)^n \tag{2.51}$$

$$d\delta / d\tau = \left(S - \frac{3}{2}Y - K\right)^n \tag{2.52}$$

Hence, if $\left(X(\tau), \varepsilon(\tau)\right)$ is the solution for (2.47), (2.48) for the initial conditions $\left(X(\tau = 0) = X_0, \varepsilon(\tau = 0) = \varepsilon_0\right)$, then $\left(-X(\tau), -\varepsilon(\tau)\right)$ is the solution for (2.49), (2.50) for initial condition $\left(X(\tau = 0) = -X_0, \varepsilon(\tau = 0) = -\varepsilon_0\right)$. Therefore, for the special case

where $\tau_1 = \tau_2 = \tau_c / 2$, at the end of first hold period, the back stress and accumulated inelastic strain for Figure 2.8(a), (b) satisfy $X_{\text{t-c}}(\tau_1) = -X_{\text{c-t}}(\tau_2), \varepsilon_{\text{t-c}}(\tau_1) = -\varepsilon_{\text{c-t}}(\tau_2)$ given the same initial condition $X(0) = \varepsilon(0) = 0$. Continuing this line of reasoning, it is easy to see that $X_{\text{t-c}}(\tau) = -X_{\text{c-t}}(\tau), \varepsilon_{\text{t-c}}(\tau) = -\varepsilon_{\text{c-t}}(\tau)$ for all times. This clearly violates (2.46). This counter example shows that that the long time inelastic strain for compression-tension loading cannot be obtained from tension-compression case by a simple phase shift, i.e., $\varepsilon_{\text{t-c}}(\tau) \neq \varepsilon_{\text{c-t}}(\tau + \tau_1)$. In other words, how one starts the system has long term consequences.

Our above argument works only when $\tau_1 = \tau_2$. Consider the case $\tau_1 \neq \tau_2$, the results in Figure 2.9 are carried out using $S_{\max} = -S_{\min}, K = 0.1, n = 5, \tau_2 = 2\tau_1 = 0.02$, which shows that when the system reaches steady state, i.e., $X_{\text{t-c}}(\tau) = X_{\text{c-t}}(\tau + \tau_1)$ but $\varepsilon_{\text{t-c}}(\tau) \neq \varepsilon_{\text{c-t}}(\tau + \tau_1)$. Hence, the accumulated inelastic strain depends on the initial condition and the system has long term memory.

2.4 Ratcheting in Cyclic Loading

Ratcheting, the inelastic strain accumulated cycle by cycle, is an important quantity in the life estimation of high temperature materials subjected to cyclic loading. Ratcheting has been studied extensively over the past decades for many different materials including stainless steel (Yoshida 1990; Kang et al. 2002; Yaguchi and Takahashi 2005a), solder alloys (Chen et al. 2006), polymers (Chen and Hui 2005) and composites (Zhang et al. 1990; Jansson and Leckif 1992) at both room and elevated temperatures. Reviews of these works can be found in the papers by Ohno (1990b, 1997) and Kang (2008). In many papers, the uniaxial ratcheting strain ε_r is defined as (Kang et al. 2002; Kang et al. 2006; Park et al. 2007)

$$\varepsilon_r = \frac{1}{2}\left(\varepsilon_{\max} + \varepsilon_{\min}\right) \tag{2.53}$$

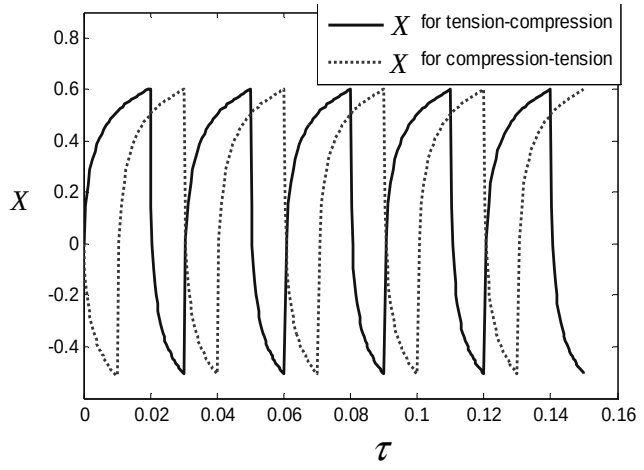

(a)

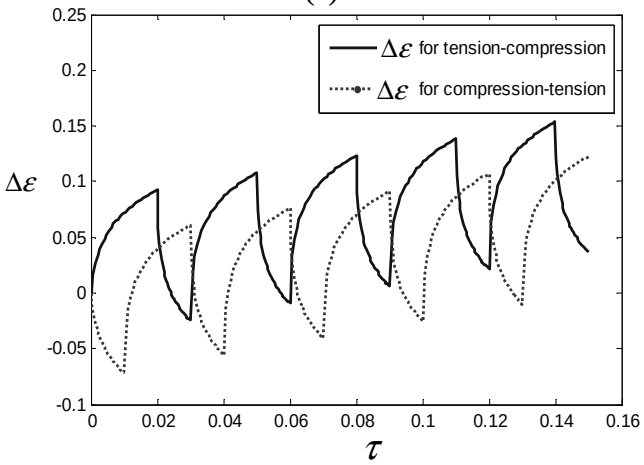

(b)

Figure 2.9 Back stress and inelastic strain history for cyclic loading (a) back stress versus time (b) inelastic strain versus time

where $\varepsilon_{\max}$ and $\varepsilon_{\min}$ are the maximum and minimum strains within one loading cycle. Another definition of ratchetting strain (Kang 2008) is

$$\varepsilon_{\mathrm{r}} = \varepsilon_{n+1}^{\max} - \varepsilon_{n}^{\max} \tag{2.54}$$

where $\varepsilon_{n+1}^{\max}$ and $\varepsilon_{n}^{\max}$ are the maximum strain in the *n*th and *n+1*th cycle. As pointed out in the literature (Zhang et al. 1990; Ohno 1990b; Kang 2008; Yoshida 1990; Yaguchi and Takahashi 2005b, 2005a; Chaboche and Nouailhas 1989a-a),

(1) Accurate modeling of ratchetting depends on the kinematic hardening rule in the constitutive model.

(2) The amount of ratcheting strain depends on a variety of factors such as mean stress, peak/valley stress hold time, loading rate and temperature.

According to various investigators (Breitbach et al. 1989; Breitbach et al. 1994), there are two contributions to the inelastic strains during cyclic loading: a time-dependent component induced by creep and a time-independent progressive cyclic strain component induced by back stress evolution. The difficulty is that these two contributions are coupled in the UVM approach and hence no simple decomposition of strains is possible. Here we propose a dimensionless ratio, called ratchetting ratio, which is defined by

$$R_{\text{ratchetting}} = \left| \frac{\Delta\varepsilon_{\infty}}{\Delta\varepsilon_{ss}} \right| \tag{2.55}$$

where $\Delta\varepsilon_{\infty}$ is the long term inelastic strain increment per cycle defined in section 2.2.3 in a cyclic test, and it is the same as ε_r defined in (2.54); $\Delta\varepsilon_{\mathrm{ss}}$ is defined by

$$\Delta\varepsilon_{\mathrm{ss}} \equiv \left(S_{\max} - 3/2 - K\right)^{n} \tau_{\mathrm{c}} \tag{2.56}$$

which is the inelastic strain accumulated in time τ_{c} in a creep test with *constant* stress $S_{\max}$. Intuitively, one may think that because the mean stress in a tension-compression cyclic test is always lower than $S_{\max}$, $\Delta\varepsilon_{\mathrm{ss}} > \Delta\varepsilon_{\infty}$. However, this argument is flawed

since the normalized back stress can be significantly lower than $3/2+K$ during peak hold in a cyclic test.

A necessary condition for $R_{\text{ratchetting}}<1$ can be obtained based on our result in section 2.2.4. Equation (2.26) guarantees that the back stress is monotonically increasing if $S_{\min}>3/2-K$. If this is the case, then the long time inelastic strain accumulated per cycle is given by (2.31). A comparison of (2.31) and (2.56) shows that

$$R_{\text{ratcheting}}=\Delta\varepsilon_{\infty}/\Delta\varepsilon_{\text{ss}}=\tau_1/\tau_{\text{c}}<1 \tag{2.57}$$

in the absence of back stress oscillation. In other words, back stress oscillations is a necessary condition for $R_{\text{ratchetting}}>1$. According to (2.45), a necessary solution for $R_{\text{ratchetting}}>1$ is $S_{\min}<3/2-K$. Unfortunately, we have not been able to find the sufficient condition for $R_{\text{ratchetting}}>1$ in terms of a closed form expression involving material constants and loading parameters. Our numerical results show that the ratcheting ratio depends on the material and loading parameters. Some examples are given in Figure 2.10(a-d) which use the same set of parameter $S_{\max}=2.1, K=0.1,$ $c=10, \tau_1=\tau_2=2$ with varying *n*. As shown in the figures, in general small $\left|S_{\min}/S_{\max}\right|$ tends to have higher $R_{\text{ratcheting}}$, however, the condition $R_{\text{ratcheting}}>1$ does not always occur.

2.5 Summary and Discussion

There are obvious limitations in our analysis. The UVM model used in this work is based on the nonlinear kinematic hardening (NLK) rule proposed by Armstrong and Frederick (1966). It is well known that this rule tends to overestimate the ratcheting strain in uniaxial and multi-axial cyclic tests (Chaboche and Nouailhas 1989b-a; Inoue et al. 1989; Freed and Walker 1990). We assume a very rapid loading and unloading

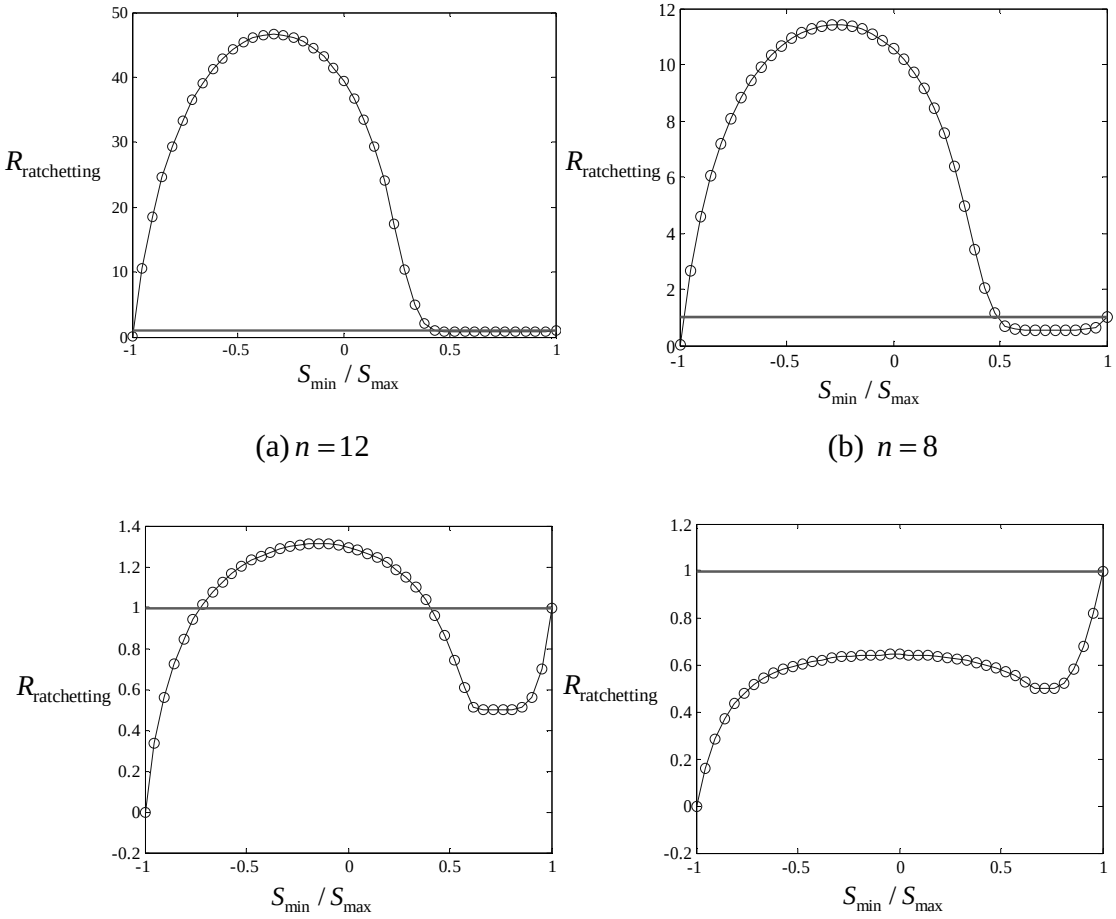

Figure 2.10 Ratcheting ratio versus $S_{\min} / S_{\max}$ for different n.

Rate so that the effect of loading rate is not explored. However, our goal is not to include the most comprehensive model of UVM, but to illustrate a different approach which may offer more insight into the behavior of UVM. We believe many of the features highlighted in this chapter are applicable to many of the UVM in the literature. In addition, our approach can be extended to study other UVM models.

In our analysis, we have neglected the evolution of two state variables. Specifically, we neglected the evolution of one of the state variables that governs the evolution of the back stress (β in Equation(2.10)) and the one that governs hardening (r in Equation(2.7)).

These simplifications have little effect on the long time qualitative behavior of the solution. For example, for sufficiently long times, $r \to r_\infty$ and it can be absorbed into the yield stress K. In addition, we can always pick $c_2 > c_1$ so that the state variable β evolves much faster than α.

To summarize, we found,

1: As long as $S_{\max} > 3/2 + K$ and $S_{\min} < 3/2 - K$, the back stress will be oscillatory and there exists a periodic solution. Otherwise, the back stress will increase monotonically to its saturation value.

2: The long time inelastic strain depends on the initial condition, i.e., a phase shift of the loading waveform can lead to completely different inelastic strain accumulation. This result presents an interesting idea that may be important in practice, that is, it is possible to pre-treat the material to ensure less ratchetting .

3: The ratchetting ratio during high temperature cyclic loading depends on the overall effect of loading and material parameter. This ratio is smaller than 1 if the back stress is not oscillatory, that is, if $S_{\min} > 3/2 - K$. In other words, low yield stress and large valley stress reduces ratcheting.

REFERENCES

Adefris N, Saxena A, McDowell D (1996) Creep fatigue crack growth behavior in 1Cr-1Mo-0.25V steels. Part I: Estimation of crack tip parameters. Fatigue Fract Eng Mater Struct 19:387-398

Armstrong PJ, Frederick CO, Britain G (1966) A mathematical representation of the multiaxial Bauschinger effect. Central Electricity Generating Board and Berkeley Nuclear Laboratories, Research & Development Dept.,

Bodner S, Partom Y (1975) Constitutive equations for elastic-viscoplastic strain-hardening materials. J Appl Mech 42:385

Breitbach G, Over H, Schubert F (1989) Experimentally verified creep ratcheting analysis. Nucl Eng Des 116:231-238

Breitbach G, Schmidt-Plutka A, Schubert F, Nickel H (1994) Investigations of creep ratcheting on thick-walled tubes. Nucl Eng Des 151:337-345

Chaboche J, Nouailhas D (1989a) Constitutive Modeling of Ratchetting Effects-Part I: Experimental Facts and Properties of the Classical Models. J Eng Mater Technol 111:384

Chaboche J, Nouailhas D (1989b) Constitutive Modeling of Ratchetting Effects-Part II: Possibilities of Some Additional Kinematic Rules. J Eng Mater Technol 111:409

Chaboche JL (1989) Constitutive equations for cyclic plasticity and cyclic viscoplasticity. Int J Plast 5:247-302

Chaboche JL, Rousselier G (1983) On the plastic and viscoplastic constitutive equations-Part I: Rules developed with internal variable concept. J Pressure Vessel Technol 105:153

Chen G, Chen X, Niu CD (2006) Uniaxial ratcheting behavior of 63Sn37Pb solder with loading histories and stress rates. Mater Sci Eng, A 421:238-244

Chen X, Hui S (2005) Ratcheting behavior of PTFE under cyclic compression. Polym Test 24:829-833

Chomette S, Gentzbittel JM, Viguier B (2010) Creep behaviour of as received, aged and cold worked Inconel 617 at 850° C and 950° C. J Nucl Mater 399:266-274

Cook R (1984) Creep properties of Inconel-617 in air and helium at 800 to 1000° C. Nucl Technol 66:283-288

Drubay B, Marie S, Chapuliot S, Lacire M, Michel B, Deschanels H (2003) A16: guide for defect assessment at elevated temperature. Int J Press Vessels Pip 80:499-516

Freed AD, Walker KP (1990) Model development in viscoplastic ratchetting. National Aeronautics and Space Administration, Cleveland, OH (USA). Lewis Research Center,

Grover P, Saxena A (1999) Modelling the effect of creep-fatigue interaction on crack growth. Fatigue Fract Eng Mater Struct 22:111-122

Guerin Y, Was GS, Zinkle SJ (2009) Materials Challenges for Advanced Nuclear Energy Systems. MRS Bull:10-14

Inoue T, Ohno N, Suzuki A, Igari T (1989) Evaluation of inelastic constitutive models under plasticity-creep interaction for 21/4Cr-1Mo steel at 600 C. Nucl Eng Des 114:259–309

Jansson S, Leckif F (1992) Mechanical behavior of a continuous fiber-reinforced aluminum matrix composite subjected to transverse and thermal loading. J Mech Phys Solids 40:593-612

Kang G (2008) Ratchetting: Recent progresses in phenomenon observation, constitutive modeling and application. Int J Fatigue 30:1448-1472

Kang G, Gao Q, Cai L, Sun Y (2002) Experimental study on uniaxial and nonproportionally multiaxial ratcheting of SS304 stainless steel at room and high temperatures. Nucl Eng Des 216:13-26

Kang G, Kan Q, Zhang J, Sun Y (2006) Time-dependent ratchetting experiments of SS304 stainless steel. Int J Plast 22:858-894

Krempl E (1987) Models of viscoplasticity some comments on equilibrium (back) stress and drag stress. Acta Mech 69:25-42

Kurata Y, Nakajima H (1995) Temperature dependence of creep properties of cold-worked Hastelloy XR. J Nucl Sci Technol 32:539-546

Lee HY, Song KN, Kim YW (2010) Evaluation of Creep-Fatigue Damage for Hot Gas Duct Structure of the NHDD Plant. J Pressure Vessel Technol 132:031101

Miller A (1976) An inelastic constitutive model for monotonic, cyclic, and creep deformation: Part I-Equations development and analytical procedures. J Eng Mater Technol 98:97

Mo K, Lovicu G, Tung HM, Chen X, Stubbins JF (2011) High Temperature Aging and Corrosion Study on Alloy 617 and Alloy 230. J Eng Gas Turbines Power 133:052908

Natesan K, Purohit A, Tam S (2003) Materials Behavior in HTGR Environments. Office of Nuclear Regulatory Research, Washington.

Ohno N (1990) Recent topics in constitutive modeling of cyclic plasticity and viscoplasticity. Appl Mech Rev 43:283–295

Ohno N (1997) Recent progress in constitutive modeling for ratchetting. Mater Sci Res Int 3:1-9

Park S, Kim K, Kim H (2007) Ratcheting behaviour and mean stress considerations in uniaxial low cycle fatigue of Inconel 718 at 649° C. Fatigue Fract Eng Mater Struct 30:1076-1083

Ren W, Swimdeman R (2009) A Review Paper on Aging Effects in Alloy 617 for Gen IV Nuclear Reactor Applications. J Pressure Vessel Technol 131:024002

Schneider K, Hartnagel W, Iischner B, Schepp P (1984) Creep behavior of materials for high-temperature reactor application. Nucl Technol 66:289-295

Schubert F, te Heesen E, Bruch U, Cook R, Diehl H, Ennis P, Jakobeit W, Penkalla H, Ullrich G (1984) Creep rupture behavior of candidate materials for nuclear process heat applications. Nucl Technol 66:227-240

Shah VN, Majumdar S, Natesan K, Technology UNRCOoNRRDoE (2003) Review and assessment of codes and procedures for HTGR components. Division of Engineering Technology, Office of Nuclear Regulatory Research, US Nuclear Regulatory Commission,Argonne National Laboratory,

Wakai T, Poussard C, Drubay B (2002) A comparison between Japanese and French A16 defect assessment procedures for fatigue crack growth. Nucl Eng Des 212:125-132

Walker KP (1981) Research and development program for non-linear structural modeling with advanced time-temperature dependent constitutive relationships.

Yaguchi M, Takahashi Y (2005a) Ratchetting of viscoplastic material with cyclic softening, part 1: experiments on modified 9Cr-1Mo steel. Int J Plast 21:43-65

Yaguchi M, Takahashi Y (2005b) Ratchetting of viscoplastic material with cyclic softening, part 2: application of constitutive models. Int J Plast 21:835-860

Yoon KB, Saxena A, McDowell DL (1992) Influence of crack-tip cyclic plasticity on creep-fatigue crack growth. In: Ernst HA, Saxena A, McDowell DL (eds) Fracture Mechanics: Twenty-Second Symposium, Philadelphia, 1992. American Society for Testing and Materials, pp 367-392

Yoshida F (1990) Uniaxial and biaxial creep-ratcheting behavior of SUS304 stainless steel at room temperature. Int J Press Vessels Pip 44:207-223

Zhan ZL, Tong J (2007a) A study of cyclic plasticity and viscoplasticity in a new nickel-based superalloy using unified constitutive equations. Part I: Evaluation and determination of material parameters. Mech Mater 39:64-72

Zhan ZL, Tong J (2007b) A study of cyclic plasticity and viscoplasticity in a new nickel-based superalloy using unified constitutive equations. Part II: Simulation of cyclic stress relaxation. Mech Mater 39:73-80

Zhang H, Daehn GS, Wagoner R (1990) The Temperature-Cycling Deformation of Particle Reinforced Metal Matrix Composites-A Finite Element Study. Scr Metall Mater 24:2151-2155

Zhao L, Tong J (2008) A viscoplastic study of crack-tip deformation and crack growth in a nickel-based superalloy at elevated temperature. J Mech Phys Solids 56:3363-3378

CHAPTER 3

CRACK TIP FILEDS IN A VISCOPLASTIC SOLID-MONOTONIC AND CYCLIC LOADING

3.1 Introduction

Recent interest in nuclear power has renewed interest in the study of high temperature materials fracture, in particular, nickel based alloys because of their exceptional high temperature creep strength. In the power plant industry, operating temperature in the equipment components is usually high. For some highly stressed components which are part of reactors, cracks from unavoidable sharp corners during fabrication or workmanship flaws may develop at certain locations and propagate due to fatigue and creep. So the reliability of these components at high temperatures becomes a significant concern. Creep fatigue and crack growth could lead to failure of the power plant equipment such as intermediate heat exchangers. Thus, to predict the design and remaining life of power plant components accurately, modeling these cracks with a constitutive model that describes the crack creeping behavior is a natural choice.

The standard fracture mechanics approach is to relate crack tip processes to a loading parameter that quantifies the strength of the crack tip stress fields. This parameter allows engineers to correlate crack growth rate in complex structures with the applied load. Attempts at understanding the time dependent crack tip stress fields can be traced back to Riedel and Rice with their seminal analysis on the stress field near the tip of a stationary Mode I crack in an elastic-power law creeping material (Riedel and Rice 1980). Since their work, a considerable amount of literature on crack tip loading parameters for creep crack growth has appeared (Riedel 1981; Bassani and

McClintock 1981; Atluri 1982; Schapery 1986; Saxena 1986; Bassani et al. 1989; Hall et al. 1998; Wang et al. 2000).

Most of the crack tip analyses are based on an elastic power law creeping (EPLC) solid. The primary reason for choosing the EPLC model is that the stress field near a crack tip is characterized by the crack tip loading parameters such as K_I , C^* or C_t in this model. However, even in monotonic loading, nickel based alloys typically exhibit complex deformation behavior (Chomette et al. 2010; Schubert et al. 1984; Cook 1984; Schneider et al. 1984; Kurata and Nakajima 1995). Another shortcoming of the EPLC model is that it does not describe material behavior under cyclic deformation well. Therefore, the use of crack tip parameters such as C* or $C(t)$ to characterize crack growth in these alloys can be questionable. Compared to monotonic loading, crack tip field under cyclic loading presents a more challenging problem and has received much less attention. Riedel (1983) studied crack tip fields in EPLC materials under cyclic loading conditions. Yoon et al. (1992) carried out both experimental and numerical studies on creep-fatigue crack growth (CFCG) behavior of 1.25Cr-0.5Mo steel. Adefris et al. (1996a, b) studied the combined effect of cyclic plasticity and creep deformation on creep fatigue crack growth of a 1Cr-1Mo-1/4V steel. Grover and Saxena (1999) proposed a new creep-reversal parameter to quantify creep-fatigue interaction. In these papers, a constitutive model in which the inelastic strain is the sum of a rate independent plastic strain and creep strain was used.

A growing body of research demonstrates that much of the complex deformation behavior of high temperature metal alloys during cyclic loading, such as stress relaxation, ratcheting and cyclic softening/hardening behavior, can be captured by so called unified viscoplastic models (UVM) ((Chaboche 1989), also see review papers by Ohno (1990a), Chaboche (Chaboche 2008) and the references within). One of the advantages of these UVM is that there is no separation between creep and rate

independent plasticity. Despite the success of UVM to represent high temperature material behavior, very few researchers have studied the deformation and stress field near the crack tip using these models. Zhao and Tong (2008) studied the behavior of the cyclic stress and deformation field in a cracked specimen numerically using a UVM of Chaboche (1989). Their study was purely numerical, for example, they did not investigate the existence of crack tip parameters for viscoplastic materials. Stamm and Walz (Stamm and Walz 1993; Walz and Stamm 1993) carried out both numerical and analytical investigation of crack tip fields in viscoplastic materials. Their numerical work focused on the regime of high applied stresses.

The brief summary above suggests that it may be useful to study the crack tip field of a viscoplastic material and compare these fields with those of an elastic power-law creeping material. In this chapter, we carried out analytical and numerical studies on the Mode I crack tip stress fields of a viscoplastic material. This model was originally conceived by Chaboche (1989) and later used by Zhao and Tong (2008) to study creep fracture in Alloy RR1000. In the first part of this chapter, we derive the asymptotic crack tip fields associated with this viscoplastic model under monotonic loading. Then the evolution of the crack tip stress field under small scale creep (SSC) conditions is studied. Under this condition, inelastic strains are confined to the crack tip. The effect of cyclic loading on the near tip stress and strain fields is studied. Due to the complexity of cyclic loading, we focus on a simple class of loading history and the effect of stress ratio on the crack tip fields.

3.2 Material Model

The geometry used for monotonic and cyclic loading is the single edge crack tension specimen (SECT) shown schematically in Figure 3.1 with $a/b = 0.1$.

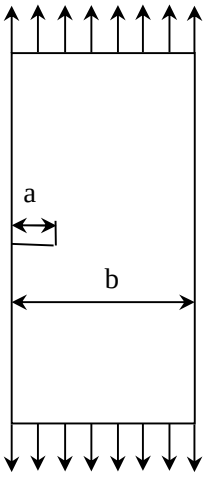

Figure 3.1 Single edge crack tension specimen

The material model is a unified viscoplastic model proposed by Chaboche(1989). The total strain rate $\dot{\varepsilon}_{ij}$ is the sum of the elastic strain rate $\dot{\varepsilon}^{\mathrm{e}}_{ij}$ and inelastic strain rate $\dot{\varepsilon}^{\mathrm{I}}_{ij}$, where a dot denotes differentiation with respect to time. The elastic strain rate is given by

$$\dot{\varepsilon}^{\mathrm{e}}_{ij} = \frac{1+\nu}{E}\dot{\sigma}_{ij} - \frac{\nu}{E}\dot{\sigma}_{kk}\delta_{ij}, \tag{3.1}$$

where σ_{ij} is the stress tensor, E is the Young's modulus and ν is the Poisson's ratio. The inelastic strain rate is given by

$$\dot{\varepsilon}^{\mathrm{I}}_{ij} = \frac{3}{2}\dot{p}\frac{\omega_{ij}}{\omega_{\mathrm{e}}}, \tag{3.2}$$

where

$$\dot{p} = \sqrt{\frac{2}{3}\dot{\varepsilon}^{\mathrm{I}}_{ij}\dot{\varepsilon}^{\mathrm{I}}_{ij}}, \tag{3.3}$$

is the effective inelastic strain rate and

$$\omega_{ij} = s_{ij} - x^{\mathrm{d}}_{ij} \tag{3.4}$$

is the difference between the stress deviatoric tensor s_{ij} and the deviator of the back stress tensor x_{ij}. Also,

$$\omega_e \equiv \sqrt{3\omega_{ij}\omega_{ij}/2} \tag{3.5}$$

The effective inelastic strain rate $\dot{p}$ is given by

$$\dot{p} = \left\langle f / Z \right\rangle^{N} \tag{3.6}$$

where Z and N are material constants. The symbol $\langle\ \rangle$ in (3.6) is defined by

$$\langle z \rangle = \begin{cases} z & z \geq 0 \\ 0 & z < 0 \end{cases} \tag{3.7}$$

In (3.7), f is the yield function defined by

$$f = \omega_{\mathrm{e}} - r - k \tag{3.8}$$

where R is an isotropic hardening variable and k is the initial radius of the yield surface. The elastic region is defined by $f \le 0$. The evolutionary law for the hardening variable R is given by

$$\dot{R} = c_3 (R_\infty - R)\dot{p} \tag{3.9}$$

where c_3 and R_∞ are isotropic hardening parameters, R_∞ is the steady state value of R, and c_3 controls the saturation rate. The back stress tensor (see(3.4)) x_{ij} is decomposed into two parts,

$$x_{ij} = \alpha_{ij} + \beta_{ij} \tag{3.10}$$

The state variables α_{ij}, β_{ij} evolve according to

$$\dot{\alpha}_{ij} = c_1 \left(a_1 \frac{\omega_{ij}}{\omega_e} - \alpha_{ij} \right) \dot{p}, \tag{3.11}$$

$$\dot{\beta}_{ij} = c_2 \left(a_2 \frac{\omega_{ij}}{\omega_e} - \beta_{ij} \right) \dot{p} \tag{3.12}$$

where c_1, c_2, a_1, a_2 are material constants. The first terms in (3.11), (3.12) are responsible for hardening whereas and the second terms model dynamic recovery. The steady state values of the back stresses are determined by a_1 and a_2 while the values of c_1 and c_2 control the rate by which the steady values are reached. Since $\left| \omega_{ij} / \omega_e \right| \le 1$, (3.11) and (3.12) imply that the back stresses are bounded by $a_1 + a_2$ at any inelastic strain rate.

This constitutive model contains 11 material parameters. These are: Young's modulus E, Poisson's ratio ν, the kinematic hardening parameters a_1, a_2, c_1, c_2, the isotropic hardening parameters c_3 and R_∞, the creep parameters Z and N, and the initial yield stress k. These parameters vary with temperature and have been determined from experimental data. Values used in this paper are for Alloy RR1000 at

650^{o}C (see Table 3.1 below). These data are taken from the papers of Zhao and Tong (2008) and (2007a).

3.3 Analytical Analysis of Monotonic Loading

3.3.1 Uniaxial Loading Behavior

Important insight into the structure of crack tip fields in the viscoplastic materials described above can be gained by examining the deformation of a straight bar in a creep test. For uniaxial loading, let $\sigma_{22} = \sigma$ be the applied tension to the bar at $t = 0$. A straightforward calculation shows that the equivalent effective stress is

$$\omega_{\mathrm{e}} = \left|\sigma - x_{22}\right|. \tag{3.13}$$

The inelastic strain rate in the loading direction is

$$\dot{\varepsilon}^{I}_{22} = \frac{3}{2}\,\dot{p}\,\frac{\omega_{22}}{\omega_{\mathrm{e}}}, \tag{3.14}$$

where

$$\omega_{22} / \omega_{\mathrm{e}} = \frac{2}{3}\frac{(\sigma - x_{22})}{\left|\sigma - x_{22}\right|}, \tag{3.15}$$

$$\dot{p} = \left\langle (\omega_{\mathrm{e}} - R - k) / Z \right\rangle^{N}. \tag{3.16}$$

Equation (3.14) can be rewritten as

$$\dot{\varepsilon}^{\mathrm{I}}_{22} = \dot{p}\,\mathrm{sgn}\left(\sigma - x_{22}\right) = \left\langle \left(\left|\sigma - x_{22}\right| - R - k\right) / Z \right\rangle^{N} \mathrm{sgn}\left(\sigma - x_{22}\right). \tag{3.17}$$

Assuming that $\varepsilon^{\mathrm{I}}_{22} = R = x_{22} = 0$ at $t = 0$, Equation (3.17) implies that the applied tension has to be greater than *k* for non-zero inelastic rate. For $\dot{p} > 0$, integrating(3.9), (3.11), (3.12) and using the initial conditions $\varepsilon^{\mathrm{I}}_{22} = R = x_{ij} = 0$ results in

$$R = R_{\infty}(1 - e^{-c_3 p}), \tag{3.18}$$

$$x_{22} = \frac{2a_1}{3}\left[1-e^{-c_1 p}\right]+\frac{2a_2}{3}\left[1-e^{-c_2 p}\right], \tag{3.19}$$

$$x_{11} = x_{33} = -\frac{a_1}{3}\left[1-e^{-c_1 p}\right]-\frac{a_2}{3}\left[1-e^{-c_2 p}\right]. \tag{3.20}$$

Substituting(3.18), (3.19) in (3.16) and assuming $\sigma - x_{22} > 0$ lead to the following expression for the inelastic strain rate:

$$\dot{\varepsilon}^I_{22} = \dot{p} = Z^{-N}\left[\sigma - \frac{2}{3}\left(a_1\left[1-e^{-c_1 p}\right]+a_2\left[1-e^{-c_2 p}\right]\right) - R_\infty\left(1-e^{-c_3 p}\right) - k\right]^N . \tag{3.21}$$

Equation (3.21) is a separable differential equation and can be integrated to find the inelastic strain as a function of time. Note, since $e^{-c_i p} \le 1$ in (3.21) the condition

$$\sigma > \frac{2}{3}(a_1 + a_2) + R_\infty + k \equiv \sigma^*, \tag{3.22}$$

ensures that $\dot{p} > 0$ for $t > 0$. In particular, if $\sigma >> \sigma^*$, the σ term inside the square bracket in (3.21) dominates, and

$$\dot{p} \approx Z^{-N}\sigma^N \tag{3.23}$$

Equation (3.23) shows that *at high stresses*, the inelastic behavior of the material is asymptotically identical to a power law creep material with creep coefficient *N*. This suggests that, near the crack tip, the viscoplastic constitutive model can be replaced by a power law creep model. Indeed, for $\sigma >> \sigma^*$, (3.23) implies that $p \approx \left(\sigma / Z\right)^N t$; substituting this into (3.18) and (3.19) gives

$$R \approx R_\infty\left(1-e^{-c_3 Z^{-N}\sigma^N t}\right) \tag{3.24}$$

$$x_{22} \approx \frac{2}{3}\left[a_1\left(1-e^{-c_1 Z^{-N}\sigma^N t}\right)+a_2\left(1-e^{-c_2 Z^{-N}\sigma^N t}\right)\right] \tag{3.25}$$

Equation (3.24) and (3.25) show that the state variables *R* and x_{22} reach their steady state values *exponentially fast*. The characteristic times needed to achieve

steady state are $(Z/\sigma)^N c_3^{-1}$ for the isotropic hardening variable R and $\max[(Z/\sigma)^N c_i^{-1}], i=1,2$ for the back stress x_{22} respectively. Note that these characteristic times are very sensitive to the stress level, i.e., higher stresses dramatically reduce the time needed to reach steady state. *This result suggests that the crack tip material is invariably governed by steady state behavior.* From (3.23) the characteristic time which determines how fast creep strain is accumulated is

$$t_1 \approx \left(Z/\sigma\right)^N \tag{3.26}$$

This characteristic time differs from the characteristic relaxation time of the internal variables by a factor of max[c_i^{-1}]. Since $c_i >> 1$ at high temperatures, the state variables evolve at a much faster rate than the inelastic strain. This behavior is consistent with the dominance of steady state behavior near the crack tip.

3.3.2 Asymptotic near tip Stress and Strain Fields

In this section we show that the asymptotic near tip fields is still governed by power law creep. Since our derivation of this result follows the same line of reasoning as the previous work of Stamm and Walz (Stamm and Walz 1993; Walz and Stamm 1993), we focus on the key ideas and our specific model since most of the mathematical details can be found in their work. In the following, (r,θ) denotes the polar coordinate of a material point. The crack tip occupies the origin where $r=0$.

The key idea is that the state variables reach *finite* steady state values at the crack tip. Indeed, (3.11) and (3.12) show that as one approaches the crack tip, the back stress tensor approaches the steady state

$$x_{ij}^{\infty} \equiv \left(a_1 + a_2\right)\left(\omega_{ij}/\omega_e\right)\Big|_{r=0} \tag{3.27}$$

Since we expect that the stress and strain fields approaches infinity at the crack tip, these steady state values of the back stresses are reached instantaneously at the crack tip. Note that $\left|\omega_{ij} / \omega_e\right| \le 1$, so these steady state values are always *bounded*. Denote

$$\left(\omega_{ij} / \omega_{\mathrm{e}}\right)\Big|_{r=0} \equiv \lim_{r\to 0} \omega_{ij} / \omega_{\mathrm{e}} \equiv \Omega(\theta) \tag{3.28}$$

Equations (3.27) and (3.28) imply that the state variables are bounded everywhere with their maximum values achieved at the crack tip at the instant of loading. As time increases, the region where the state variables achieved their steady state spreads out from the crack tip.

Since the state variables are bounded at their steady state values near the crack tip, we have

$$\omega_{ij} = s_{ij} - x_{ij}^d \approx s_{ij} \ , \ \omega_{\mathrm{e}} \approx \sqrt{\frac{3}{2} s_{ij} s_{ij}} = \sigma_{\mathrm{e}}, \tag{3.29}$$

$$\dot{p} = \left\langle \frac{\omega_{\mathrm{e}} - R - k}{Z} \right\rangle^N \approx \left(\frac{\sigma_{\mathrm{e}}}{Z} \right)^N . \tag{3.30}$$

Equations (3.29), (3.30) imply that the inelastic strain rate near the crack tip is governed by

$$\dot{\varepsilon}_{ij}^{\mathrm{I}} \approx \frac{3}{2} B \sigma_e^{N-1} s_{ij} \qquad B \equiv Z^{-N} \tag{3.31}$$

To leading order, the total strain rate near the crack tip is that of an EPLC material, i.e.,

$$\dot{\varepsilon}_{ij} = \frac{1+\nu}{E} \dot{\sigma}_{ij} - \frac{\nu}{E} \dot{\sigma}_{kk} \delta_{ij} + \frac{3}{2} B \sigma_e^{N-1} s_{ij} \tag{3.32}$$

For a stationary crack, the inelastic strain rates dominate the elastic strain rates as long as $N > 1$. Therefore, (3.31), (3.32) imply that the near tip stress and strain fields must be governed by the HRR field with a creep exponent N and creep coefficient B. Specifically, the stress field near the crack tip must have the form (Riedel and Rice 1980):

$$\sigma_{ij} = \left(\frac{D(t)}{BI_N r} \right)^{1/(N+1)} \tilde{\sigma}_{ij}(\theta, N) \quad r \to 0 \tag{3.33}$$

where $D(t)$ characterizes the amplitude of the singular field. In addition, since x_{ij} is bounded at the crack tip, we have

$$\Omega(\theta) = \lim_{r \to 0} \omega_{ij} / \omega_e \approx \tilde{s}_{ij}(\theta, N) / \tilde{\sigma}_e(\theta, N) \tag{3.34}$$

where $\tilde{s}_{ij}(\theta, N) \equiv \tilde{\sigma}_{ij}(\theta, N) - \tilde{\sigma}_{kk}(\theta, N)\delta_{ij} / 3$ and $\tilde{\sigma}_e(\theta, N) = \sqrt{3\tilde{s}_{ij}\tilde{s}_{ij} / 2}$.

Equations (3.27) and (3.34) show that the back stress tensor at the crack tip is completely determined by the material constants and angular variation of the HRR field. The evolution of the state variables near the crack tip can be estimated by substituting (3.34) into (3.9)-(3.12) and using (3.29), (3.30), the results are:

$$x_{ij} = \sum_{i=1}^{2} a_i \left[\frac{\tilde{s}_{ij}(\theta, N)}{\tilde{\sigma}_e(\theta, N)} \right] \left[1 - \exp\left(- \frac{Bc_i \left[\tilde{\sigma}_e(\theta, N) \right]^N}{\left(BI_N r \right)^{N/(N+1)}} \int_0^t \left(D(t') \right)^{N/(N+1)} dt' \right) \right] \tag{3.35}$$

$$R = R_\infty \left[1 - \exp\left(- \frac{Bc_3 \left[\tilde{\sigma}_e(\theta, N) \right]^N}{\left(BI_N r \right)^{N/(N+1)}} \int_0^t \left(D(t') \right)^{N/(N+1)} dt' \right) \right] \tag{3.36}$$

Note that, for any $t > 0$, the back stress tensor and the isotropic hardening variable approach their steady state values exponentially fast as $r \to 0$.

3.4 Finite Element Analysis (FEM) Simulation

3.4.1 Normalization

In the following, we normalize all lengths including displacements by the crack length, *a*, stresses by a_1 and time by τ where

$$\tau = \left(Z / a_1 \right)^N \tag{3.37}$$

All normalized variables are topped by a bar. All the derivatives with respect to the normalized time τ are denoted by prime. The normalized constitutive model is:

$$\varepsilon'^{e}_{ij} = \frac{1+\nu}{\bar{E}}\bar{\sigma}'_{ij} - \frac{\nu}{\bar{E}}\bar{\sigma}'_{kk}\delta_{ij} \tag{3.38}$$

$$\bar{\varepsilon}'^{\mathrm{I}}_{ij} = \frac{3}{2}\bar{p}'\frac{\bar{\omega}_{ij}}{\bar{\omega}_{\mathrm{e}}},\ \ \bar{\omega}_{\mathrm{e}} \equiv \sqrt{3\bar{\omega}_{ij}\bar{\omega}_{ij}/2} \tag{3.39}$$

$$\bar{p}' = \left\langle \bar{\omega}_{\mathrm{e}} - \bar{R} - \bar{k} \right\rangle^{N} \tag{3.40}$$

$$\bar{R}' = c_3(\bar{R}_{\infty} - \bar{R})\bar{p}' \tag{3.41}$$

$$\bar{\alpha}'_{ij} = c_1\left(\frac{\bar{\omega}_{ij}}{\bar{\omega}_{\mathrm{e}}} - \bar{\alpha}_{ij}\right)\bar{p}' \tag{3.42}$$

$$\bar{\beta}'_{ij} = c_2\left(\frac{a_2\bar{\omega}_{ij}}{a_1\bar{\omega}_{\mathrm{e}}} - \bar{\beta}_{ij}\right)\bar{p}' \tag{3.43}$$

A straightforward dimensional analysis shows that the governing equations and the boundary conditions contain the following dimensionless quantities:

$$c_2, c_1, c_3, N, \nu, a_2/a_1, \bar{k} = k/a_1, \bar{R}_{\infty} = R_{\infty}/a_1, \bar{\sigma}_{\infty} = \sigma_{\infty}/a_1, \bar{E} = E/a_1 \tag{3.44}$$

3.4.2 FE Model

Finite element analysis was carried out using the finite element software ABAQUS(2008). The constitutive model is implemented in ABAQUS through a user-defined material subroutine UMAT using the implicit backward Euler method under the assumption of small deformations. The finite element models are shown in Figure 3.2. The mesh consists of 4-noded bilinear plane strain quadrilateral element (CPE4). To capture the crack tip stress fields accurately, we used a sub modeling technique in ABAQUS (2008) to obtain detailed numerical solution at the crack tip by applying the

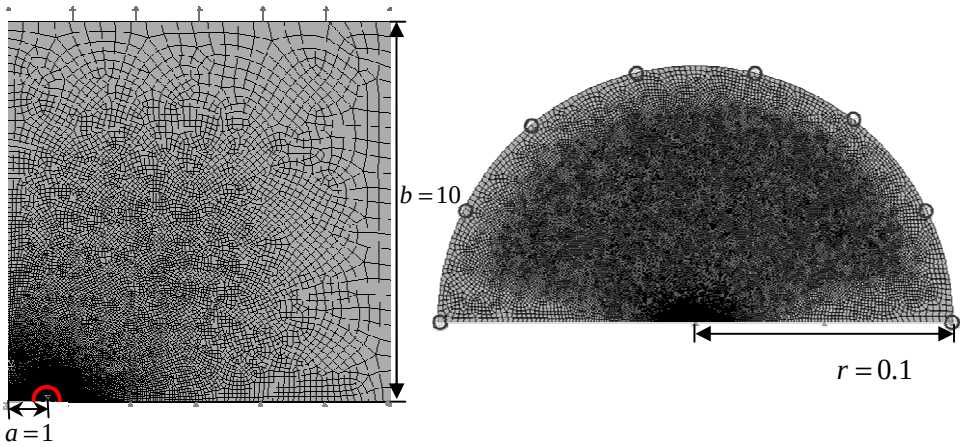

Figure 3.2 FE models for numerical simulation. (a) Finite element model for half of the specimen. The sub-model region ($r = 0.1$) is highlighted. (b) Semicircular FE sub-model with fine mesh

solution obtained using a coarse mesh as the boundary condition in the sub-model. A convergence study with respect to mesh and step size has been carried out. To capture the HRR field near the crack tip, the maximum size of the smallest element should be on the order of 10^{-5}. In all simulations, the smallest element size near the crack tip is on the order of 10^{-6} whereas the mesh size in the far field is on the order of 10^{-1}. Backward Euler scheme ensures numerical stability. A normalized time step size of 10^{-4} is used in the simulation. A convergence study shows that the solution remains unchanged with further reduction of the normalized time step size. The normalized parameters used in the simulations are calculated using the material parameter in Table 3.1(Zhan and Tong 2007a, b; Zhao and Tong 2008).

To verify the UMAT and the sub-modeling technique, we set all c_i and k to zero. This reduces the viscoplastic model to a power law creeping solid. We compare our numerical results with analytical solutions in the literature. Details are given in the Appendix 3.1.

3.4.3 Small Scale Creep (SSC)

For an EPLC material, creep deformation is always confined to the crack tip at sufficiently short times. This condition is known as small scale creep and was studied first by Riedel and Rice (1980). In this regime, the crack is modeled as semi-infinite with the far field boundary condition governed by the stress intensity factor K_I, i.e.,

$$\sigma_{ij} = \frac{K_I}{\sqrt{2\pi r}} \tilde{\sigma}_{ij}^{e}(\theta) \quad r \to \infty \tag{3.45}$$

For a constant load applied suddenly at time $t = 0$, Riedel and Rice (1980) have shown that near crack tip stress field is given by

$$\sigma_{ij} = \left(\frac{C(t)}{BI_N r} \right)^{1/(N+1)} \tilde{\sigma}_{ij}(\theta, N) \tag{3.46}$$

Table 3.1 Data for viscoplastic material (Zhan and Tong 2007a, b; Zhao and Tong 2008)

Parameters	Values
E	190 GPa
ν	0.285
Z	678.317 $\mathrm{MPa}\times\mathrm{s}^{-N}$
N	10
k	144.26 MPa
a_1	361.57 MPa
a_2	266.84 MPa
R_∞	161.52 MPa
c_1	391.61
c_2	2578.69
c_3	7.13

where $C(t)$ is the time-dependent stress amplitude of the singularity, I_N is a numerical factor dependents on N and $\tilde{\sigma}_{ij}$ is the angular variation of the HRR field. For short times, the stress and strain fields are self-similar whereas for long times, the creep strain will eventually dominate the elastic strain and $C(t) \to C^*$ where C^* is a path independent integral defined by Landes and Begley(1976) . The transition from short to long time behavior takes place at a time denoted by t_{R}, which is given by

$$t_{\mathrm{R}} = \frac{\alpha K_I^2 (1-\nu^2)}{(n+1)EC^*} \tag{3.47}$$

where $\alpha \approx 1$. Finite element calculations (Ehlers and Riedel 1981) showed that $C(t)$ can be approximated by:

$$C(t) \approx \left(1 + \frac{t_{\mathrm{R}}}{t}\right) C^* \tag{3.48}$$

In contrast, for a viscoplastic solid, as long as the applied load is sufficiently low, the region of non-zero inelastic strain is *always* confined to the crack tip region *for all times*. This is because the inelastic strain rate vanishes when $f \le 0$ (see (3.6) and (3.7)). The fact that the region of active creep is *confined by elastic material* implies that the inelastic strain rate *everywhere* has to vanish at very long times, as shown below.

With this background in mind, we consider the SSC problem in a viscoplastic solid. We assume that the applied load is sufficiently small so that inelastic zone is small compared with the region of dominance of the elastic K_I field. To be specific, consider a plane strain edge crack occupying $x \in (0, a), y = 0$ in an infinite strip of viscoplastic material (see Figure 3.1). At time $t = 0$, the crack is loaded by applying a constant remote tension:

$$\sigma_{22}(x, |y| \to \infty, t > 0) = \sigma_\infty \tag{3.49}$$

The boundary of the inelastic zone is determined by the condition $f = \omega_e - R - k = 0$. The maximum size of this creep zone r_c^{Max} can be estimated by setting $R = x_{ij} = 0$ and equating ω_e with k where ω_e is obtained from elastic K_I field. This results in:

$$r_c^{\text{Max}} = \frac{K_I^2}{2\pi k^2}\tilde{\sigma}_e(\theta) \tag{3.50}$$

SSC requires the condition $r_c^{Max} << a$ to be satisfied. For the single edged crack specimen shown in Figure 3.1, $K_I \cong 1.12\sigma_\infty\sqrt{\pi a}$ (Tada et al. 2000). Substituting this expression for stress intensity factor into (3.47), the condition for SCC is

$$\frac{\sigma_\infty^2}{k^2} << 1.6 \tag{3.51}$$

Our analysis in the previous section implies that the crack tip stresses must have the form:

$$\sigma_{ij} = \left(\frac{D(t)}{BI_N r}\right)^{1/(N+1)} \tilde{\sigma}_{ij}(\theta, N) \tag{3.52}$$

where $D(t)$ is a time dependent stress amplitude. The SSC problem was simulated in ABAQUS using the finite element model shown in Figure 3.2. To ensure SSC, the normalized remote load is set to 0.2 to satisfy(3.51). Figure 3.3 shows a log-log plot of the normalized stress $\bar{\sigma}_{22}$ directly ahead of the crack tip ($\theta = 0$) versus the normalized distance $\bar{d}$ at four different normalized times: 3.5e-3, 1.13,10,200. The two straight lines with slope of $-1/2$ and $-1/(N+1)$ denote the K field and HRR field singularity respectively.

Figure 3.3 shows that at distances close to the crack tip ($10^{-3} < \bar{d} < 10^{-1}$),the elastic *K* field dominates at *all times*, since the results the slope of the stress versus distance is approximately -1/2. Indeed, the numerical solution agrees with (3.45). This result is consistent with the SSC assumption. Very close to the crack tip, the elastic rate is no

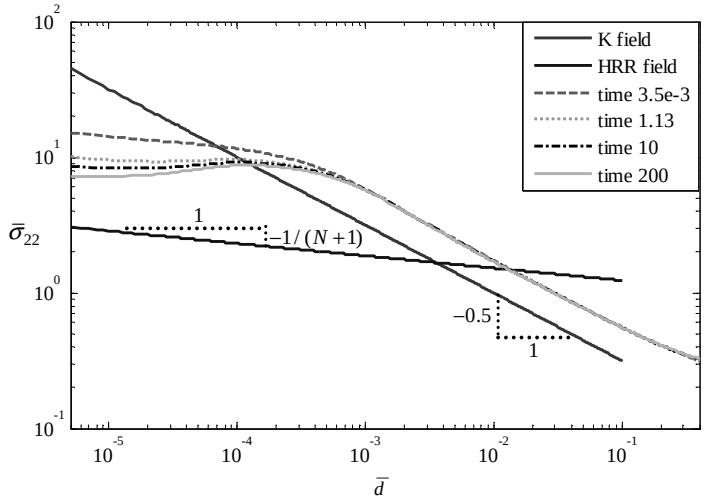

Figure 3.3 Normalized stress $\bar{\sigma}_{22}(r,\theta=0)$ versus normalized distance directly ahead of the crack tip at different normalized times. The two straight lines are indicating the slope of -1/2 and -1/(N+1) for comparison.

longer dominant, Figure 3.3 shows that stress near the crack tip at normalized times $\bar{t} = 3.5\text{e-}3$ exhibits the HRR singularity, consistent with (3.46). As time increases to 1.13, the region of validity of the HRR field decreases significantly and at longer times ($\bar{t} = 10,\ 200$), we observe no region of dominance of the HRR field. Stress relaxation near the crack tip is evident.

As mentioned earlier, we expect the HRR field and the inelastic strain rate to vanish with increasing time. To verify this hypothesis, the inelastic strain component ε_{22}^{I} versus normalized time $\bar{t} \in [10, 200]$ directly ahead of crack tip at $\bar{d} = 1\times10^{-5}$ is plotted in Figure 3.4. It shows that the inelastic strain rate is negative for $\bar{t} \in [10, 200]$. This result, together with (3.2) and (3.4), implies that $s_{22} - x_{22}^{d} < 0$. Recall that the existence of HRR field is based on the inequality $s_{ij} >> x_{ij}^{d}$, hence, the fact that $\varepsilon_{22}^{\mathrm{I}}$ decreases with time ($s_{22} - x_{22}^{d} < 0$) implies that the HRR field cannot be dominant, consistent with our result in Figure 3.3. Finally, note that the scale of the inelastic strain in Figure 3.4 is very fine, and $\varepsilon_{22}^{\mathrm{I}}$ almost approaches constant by normalized time 200. This result is also consistent with our hypothesis that the inelastic strain rate vanishes everywhere at very long times. Within the small scale creep regime, the region where creep occurs is always confined inside a small region near the crack tip where the surrounding material is elastic. This geometry confinement result causes the creep strain rate at a fixed material point to decrease with time at some point. This "back stress" is not due to microstructural changes in the dislocation structure but due to geometric constraint.

As a further check, we plot the normalized crack tip stress amplitude, $\bar{D}(t) = D(t)/D_1$ where $D_1 = D(\bar{t}_1 = 3.5\text{e}-3)$ in Figure 3.5. This figure shows that the normalized stress amplitude decreases with time for $\bar{t} > \bar{t}_1$ and approaches zero at longer times. The above analysis focuses on small applied loading where the inelastic strain is confined to the crack tip region. We believe this is an important regime as

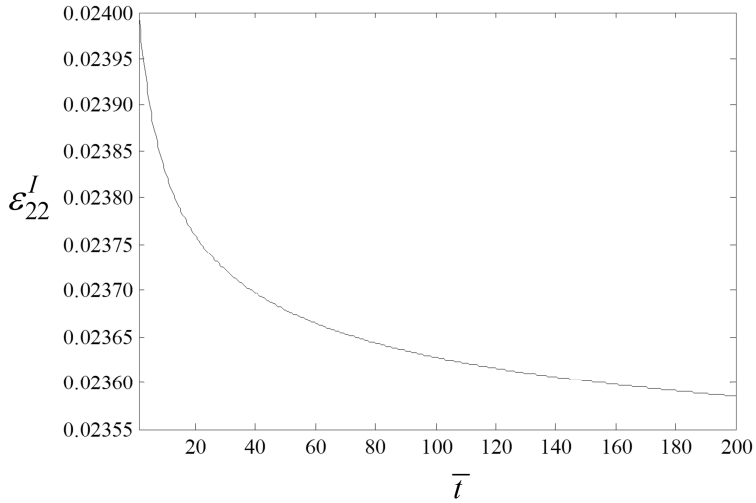

Figure 3.4 $\varepsilon_{22}^{\mathrm{I}}$ versus $\bar{t}$ at $\bar{d}=1\times10^{-5},\theta=0$

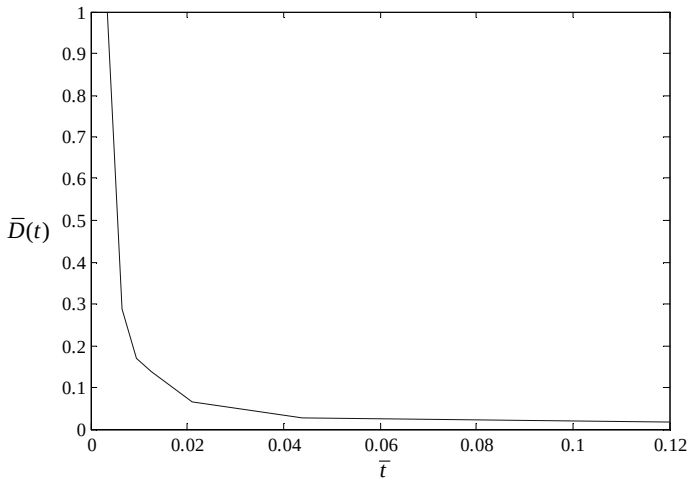

Figure 3.5 Normalized crack tip stress amplitude $\bar{D}(t)$ versus dimensionless time $\bar{t}$

most high temperature components are subjected to relatively low loads to prevent creep rupture. Nonetheless, another regime is when the applied stress σ_∞ exceeds σ^* defined by (3.22). In this case the specimen creeps everywhere and SSC is valid only for very short times. Eventually the elastic K_I field will disappear as inelastic deformation spreads throughout the specimen. In particular, if the applied stress $\sigma_\infty >> \sigma^*$, then the *entire* specimen creeps. In this case, the fracture mechanics should be well approximated by the EPLC material as demonstrated by Stamm and Walz (Stamm and Walz 1993; Walz and Stamm 1993).

3.5 Cyclic Loading

In this section we study the crack tip fields due to a simple class of cyclic loading which consists of trapezoidal load cycles on the SECT specimen in Figure 3.6. Since our focus is on the effect of stress ratio on the crack tip fields, we limit our simulations to waveforms where loading and unloading are much faster than the hold period. A schematic of the waveform is shown in Figure 3.6. Each cycle contains four parts: loading with duration 0.1, hold at $\bar{\sigma}_{\max}$ with normalized time 3, unloading with duration 0.1 and hold at $\bar{\sigma}_{\min}$ with normalized time 3 (see Figure 3.6(b)). The long normalized hold time allows for adequate stress relaxation. The normalized maximum stress amplitude is ($\bar{\sigma}_{\max} = 0.2$) so that the specimen is under SSC. Four different loading with stress ratios $S = \bar{\sigma}_{\min} / \bar{\sigma}_{\max} =$ 0, 0.2, 0.5 and 0.8 are considered.

For each of the four cycles (I,II,III,IV) labeled in Figure 3.6(a), we highlight the stress field at the three times (1,2,3) which correspond to the beginning ,the middle and the end of a hold period. A log-log plot of the stress component $\bar{\sigma}_{22}$ evaluated directly ahead of the crack tip versus the normalized distance $\bar{d}$ at these times for S = 0.5 are shown in Figure 3.7(a-c). Note that results for cycles (I,II,III,IV) at the same time lie approximately on top of each other in these figures, indicating that the stress

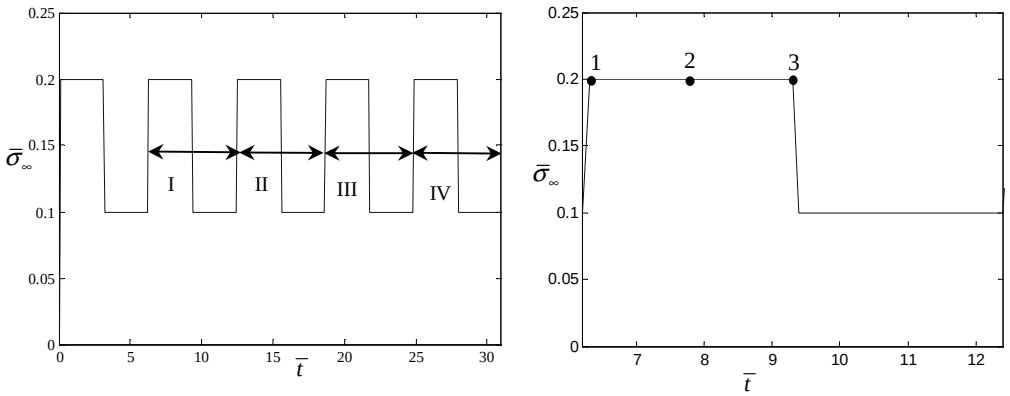

(a) (b)

Figure 3.6 Cyclic loading waveform with $S = 0.5$. (a) loading history. Four loading cycles (I,II,III,IV) are labeled. (b) a particular loading cycle. (1,2,3) represent three different times in the hold period in each cycle.

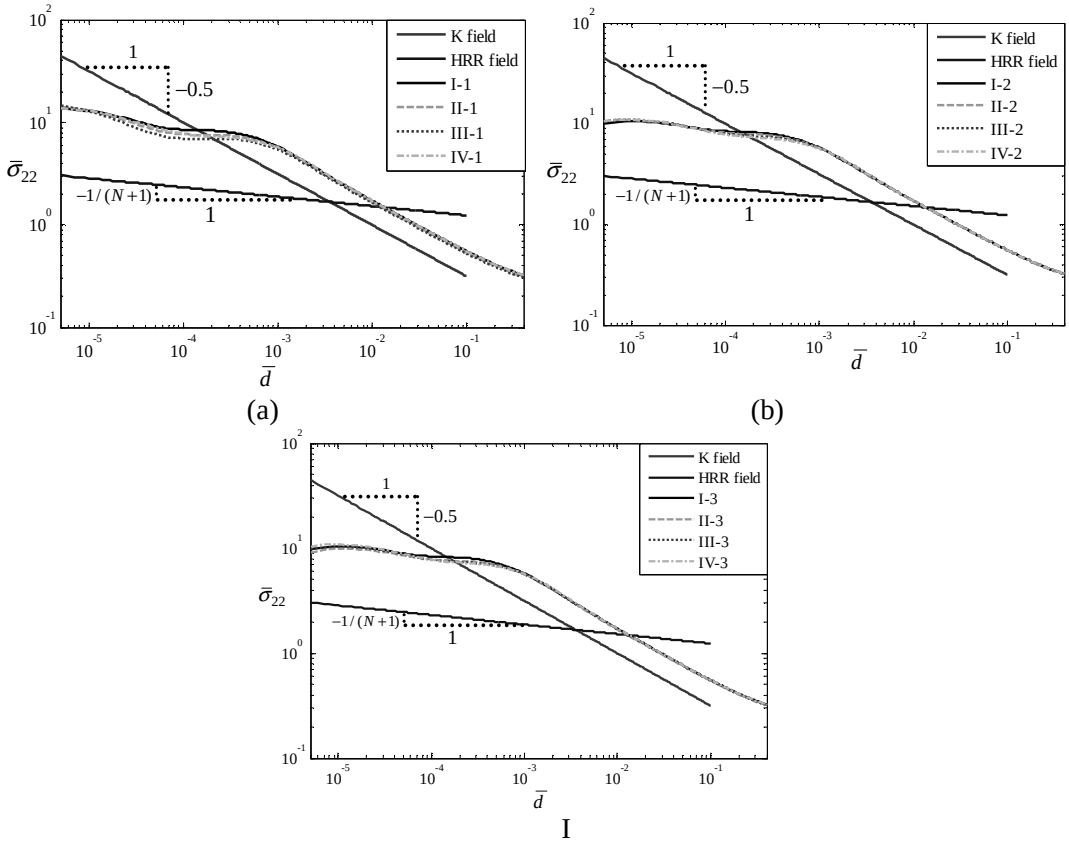

Figure 3.7 Normalized stress profiles for different times in a hold period. (a) at the beginning of hold, (b) at the middle of hold, (c) at the end of hold.

distributions are approximately cycle independent. Our numerical result shows that the stress fields do not vary from cycle to cycle after the second cycle, hence we do not report results in the first cycle, and cycle I labeled in Figure 3.7(a) is actually the second cycle. As shown in Figure 3.7(a), immediately after loading, the stress field near the crack tip does not show any HRR characteristics (the HRR field is indicated by the blue line with slope -1/(*N+1*)). This result is not surprising since loading is sufficiently fast so that the rate of creep deformation is small compared with the elastic strain rate. As time increases, Figure 3.7(b) shows that the HRR field begins to dominate near the crack tip. Note that, at the end of the hold period Figure 3.7(c), the region of dominance of the HRR field is smaller.

This result is consistent with our SSC analysis in the previous section since the inelastic strain rate will decrease at long times. Similar trends for the stress are found for the other loading cases with different stress ratios.

Next we investigate the effect of stress ratio *S* on the inelastic strain $\varepsilon_{22}^{\mathrm{I}}$. These results are presented at a fixed material point $\bar{d} = 1\times10^{-5}$ directly ahead of the crack tip. The time evolution of $\varepsilon_{22}^{\mathrm{I}}$ at this material point for *S* = 0, 0.2, 0.5 and 0.8 are plotted in Figure 3.8. A common feature of these figures is that $\varepsilon_{22}^{\mathrm{I}}$ *increases* in each cycle. This feature has been extensively studied in the literature (Chaboche and Nouailhas 1989a-b, 1989b-b; Ohno and Wang 1993; McDowell 1995; Yoshida 1990; Yaguchi and Takahashi 2005a, 2005b; Kang et al. 2002; Kang et al. 2006) for bars loaded under cyclic creep. For the material parameters used in our simulations, we found that the *increment* of inelastic strain per cycle, $\Delta\varepsilon_{22}^{\mathrm{I}}$, converges rapidly to a constant which is denoted by $\Delta\varepsilon_{22}^{\mathrm{I}}(\infty, S)$. The maximum inelastic strains accumulated per cycle and the value of $\Delta\varepsilon_{22}^{\mathrm{I}}(\infty, S)$ depend on the stress ratio. The *higher* the stress ratio *S*, the *less* the maximum strain accumulated at the same cycle. This effect is consistent with earlier calculation(Zhao and Tong 2008)and experimental observations

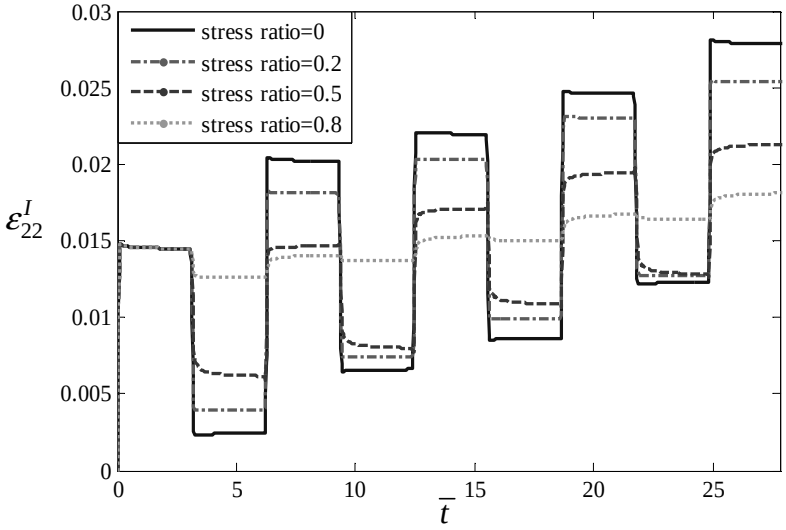

Figure 3.8 Crack tip strain $\varepsilon_{22}^{\mathrm{I}}$ at $\bar{d} = 1\times10^{-5}, \theta = 0$ for four stress ratios

(Yaguchi and Takahashi 2005a; Gupta et al. 2005) of uniaxial specimens loaded under cyclic conditions.

To understand these results, we plot the stress directly ahead of the crack tip at $\bar{d} = 1\times10^{-5}$ in Figure 3.9. It shows that immediately after loading, the stress $\bar{\sigma}_{22}$ associated with the stress ratio 0 is higher than that of *S = 0.8*. The stress increases is due to the rapid elastic loading resulting in a high stress peak near the crack for low stress ratios. As pointed out by Riedel (1983) in his analysis of creep fatigue crack tip fields in an EPLC material, these stress peaks are associated with an sudden increase in stress intensity factor due to rapid change in loading. This stress increase gives rise to a higher inelastic strain rate during the hold period. As a result, the inelastic strain increases with decreasing stress ratio.

3.6 Summary and Discussion

A numerical and analytical study on the asymptotic stress and strain field of a plane strain Mode I stationary crack in a viscoplastic material is presented in this chapter. The focus is on the regime of small scale creep where the region of inelastic strain is small in comparison with typical specimen dimensions. Analyses are carried out for a constant applied load and a simple class of cyclic loading history. Our asymptotic analysis shows that the near tip stress and strain fields are still governed by the HRR field. This result can be readily extended to viscoplastic materials with different creep functions, as long as the state variables reach steady state at large strains (Stamm and Walz 1993; Walz and Stamm 1993). The argument for the near tip stress and strain field can also be extended to a *growing* Mode I crack with growth rate $\dot{a}$. Since near the crack tip the material behavior is given by (3.31), the analysis of Hui and Riedel(1981) applies, so the near tip stress field for $N > 3$ is:

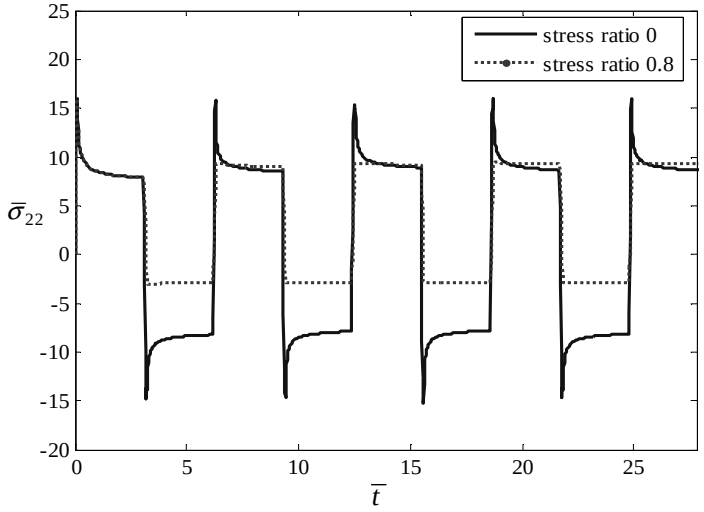

Figure 3.9 Crack tip stress σ_{22} at $\bar{d} = 1\times10^{-5}, \theta = 0$ for stress ratio 0 and 0.8

$$\sigma_{ij} = \alpha_N \left(\frac{\dot{a} Z^N}{Er} \right)^{1/(N-1)} \hat{\sigma}_{ij}(\theta, N) \tag{3.53}$$

where $\hat{\sigma}_{ij}$ are dimensionless functions describing the angular variations of the near tip fields and α_N is a numerical constant (see (Hui and Riedel 1981)).

Our solution for the SSC problem differs significantly from the well known solution for an EPLC solid, where the creep strain at a material increases monotonically with time and the amplitude of the stress field at the crack tip reaches a constant value (C^*). In our case, the creep strain at a material point near the crack tip first increases, then decreases to a constant value due to restraining stress exerted by the surrounding elastic material. As a result, the amplitude of the HRR field vanishes at long times. Therefore, if the applied load is small, the appropriate crack tip loading parameter is the elastic *K* field. This result is consistent with many creep crack growth experiments of super-alloys which suggested that the stress intensity factor correlates with the crack growth rate (Sadananda and Shahinian 1981; Fu 1980; Tong et al. 2001; Floreen and Kane 1979).

The effect of cyclic loading on the crack tip stress and strain fields are studied using four particular waveforms with different stress ratios but the same loading frequencies. Our waveform has rapid loading and unloading cycles. The hold times in our simulations are sufficiently long to allow for creep relaxation. In the beginning of a hold period, the elastic *K* field is dominant, and the region of HRR field is small. As time increases, the HRR field starts to dominate. For longer times, the region of dominance of the HRR decreases with time. For the material parameters used in this chapter, we find the stress distribution rapidly becomes cycle independent. This rapid convergence of a cycle independent stress state is controlled by the material parameters c_i and is particularly sensitive to the stress level ((3.35)-(3.36)). The larger the c_i and the higher the stress, the faster the rate of convergence. The ratcheting strain

is found to decrease with stress ratio.

There is obvious limitation in our analysis. We did not investigate the effect of loading frequency on the crack tip fields. Also, the hold times in all our simulations are identical. The dependence of crack tip fields on hold times and frequencies will be presented in a future work. More importantly, the micromechanics of local damage processes such as grain boundary cavitation are not included in our analysis. For Nickel-based super alloys, environmental effects such as oxidation embrittlement have been cited as the main cause of intergranular cracking for static and long dwell loading conditions(Saxena and Bassani 1984; Floreen and Kane 1979; Tong et al. 2001) .

Appendix 3.1 Verification of the FEM implementation

To verify the UMAT and the sub-modeling technique, we carried out simulations in a single edge cracked test (SECT) specimen. Sub-modeling can provide more detailed and accurate local solutions by applying the previously calculated global solution as the boundary condition (Krishnan et al. 2008). To validate our FEM, the constitutive model was reduced to an EPLC model by setting c_1, c_2, c_3 and k in (3.40)-(3.43) to zero. A normalized remote stress 0.2 is applied to the SECT specimen). Figure 3.10 shows the log-log plot of the stress component σ_{22} versus distance directly ahead of the crack tip. The stress obtained from the global model (coarser mesh) is indicated by the dotted line. The stress obtained using the sub-model (finer mesh) is indicated by the dash line. Note that there is a large overlap region where both models agree, which validates this sub-modeling technique. The inverse square root singularity associated with the elastic K_I field occurs in this overlap region. Log-log plots of crack tip σ_{22} field at different times are given in Figure 3.11. As time increases the stress near the crack tip is controlled by the HRR singularity which appears as a straight line with slope $-1/(N+1)$.

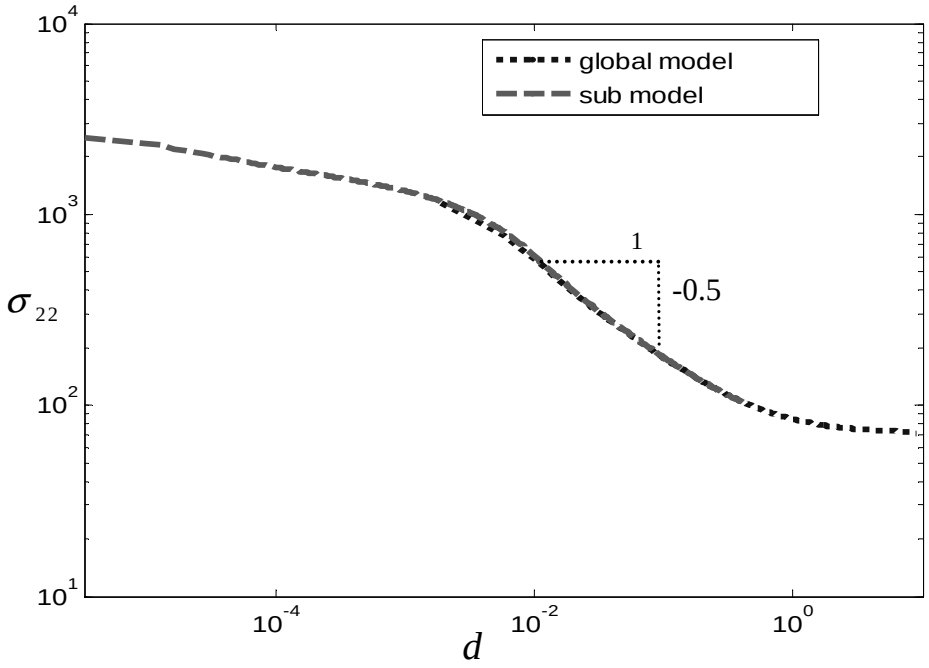

Figure 3.10 Verification of the sub-modeling technique

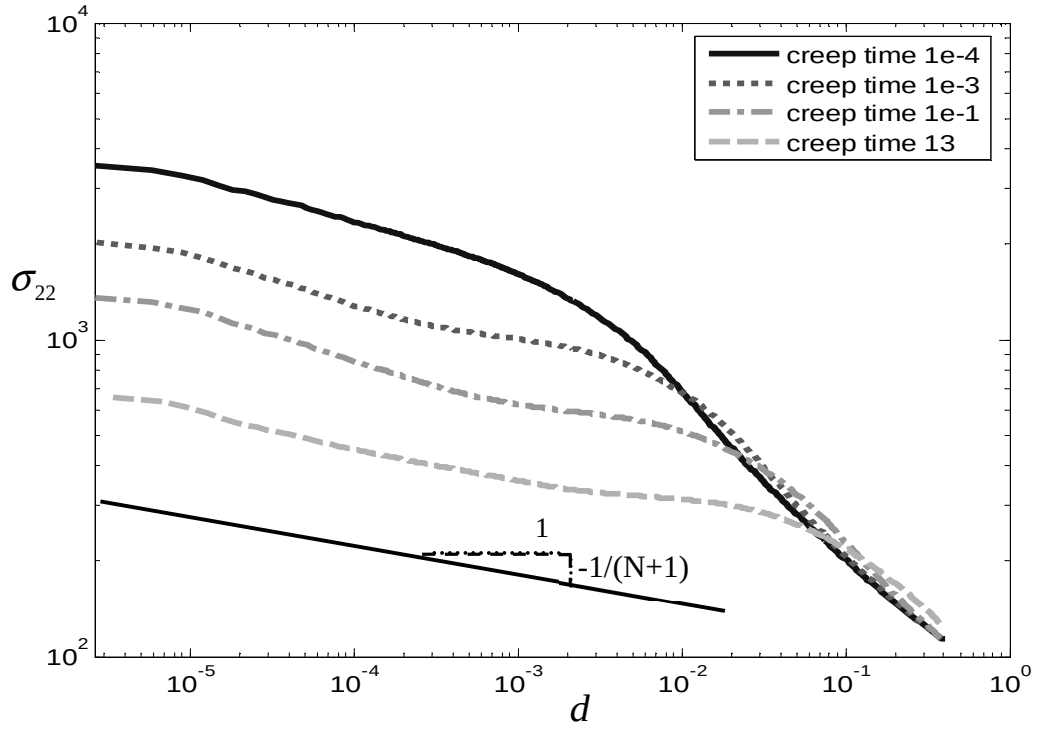

Figure 3.11 Log-log plot of the stress versus distance ahead of crack tip at different times

REFERENCES

ABAQUS (2008) version 6.8-3. Dassault Systemes SIMULIA Corp.

Adefris N, Saxena A, McDowell D (1996a) Creep fatigue crack growth behavior in 1Cr-1Mo-0.25V steels. Part I: Estimation of crack tip parameters. Fatigue Fract Eng Mater Struct 19:387-398

Adefris N, Saxena A, McDowell D (1996b) Creep fatigue crack growth behavior in 1Cr-1Mo-0.25V steels. Part II: Crack growth behavior and models. Fatigue Fract Eng Mater Struct 19:401-411

Atluri SN (1982) Path-independent integrals in finite elasticity and inelasticity, with body forces, inertia, and arbitrary crack-face conditions. Eng Fract Mech 16:341-364

Bassani J, McClintock F (1981) Creep relaxation of stress around a crack tip. Int J Solids Struct 17:479-492

Bassani JL, Hawk DE, Saxana A (1989) Evaluation of the C_t Parameter for Characterizing the Creep Crack Growth Rate in the Transient Regime. In: Saxana A, Landes JD, Bassani JL (eds) Third International Symposium on Nonlinear Fracture Mechanics, Knoxville, 1989. American Society for Testing and Materials, pp 7-26

Chaboche J (2008) A review of some plasticity and viscoplasticity constitutive theories. Int J Plast 24:1642-1693

Chaboche J, Nouailhas D (1989a) Constitutive Modeling of Ratchetting Effects—Part I: Experimental Facts and Properties of the Classical Models. J Eng Mater Technol 111:384

Chaboche J, Nouailhas D (1989b) Constitutive Modeling of Ratchetting Effects—Part II: Possibilities of Some Additional Kinematic Rules. J Eng Mater Technol 111:409

Chaboche JL (1989) Constitutive equations for cyclic plasticity and cyclic viscoplasticity. Int J Plast 5:247-302

Chomette S, Gentzbittel JM, Viguier B (2010) Creep behaviour of as received, aged and cold worked INCONEL 617 at 850° C and 950° C. J Nucl Mater 399:266-274

Cook R (1984) Creep properties of Inconel-617 in air and helium at 800 to 1000° C. Nucl Technol 66:283-288

Ehlers R, Riedel H (1981) A finite element analysis of creep deformation in a specimen containing a macroscopic crack. In: Francois D (ed) Fifth International Conference on Fracture, London, 1981. Pergamon Press, pp 691-698

Floreen S, Kane R (1979) An investigation of the crack fatigue environment interaction in a Ni base superalloy. Fatigue Fract Eng Mater Struct 2:401-412

Fu L (1980) Creep crack growth in technical alloys at elevated temperature--a review. Eng Fract Mech 13:307-330

Grover P, Saxena A (1999) Modelling the effect of creep-fatigue interaction on crack growth. Fatigue Fract Eng Mater Struct 22:111-122

Gupta C, Chakravartty J, Reddy G, Banerjee S (2005) Uniaxial cyclic deformation behaviour of SA 333 Gr 6 piping steel at room temperature. Int J Press Vessels Pip 82:459-469

Hall D, McDowell D, Saxena A (1998) Crack tip parameters for creep-brittle crack growth. Fatigue Fract Eng Mater Struct 21:387-401

Hui C, Riedel H (1981) The asymptotic stress and strain field near the tip of a growing crack under creep conditions. Int J Fract 17:409-425

Kang G, Gao Q, Cai L, Sun Y (2002) Experimental study on uniaxial and nonproportionally multiaxial ratcheting of SS304 stainless steel at room and high temperatures. Nucl Eng Des 216:13-26

Kang G, Kan Q, Zhang J, Sun Y (2006) Time-dependent ratchetting experiments of SS304 stainless steel. Int J Plast 22:858-894

Krishnan VR, Hui CY, Long R (2008) Finite strain crack tip fields in soft incompressible elastic solids. Langmuir 24:14245-14253

Kurata Y, Nakajima H (1995) Temperature dependence of creep properties of cold-worked Hastelloy XR. J Nucl Sci Technol 32:539-546

Landes J, Begley J (1976) A fracture mechanics approach to creep crack growth. Mechanics of crack growth:128-148

McDowell D (1995) Stress state dependence of cyclic ratchetting behavior of two rail steels. Int J Plast 11:397-421

Ohno N (1990) Recent topics in constitutive modeling of cyclic plasticity and viscoplasticity. Appl Mech Rev 43:283-295

Ohno N, Wang JD (1993) Kinematic hardening rules with critical state of dynamic recovery, part I: formulation and basic features for ratchetting behavior. Int J Plast 9:375-390

Riedel H (1981) Creep deformation at crack tips in elastic-viscoplastic solids. J Mech Phys Solids 29:35-49

Riedel H (1983) Crack-tip stress fields and crack growth under creep-fatigue conditions. In: Shih CF, Gudas JP (eds) Second International Symposium on Elastic-Plastic Fracture Mechanics, 1983. American Society for Testing and Materials, pp I505-I520

Riedel H, Rice JR (1980) Tensile cracks in creeping solids. In: Paris PC (ed) Fracture mechanics: twelfth conference, Philadelphia, 1980. American Society for Testing and Materials, pp 112-130

Sadananda K, Shahinian P (1981) Review of the fracture mechanics approach to creep crack growth in structural alloys. Eng Fract Mech 15:327-342

Saxena A (1986) Creep crack growth under non-steady-state conditions. ASTM Spec Tech Publ:185-201

Saxena A, Bassani JL (1984) Time-dependent fatigue crack growth behavior at elevated temperature. In: Wells JM, Landes JD (eds) Fracture: Interactions of Microstructure Mechanisms and Mechanics, 1984. The Metallurgical Society of AIME, pp 357-383

Schapery RA (1986) Time-dependent fracture: continuum aspects of crack growth. In: Bever M (ed) Encyclopedia of materials science and engineering, 1986. Pergamon Press, pp 5043-5053

Schneider K, Hartnagel W, Iischner B, Schepp P (1984) Creep behavior of materials for high-temperature reactor application. Nucl Technol 66:289-295

Schubert F, te Heesen E, Bruch U, Cook R, Diehl H, Ennis P, Jakobeit W, Penkalla H, Ullrich G (1984) Creep rupture behavior of candidate materials for nuclear process heat applications. Nucl Technol 66:227-240

Stamm H, Walz G (1993) Analytical investigation of crack tip fields in viscoplastic materials. Int J Fract 64:135-155

Tada H, Paris PC, Irwin GR (2000) The stress analysis of cracks handbook. Third edn. ASME, New York

Tong J, Dalby S, Byrne J, Henderson M, Hardy M (2001) Creep, fatigue and oxidation in crack growth in advanced nickel base superalloys. Int J Fatigue 23:897-902

Walz G, Stamm H (1993) Numerical investigation of crack tip fields in viscoplastic materials. Int J Fract 64:157-178

Wang W, Yuan F, Takao Y (2000) A unified loading parameter for creep-crack growth. Proceedings of the Royal Society of London Series A: Mathematical, Physical and Engineering Sciences 456:163-183

Yaguchi M, Takahashi Y (2005a) Ratchetting of viscoplastic material with cyclic softening, part 1: experiments on modified 9Cr-1Mo steel. Int J Plast 21:43-65

Yaguchi M, Takahashi Y (2005b) Ratchetting of viscoplastic material with cyclic softening, part 2: application of constitutive models. Int J Plast 21:835-860

Yoon KB, Saxena A, McDowell DL (1992) Influence of crack-tip cyclic plasticity on creep-fatigue crack growth. In: Ernst HA, Saxena A, McDowell DL (eds) Fracture Mechanics: Twenty-Second Symposium, Philadelphia, 1992. American Society for Testing and Materials, pp 367-392

Yoshida F (1990) Uniaxial and biaxial creep-ratcheting behavior of SUS304 stainless steel at room temperature. Int J Press Vessels Pip 44:207-223

Zhan ZL, Tong J (2007a) A study of cyclic plasticity and viscoplasticity in a new nickel-based superalloy using unified constitutive equations. Part I: Evaluation and determination of material parameters. Mech Mater 39:64-72

Zhan ZL, Tong J (2007b) A study of cyclic plasticity and viscoplasticity in a new nickel-based superalloy using unified constitutive equations. Part II: Simulation of cyclic stress relaxation. Mech Mater 39:73-80

Zhao L, Tong J (2008) A viscoplastic study of crack-tip deformation and crack growth in a nickel-based superalloy at elevated temperature. J Mech Phys Solids 56:3363-3378

CHAPTER 4

PLANAR DEFORMATION OF RANDOM SIZED POWER LAW CREEPING GRAINS WITH SLIDING AND CAVITATING GRAIN BOUNDARIES

PART I: CAVITY NUCLEATION AND GROWTH

4.1 Introduction

Designing for creep rupture is essential for elevated temperature components such as gas turbines, steam boilers and heat exchangers. For example, many structural components in nuclear power plants have a design life of 60 years. However, it is difficult to conduct creep experiments for such a long period of time. The current approach is to extrapolate short-term, high stress creep rupture data to long-term, low stress operating conditions using empirically based time-temperature parameters such as the Larson-Miller parameter (Larson and Miller 1952). This approach may lead to non-conservative design limits because the failure mechanisms in short term and long term tests can be different. A discussion of the difficulties associated with extrapolation of creep rupture data can be found in Ashby et al (1979).

A more consistent way of extrapolating creep rupture data is to supplement short term test information with fracture mechanism maps (Wray 1969). Briefly, a fracture mechanism map shows fields of dominance of particular creep rupture mechanisms in stress-temperature (or rupture time-temperature) space. Maps for over 40 materials covering pure metals and commercial alloys can be found in Gandhi and Ashby (1979) and Fields et al (1980). For example, the dominating fracture mechanism at low stresses and elevated temperatures for ferritic and austenistic steels is intergranular cavitation. In this regime, grain boundary cavities nucleate on grain boundaries that are under normal tension. Extensive research has shown that grain

boundary cavities can grow by grain boundary sliding(Evans 1971), stress-assisted diffusion of atoms from the cavity surface to the grain boundaries (Hull and Rimmer 1959; Chuang et al. 1979b; Needleman and Rice 1980), and by creep deformation of the surrounding grains (Hancock 1976; Budiansky et al. 1982). An excellent review of these micromechanical damage mechanisms can be found in Riedel's book on high temperature fracture (Riedel 1987).

Computational modeling based on micro-mechanics of creep damage processes such as those mentioned above can be used to alleviate the limitations of extrapolation and has been carried out by many investigators over the past thirty years. Numerical and approximate analytical solutions of a single cavity or an array of equally spaced cavities along an isolated grain boundary surrounded by power-law creeping or rigid grains have been developed by various investigators to quantify the effect of cavitation on creep deformation. These models form the basis for a continuum description of grain boundary separation where different oriented grain boundaries interact with each other. These continuum grain boundary separation models have been used extensively to study creep deformation of two dimensional polycrystalline microstructures consisting a periodic array of power-law creeping hexagonal grains (Riedel 1984; Van der Giessen and Tvergaard 1991; Van der Giessen and Tvergaard 1994; Onck and Van der Giessen 1997; Onck and Van der Giessen 1998). There are also numerical studies where grain deformation is modeled by rate-dependent crystal plasticity based constitutive models (Bower and Wininger 2004). This approach is computationally expensive so that only a limited number of grains can be simulated. More importantly, many of the intergranular cavitation models are based on the assumption that grain deformation can be modeled by elastic-power-law creep. For these reasons, we model the grains as an elastic power-law creeping material in this chapter.

So far, practically all numerical studies focus on uniform size grains with hexagonal shapes. In this chapter we use a representative volume element (RVE) where grains are non-uniform in size and randomly distributed. The RVE is generated using Voronoi tessellation. It should be noted that multi-grain random structures have been used to study crack initiation and propagation along grain boundaries in Aluminum alloys (Iesulauro et al. 2002). Since high temperature applications are not the focus of their work, grain boundary cavitation and sliding are not incorporated into their cohesive zone model. In our model, each grain is treated as a continuum and deforms by elastic-power-law creep. Grain boundary sliding and grain boundary separation due to cavity nucleation and growth are simulated using the equations summarized by Onck and Van der Giessen (1998). Specifically, these equations are implemented into a cohesive zone model (CZM) which allows us to compute grain boundary separation and slip as a function of loading history. Calculations are carried out for uniaxial creep and relaxation tests using periodic boundary conditions. It has been shown by various researchers (Terada et al. 2000; Kanit et al. 2003; Larsson et al. 2011) that periodic boundary condition increases the convergence rate of numerical results with increasing RVE size. Several advantages of the approach used in our work are: (1) a more realistic microstructure is modeled using RVE where grains are randomly distributed, (2) random creep behavior of grains (e.g. different grains can have different creep exponents and coefficients) can be incorporated into the FEM code , (3) complex grain boundary damage mechanism which is described by CZM is integrated into a commercial finite element software (ABAQUS) where parallelization computation can be carried out if desired.

The outline of this chapter is as follows. In section 4.2 we summarize the equations governing grain deformation and a CZM which incorporates damage due to cavitation and grain boundary sliding. The normalization of all the governing

equations is carried out in section 4.3. To gain insight, we analyze the CZM in section 4.4 using a simple loading history and show that the grain boundary cavitation model predicts interfacial failure. Details of our numerical implementation using ABAQUS is given in section 4.5. Finite element results for relaxation test and uniaxial tension test are presented in section 4.6 and 4.7 respectively. Finally, summary and discussion are given in section 4.8.

4.2 Constitutive Model

We assume that grains deform by elastic-power-law creep according to

$$\dot{\varepsilon}_{ij} = \dot{\varepsilon}_{ij}^{\mathrm{e}} + \dot{\varepsilon}_{ij}^{\mathrm{C}}, \tag{4.1}$$

$$\dot{\varepsilon}_{ij}^{\mathrm{e}} = \frac{1+\nu}{E}\dot{\sigma}_{ij} - \frac{\nu}{E}\dot{\sigma}_{kk}\delta_{ij}, \tag{4.2}$$

$$\dot{\varepsilon}_{ij}^{\mathrm{C}} = \frac{3}{2}B\sigma_{\mathrm{e}}^{\mathrm{n}}\frac{s_{ij}}{\sigma_{\mathrm{e}}}. \tag{4.3}$$

where a dot denotes time derivative, $\dot{\varepsilon}_{ij}$ is the total strain rate, $\dot{\varepsilon}_{ij}^{\mathrm{e}}$ is the elastic strain rate , $\dot{\varepsilon}_{ij}^{\mathrm{C}}$ is the creep strain rate. σ_{ij} is the stress tensor, E is the Young's modulus and ν is the Poisson's ratio, s_{ij} is the stress deviatoric tensor , σ_{e} is the von-Mises stress, B and n are the power law creep coefficient and exponent respectively.

Grain boundary sliding is modeled based on a theory proposed by Raj and Ashby (1971). In this model, the relative grain boundary sliding rate $\dot{u}_{\mathrm{s}}$ is directly proportional to shear stress τ along the grain boundary, i.e.,

$$\dot{u}_{\mathrm{s}} = \frac{\tau}{\eta_{\mathrm{b}}} \tag{4.4}$$

where η_{b} is the grain boundary viscosity.

Cavity nucleation and growth along a grain boundary facet leads to normal separation of the two adjacent grains. This separation is denoted by δ and the rate of

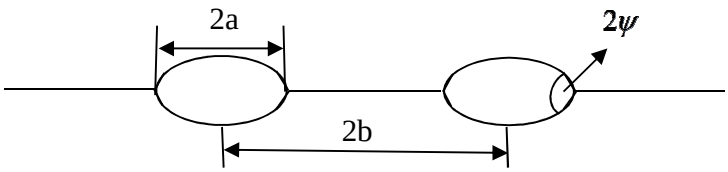

Figure 4.1 Periodically spaced cavities along a grain boundary

separation $\dot{\delta}$ is estimated using a continuum model where discrete periodically spaced voids in an infinite power law creeping material are subjected to a far field multi-axial stress state. Details can be found in Onck and Van der Giessen and the references within (Onck and Van der Giessen 1998). Here we briefly summarize their results. For a grain boundary facet with periodically spaced cavities as shown in Figure 4.1, δ is approximated in a averaged sense by $\delta = V / \pi b^2$ where V is the cavity volume given by

$$V = \frac{4\pi}{3} a^3 h(\psi), h(\psi) = (\frac{1}{1+\cos\psi} - \frac{1}{2}\cos\psi)\frac{1}{\sin\psi}, \tag{4.5}$$

where a is the cavity radius, $2b$ is the spacing between two adjacent cavities, 2ψ is the dihedral angle of the cavity. The grain boundary separation rate $\dot{\delta}$ is

$$\dot{\delta} = \frac{\dot{V}}{\pi b^2} - \frac{2V}{\pi b^2}\frac{\dot{b}}{b} \tag{4.6}$$

where $\dot{V}$ is the cavity volume growth rate. The second term in (4.6) depends on whether new cavities can nucleate. According to Onck and Van der Giessen, nucleation occurs if a dimensionless parameter S exceeds its threshold value S_{thr}, i.e.,

$$S = \left(\frac{\sigma_{\text{n}}}{\Sigma_0}\right)^2 \varepsilon_{\text{e}}^{\text{C}} > S_{\text{thr}} = \frac{N_{\text{I}}}{F_{\text{n}}} \tag{4.7}$$

Note that S is a combination of the normal traction σ_{n} at a continuum point along a grain boundary and the effective creep strain $\varepsilon_{\text{e}}^{\text{C}}$ at distances far from the cavity nuclei. Σ_0 is a stress normalization factor, N_{I} is the initial cavity density (number of cavity per unit undeformed area), and F_{n} is a material parameter with the unit of cavity density. A higher value of F_{n} indicates more active cavity nucleation.

If the nucleation condition (4.7) is satisfied, then the second term in (4.6) is given by

$$\frac{\dot{b}}{b} = -\frac{1}{2}\frac{\dot{N}}{N} \tag{4.8}$$

where N is the cavity density and its rate $\dot{N}$ is given by

$$\dot{N} = F_{\mathrm{n}}\left(\frac{\sigma_{\mathrm{n}}}{\Sigma_0}\right)^2 \dot{\varepsilon}_{\mathrm{e}}^{\mathrm{C}} \tag{4.9}$$

The cavity volume growth rate $\dot{V}$ in (4.6) is computed using

$$\dot{V} = \dot{V}_1 + \dot{V}_2 \tag{4.10}$$

where $\dot{V}_1$ is the volume growth rate due to coupling of grain boundary diffusion and power law creep and it is given by(Needleman and Rice 1980; Chen and Argon 1981):

$$\dot{V}_1 = 4\pi D\left[\frac{\sigma_{\mathrm{n}} - (1-f)\sigma_{\mathrm{s}}}{q(f)}\right], q(f) = 2\ln(1/f) - (3-f)(1-f) \tag{4.11}$$

with

$$f = \max\left[\left(\frac{a}{b}\right)^2, \left(\frac{a}{a+1.5L}\right)^2\right],\ L \equiv \left(D\sigma_{\mathrm{e}} / \dot{\varepsilon}_{\mathrm{e}}^{\mathrm{C}}\right)^{1/3} \tag{4.12}$$

where D is the grain boundary diffusivity, σ_{s} is the sintering stress which is usually small and it is neglected in our analysis, L is the diffusive length. For large L, $\dot{V}_1$ is the cavity diffusive growth rate obtained in the rigid grain limit. For small L, cavity growth is controlled by power law creep of the surrounding material (Dyson 1976).

The second term $\dot{V}_2$ in (4.10) is based on the results of a spherical void under triaxial stressing (Budiansky et al. 1982), later modified by Sham and Needleman (1983) and it is given by

$$\dot{V}_2 = \begin{cases} 2\pi a^3 \dot{\varepsilon}_{\mathrm{e}}^{\mathrm{C}} h(\psi)\left[\frac{3}{2n}\left|\frac{\sigma_{\mathrm{m}}}{\sigma_{\mathrm{e}}}\right| + \frac{(n-1)(n+0.4319)}{n^2}\right]^n, & \left|\frac{\sigma_{\mathrm{m}}}{\sigma_{\mathrm{e}}}\right| > 1 \\ 2\pi a^3 \dot{\varepsilon}_{\mathrm{e}}^{\mathrm{C}} h(\psi)\left[\frac{3}{2n} + \frac{(n-1)(n+0.4319)}{n^2}\right]\frac{\sigma_{\mathrm{m}}}{\sigma_{\mathrm{e}}}, & \left|\frac{\sigma_{\mathrm{m}}}{\sigma_{\mathrm{e}}}\right| \le 1 \end{cases} \tag{4.13}$$

where σ_{m} is mean stress. Both σ_{e} and σ_{m} are local quantities on the scale of grain sizes, but remote quantities on the scale of cavities. In our simulation, σ_{e}, $\varepsilon_{\mathrm{e}}^{\mathrm{C}}$, $\dot{\varepsilon}_{\mathrm{e}}^{\mathrm{C}}$, σ_{m} are quantities evaluated as the average of the two neighboring grains located at either side of a grain boundary facet.

4.3 Normalization

The following normalization is carried out to reduce the number of material and geometrical parameters in our analysis.

$$\begin{aligned}\bar{\sigma} &= \frac{\sigma}{\Sigma_0}, \bar{t} = \frac{t}{t_{\mathrm{c}}}, \bar{N} = \frac{N}{N_{\mathrm{I}}}, \bar{F}_n = \frac{F_{\mathrm{n}}}{N_{\mathrm{I}}}, \bar{a} = \frac{a}{a_0}, \\ \bar{b} &= \frac{b}{b_0}, \bar{V} = \frac{V}{V_0}, \bar{\delta} = \frac{\delta}{\delta_0}, \bar{L} = \frac{L}{a_0}, \bar{u}_s = \frac{u_{\mathrm{s}}}{R_{\mathrm{I}}}\end{aligned} \tag{4.14}$$

where t_{c} is the characteristic time given by $1/B\Sigma_0^n$, $2R_{\mathrm{I}}$ is the typical width of a grain boundary facet which is approximately $50\,\mu\mathrm{m}$ for our choice of RVE, N_{I} is the initial cavity density given by $40/\pi R_{\mathrm{I}}^2$, $a_0, 2b_0, V_0$,are the initial cavity radius, spacing and volume respectively. δ_0 is the initial separation of the grain boundary due to pre-existing voids given by $V_0/\pi b_0^2$.

In the following, all normalized variables are topped by a bar. The derivative with respect to normalized time is denoted by a prime instead of a dot.

The elastic-power-law creep equations for grain deformation are

$$\varepsilon_{ij}' = \varepsilon_{ij}'^{\mathrm{e}} + \varepsilon_{ij}'^{\mathrm{C}} \tag{4.15}$$

$$\varepsilon_{ij}'^{\mathrm{e}} = \frac{1+\nu}{\bar{E}}\bar{\sigma}_{ij}' - \frac{\nu}{\bar{E}}\bar{\sigma}_{kk}'\delta_{ij}, \tag{4.16}$$

$$\varepsilon_{ij}'^{\mathrm{C}} = \frac{3}{2}\bar{\sigma}_{\mathrm{e}}^{\mathrm{n}}\frac{\bar{s}_{ij}}{\bar{\sigma}_{\mathrm{e}}}, \tag{4.17}$$

The governing equation for grain boundary sliding is

$$\bar{\tau} = \lambda_1 \bar{u}_s', \tag{4.18}$$

where

$$\lambda_1 = \frac{\eta_b R_I}{t_c \Sigma_0} \tag{4.19}$$

The normalized grain boundary separation is found to be

$$\bar{\delta}' = \left(\frac{\bar{V}'}{\bar{b}^2} - \frac{2\bar{V}}{\bar{b}^2} \frac{\bar{b}'}{\bar{b}} \right) \tag{4.20}$$

The rate of change for cavity spacing $\bar{b}'$ is

$$\frac{\bar{b}'}{\bar{b}} = -\frac{1}{2} \frac{\bar{N}'}{\bar{N}} \tag{4.21}$$

where $\bar{N}'$ is the normalized rate of change of cavity density and is given by

$$\bar{N}' = \frac{\bar{\sigma}_n^2 \bar{\varepsilon}_e'^C}{S_{thr}} \tag{4.22}$$

The cavity nucleation condition is

$$\bar{\sigma}_n^2 \varepsilon_e^C \geq S_{thr} \tag{4.23}$$

The normalized cavity volume growth rate is

$$\bar{V}' = \bar{V}_1' + \bar{V}_2' \tag{4.24}$$

$$\bar{V}_1' = \lambda_2 \frac{\bar{\sigma}_n}{\ln(\frac{1}{f}) - \frac{1}{2}(3-f)(1-f)}, \tag{4.25}$$

$$\lambda_2 = \frac{3Dt_c\Sigma_0}{a_0^3 h(\psi)} \tag{4.26}$$

$$f = \max\left[\omega_0^2 \left(\frac{\bar{a}}{\bar{b}} \right)^2, \left(\frac{\bar{a}}{\bar{a} + 1.5\bar{L}} \right)^2 \right], \tag{4.27}$$

$$\bar{L}=\left(\frac{h(\psi)\lambda_2}{3}\bar{\sigma}_{\mathrm{e}}^{1\text{-}\mathrm{n}}\right)^{1/3},\ \omega_0=a_0/b_0 \tag{4.28}$$

$$\bar{V}_2'=\begin{cases}\pm\dfrac{3}{2}\varepsilon_{\mathrm{e}}'^{\mathrm{C}}\bar{a}^3\left[\dfrac{3}{2n}\left|\dfrac{\sigma_{\mathrm{m}}}{\sigma_{\mathrm{e}}}\right|+\dfrac{(n-1)(n+0.4319)}{n^2}\right]^n, & \left|\dfrac{\bar{\sigma}_{\mathrm{m}}}{\bar{\sigma}_{\mathrm{e}}}\right|>1\\ \dfrac{3}{2}\varepsilon_{\mathrm{e}}'^{\mathrm{C}}\bar{a}^3\left[\dfrac{3}{2n}+\dfrac{(n-1)(n+0.4319)}{n^2}\right]^n\dfrac{\bar{\sigma}_{\mathrm{m}}}{\bar{\sigma}_{\mathrm{e}}}, & \left|\dfrac{\bar{\sigma}_{\mathrm{m}}}{\bar{\sigma}_{\mathrm{e}}}\right|\le 1\end{cases} \tag{4.29}$$

Finally, the radius of a cavity grows according to

$$\bar{a}'=\frac{V'}{3\bar{a}^2} \tag{4.30}$$

To summarize, there are seven dimensionless parameters in our problem

$$\left\{n,\bar{E},\nu,S_{\mathrm{thr}}=\frac{N_{\mathrm{I}}}{F_{\mathrm{n}}},\omega_0=\frac{a_0}{b_0},\lambda_1=\frac{\eta_{\mathrm{b}}R_{\mathrm{I}}}{\Sigma_0 t_{\mathrm{c}}},\lambda_2=\frac{3Dt_{\mathrm{c}}\Sigma_0}{a_0^3h(\psi)}\right\} \tag{4.31}$$

This normalization allows us to study the effect of different micromechanics parameters on creep behavior. Specifically, λ_1 is a ratio of the creep strain due to power law creep over the strain caused by grain boundary sliding. $\lambda_1\to 0$ corresponds to free sliding at the grain boundary, whereas $\lambda_1\to\infty$ means no grain boundary sliding is allowed. λ_2 is the ratio of cavity growth rate due to diffusion over that due to power law creep. A small λ_2 indicates that cavity growth is controlled by power law creep and a large λ_2 indicates that cavity growth is controlled by diffusion. ω_0 is the square root of the initial area fraction occupied by voids and can be considered as an initial damage parameter. Finally, S_{thr} (see(4.7)) controls the ease of cavity nucleation.

4.4 Grain Boundary Cavitation Model-Cohesive Zone Model

The grain boundary cavitation model can be interpreted as a rate dependent cohesive zone model. Note that in typical cohesive zone models, the separation is completely determined by the current state of traction. In this case, the separation

depends on the *history* of *traction*. In addition, it involves other stress components as void growth is sensitive to hydrostatic tension (see for example(4.13)). In light of these complications, we solve a simple problem to gain insight into the behavior of the CZM used in this work. For example, it is reasonable to ask whether the stress will go to zero as the interface separation becomes very large. Specifically, we subject an infinite grain boundary separated by two infinite elastic-power-law creeping grains to a constant separation rate v, that is, $\delta = vt + \delta_0$. After normalization, the imposed separation is

$$\bar{\delta} = \lambda_3 \bar{t} + 1, \quad \lambda_3 = v t_c / \delta_0. \tag{4.32}$$

To simplify the mathematics, we assume the stress state is uniaxial,

$$\sigma_e = \sigma_n = 3\sigma_m = \sigma \tag{4.33}$$

where σ is an unknown function of time. We will show that the normal traction along such a boundary goes to zero when it fails.

According to (4.20), the grain boundary separation rate is related to the cavity radius and spacing by

$$\frac{\bar{\delta}'}{\bar{\delta}} = \left(\frac{3\bar{a}'}{\bar{a}} - \frac{2\bar{b}'}{\bar{b}} \right) \tag{4.34}$$

Integrating (4.34) , we get

$$\bar{\delta} = \frac{\bar{a}^3}{\bar{b}^2} \tag{4.35}$$

Equation (4.35) shows that the separation $\bar{\delta}$ is a function only of $\bar{a}$ and $\bar{b}$ which can be viewed as *state variables*. The evolution equations of these two state variables are derived as follows.

The cavity radius growth rate $\bar{a}'$ is found by substituting (4.25)-(4.29) into (4.30),

$$\bar{a}' = \frac{\lambda_2 \bar{\sigma}}{3\bar{a}^2 q(f)} + \frac{\alpha_n \bar{a} \bar{\sigma}^n}{3} \tag{4.36}$$

$$q(f) \equiv \left[2\ln(1/f) - (3-f)(1-f)\right], \quad \alpha_n = \frac{1}{2}\left[\frac{3}{2n} + \frac{(n-1)(n+0.4319)}{n^2}\right]^n \tag{4.37}$$

Integrating (4.21), the cavity spacing b is found to relate to the cavity density by

$$\bar{b} = \bar{N}^{-1/2} \tag{4.38}$$

The cavity density $\bar{N}$ can be determined by integrating (4.22),

$$\bar{N} = 1 + \frac{H(\bar{t} - \bar{t}_N)}{S_{thr}} \int_{\bar{t}_N}^{\bar{t}} \bar{\sigma}^{n+2}(t')dt' \tag{4.39}$$

where H is the Heavside function defined by

$$H(x) = \begin{cases} 1 & x \geq 0 \\ 0 & x < 0 \end{cases} \tag{4.40}$$

and $\bar{t}_N$ is the normalized nucleation time at which the nucleation condition

$$\bar{\sigma}^2(\bar{t}_N) \int_0^{\bar{t}_N} \bar{\sigma}^n(t')dt' = S_{thr} \tag{4.41}$$

is satisfied. Combining (4.38) and (4.39),

$$\bar{b} = \left[1 + \frac{H(\bar{t} - \bar{t}_N)}{S_{thr}} \int_{\bar{t}_N}^{\bar{t}} \bar{\sigma}^{n+2}(t')dt'\right]^{-1/2} \tag{4.42}$$

Differentiating (4.42) on both sides with respect to $\bar{t}$ gives:

$$\bar{b}' = -\frac{H(\bar{t} - \bar{t}_N)}{2S_{thr}} \bar{b}^3 \bar{\sigma}^{n+2}(\bar{t}) \tag{4.43}$$

Equations (4.36) and (4.43) determine the evolution of the state variables $\bar{a}$ and $\bar{b}$. Define a damage parameter ω which is equal to the square root of the area fraction of cavities by

$$\omega = a/b = \omega_0 \bar{a}/\bar{b} \tag{4.44}$$

According to (4.36) and (4.43), $\bar{a}$ increases with time while $\bar{b}$ decreases with time. This, together with (4.44) implies that ω is a monotonic increasing function of time with range $\omega_0 < \omega \le 1$. Physically, the condition $\omega = 1$ means neighboring cavities link up to form micro-cracks and the grain boundary is fully damage at $\omega = 1$.Our goal is to study the behavior of σ and show that it goes to zero as $\omega \to 1$. To demonstrate this, we start by rewriting (4.36) as

$$3q(f)\bar{a}^2\bar{a}' = \lambda_2\bar{\sigma} + 3\alpha_n q(f)\bar{a}^3\bar{\sigma}^n \tag{4.45}$$

In the following we will show that the two terms containing *q(f)* in (4.45) go to zero as $\omega \to 1$, which would lead to zero normal traction along the grain boundary. Recall

$$f = \max\left[\omega^2, \left(\frac{\bar{a}}{\bar{a}+1.5\bar{L}}\right)^2\right],\ \bar{L} = \left(\frac{h(\psi)\lambda_2}{3}\bar{\sigma}_e^{1-n}\right)^{1/3} \tag{4.46}$$

Since $\bar{L}$ is always positive, $\bar{a}/\left(\bar{a}+1.5\bar{L}\right) < 1$ at all times, whereas our argument above shows that ω increase monotonically to 1. This means that eventually $f \to 1^-$ at $\omega = 1$. Therefore, we can write

$$f = 1 - \varepsilon \tag{4.47}$$

where ε is a small positive number. Expanding $q(f) \equiv \left[2\ln(1/f) - (3-f)(1-f)\right]$ about $\varepsilon = 0^+$ leads to

$$q(f) = -2\ln(1-\varepsilon) - (2+\varepsilon)\varepsilon = -2\left[-\varepsilon - \frac{1}{2}\varepsilon^2 - \frac{1}{3}\varepsilon^3 - ....\right] - (2\varepsilon + \varepsilon^2) = 2\sum_{k=3}^{\infty}\frac{(1-f)^k}{k} \tag{4.48}$$

Since f increases to 1 monotonically, (4.48) indicates that $q(f)$ is a monotonic decreasing function of f and it vanishes as $(1-f)^3$ as $f \to 1^-$. Therefore, as long as a' is bounded, (4.45) implies as $f \to 1^-$

$$\sigma \to 0 \tag{4.49}$$

To check if a' is bounded as $f \to 1^-$, we differentiate (4.35) with respect to time and write it in terms of $\bar{a}'$,

$$\bar{a}' = \frac{v + 2\bar{b}'\omega^3}{3\omega^2} \tag{4.50}$$

Since the denominator of (4.50) is strictly positive, $\bar{a}'$ is bounded. Thus, we have shown that the stress vanishes as $\omega \to 1$. Note that at $\omega = 1$, the interfacial displacement reaches it maximum value

$$\bar{\delta} = \bar{a}_{\max} = \bar{b}_{\min} = \left[1 + \frac{H(\bar{t} - \bar{t}_N)}{S_{thr}} \int_{\bar{t}_N}^{\bar{t}_{\max}} \bar{\sigma}^{n+2}(t')dt' \right]^{-1/2} \tag{4.51}$$

where $\bar{t}_{\max}$ is the time when $\delta = \delta_{\max}$.

Next, we show that the normal traction is a monotonic decreasing function of time. To show this, we first find the governing equation for the evolution of σ. Substituting (4.42) into (4.35), we find

$$\lambda_3 \bar{t} + 1 = \bar{\delta} = \bar{a}^3 \left(1 + \frac{H(\bar{t} - \bar{t}_N)}{S_{thr}} \int_{\bar{t}_N}^{\bar{t}} \bar{\sigma}^{n+2}(t')dt' \right) \tag{4.52}$$

Differentiate (4.52) with respect to time and rewrite it in terms of $\bar{a}'$, we find

$$\bar{a}' = \frac{\bar{a}\lambda_3 - \bar{a}^4 \bar{\sigma}^{n+2} H(\bar{t} - \bar{t}_N)/S_{thr}}{3\lambda_3 \bar{t} + 3} \tag{4.53}$$

Equating (4.53) and (4.50), after some algebra, we obtain

$$(\lambda_3 \bar{t} + 1)\alpha_n \bar{\sigma}^n + \bar{a}^3 \bar{\sigma}^{n+2} H(\bar{t} - \bar{t}_N)/S_{thr} + \frac{(\lambda_3 \bar{t} + 1)\lambda_2 \bar{\sigma}}{\bar{a}^3 q(f)} = \lambda_3 \tag{4.54}$$

In the following, we study the evolution of the stress during two stages of grain boundary cavitation.

Stage 1: before nucleation $0 < \bar{t} < \bar{t}_N$

In this period, $H(\bar{t}-\bar{t}_{\mathrm{N}})=0\Rightarrow \bar{b}'=0,\bar{b}=1$. As a result, (4.52),(4.53),(4.54) simplify to

$$\bar{a}^3=\lambda_3\bar{t}+1 \tag{4.55}$$

$$\bar{a}'=\frac{\bar{a}\lambda_3}{3\lambda_3\bar{t}+3} \tag{4.56}$$

$$A_0\bar{\sigma}^n+B_0\bar{\sigma}=C_0 \tag{4.57}$$

where

$$A_0=(\lambda_3\bar{t}+1)\alpha_{\mathrm{n}},B_0=\frac{\lambda_2}{q(f)},C_0=\lambda_3 \tag{4.58}$$

In (4.58), A_0 increases with time. Also, B_0 increases with time since *q(f)* decreases with time according to (4.48). Since C_0 is fixed, $\bar{\sigma}$ will decrease monotonically from its initial value $\bar{\sigma}_{\mathrm{ini}}=\bar{\sigma}(\bar{t}=0)$ to $\bar{\sigma}(\bar{t}=\bar{t}_{\mathrm{N}})$.

The initial stress $\bar{\sigma}_{ini}$ can be solved directly by neglecting $A_0(t=0)=\alpha_{\mathrm{n}}$ in(4.58). This approximation is justified because a simple calculation based on material parameters of ferritic and austenistic steels shows that

$$B_0(t=0)=\frac{\lambda_2}{q(f_0)}>>A_0(t=0)=\alpha_{\mathrm{n}} \tag{4.59}$$

Hence, $\bar{\sigma}_{\mathrm{ini}}$ can be approximated by

$$\bar{\sigma}_{\mathrm{ini}}\approx\frac{\lambda_3}{\lambda_2}q(f_0)=\frac{va_0^3}{3\delta_0\Sigma_0 D}q(f_0)h(\psi) \tag{4.60}$$

The nucleation time $\bar{t}_{\mathrm{N}}$ is determined by (4.41). Since $\bar{\sigma}$ decreases monotonically from its initial value (4.60), a *lower bound* for $\bar{t}_{\mathrm{N}}$ is

$$\bar{t}_{\mathrm{N}}>\bar{t}_{\mathrm{N}}^{\min}=\left(\frac{3\delta_0\Sigma_0 D}{va_0^3q(f_0)h(\psi)}\right)^{n+2} \tag{4.61}$$

From (4.61), one can see that if the separation rate *v* is very small, the time for cavity nucleation can be very long. On the other hand, if the separation rate is fast or the

grain boundary diffusivity is high, cavities can nucleate in a very short time. When $\bar{t}$ reaches $\bar{t}_{\mathrm{N}}$, we have

$$\bar{a}_N = \left(\lambda_3 \bar{t}_{\mathrm{N}} + 1\right)^{1/3} \tag{4.62}$$

$$\bar{b} = 1, \bar{N} = 1 \tag{4.63}$$

The stress at nucleation, i.e., $\bar{\sigma}\left(\bar{t} = \bar{t}_{\mathrm{N}}\right)$ can be solved from (4.57). At $\bar{t}_{\mathrm{N}}$, the normalized grain boundary opening is $\bar{\delta}_N = \lambda_3 \bar{t}_{\mathrm{N}} + 1$.

Stage 2: post nucleation $\bar{t} > \bar{t}_{\mathrm{N}}$

After $\bar{t}_N$, cavity nucleation occurs. According to (4.53), the cavity radius growth rate is given by

$$\bar{a}' = \frac{\bar{a}\lambda_3 - \bar{a}^4 \bar{\sigma}^{n+2} / S_{\mathrm{thr}}}{3\lambda_3 \bar{t} + 3} \tag{4.64}$$

Comparing (4.64) with (4.56), we see that the cavity radius growth rate is *reduced* after nucleation. What happens physically is that under constant separate rate, stress relaxation occurs faster after nucleation which leads to a slower cavity growth rate. This, together with (4.55) implies that

$$\bar{a}^3 < \lambda_3 \bar{t} + 1 \quad \text{at } \bar{t} > \bar{t}_{\mathrm{N}} \tag{4.65}$$

According to (4.43), the rate of change of cavity spacing after nucleation is

$$\bar{b}' = -\frac{\bar{b}^3 \bar{\sigma}^{n+2}(\bar{t})}{2S_{\mathrm{thr}}} \tag{4.66}$$

The normal traction after cavity nucleation can be determined using (4.54),

$$A_0 \bar{\sigma}^n + B_1 \bar{\sigma} + D_1 \bar{\sigma}^{n+2} = C_0 \tag{4.67}$$

where A_0, C_0 are defined earlier in (4.58), and

$$B_1 = \frac{(\lambda_3 \bar{t} + 1)\lambda_2}{\bar{a}^3 q(f)}, D_1 = \frac{\bar{a}^3}{S_{\text{thr}}} \tag{4.68}$$

We note the following when comparing (4.67) with (4.57):

(1) (4.65) implies that $B_1 > B_0 = \lambda_2 / q(f)$;

(2) There is an additional term $D_1 > 0$ in (4.67);

(3) A_0, C_0 are the same.

This means that $\sigma(\bar{t} \le \bar{t}_{\text{N}}) > \sigma(\bar{t} > \bar{t}_{\text{N}})$. In addition, the traction after nucleation decreases monotonically since A_0, B_1, D_1 increases with time and C_0 is a constant.

To summarize, there are two possible scenarios:

Case 1: According to (4.61), for sufficiently low normal separation velocity (reflected in λ_3) or small grain boundary diffusivity (reflected in λ_2), the nucleation time is very long. For this case, only the growth of pre-existing cavities contributes to separation. The normal traction decays monotonically to zero at a finite time $\bar{t} < \bar{t}_{\text{N}}$. For this case, the time for ω to reach 1 is typically very long. An example of this case is shown in Figure 4.2. The five dimensionless parameters used in Figure 4.2 are

$$\left\{\omega_0 = 4.2\times10^{-3}, 1/S_{\text{thr}} = 7.465\times10^{3}, \lambda_1 = 1.67\times10^{-2}, \lambda_2 = 2.037\times10^{3}, \lambda_3 = 9.037\times10^{3}\right\} \tag{4.69}$$

Case 2: For higher values of v, preexisting cavities still grow according to (4.56) at $0 < \bar{t} < \bar{t}_{\text{N}}$. After $\bar{t} = \bar{t}_{\text{N}}$, cavities grows more slowly according to (4.64) and new cavities are nucleated. Also, σ follows different evolution paths before and after nucleation, in particular the curve $\bar{\sigma}(\bar{t})$ has a jump at $\bar{t} = \bar{t}_{\text{N}}$. However, the normal traction always decreases monotonically and it vanishes when ω reaches 1. An example of this case is shown in Figure 4.3. The five dimensionless parameters used in the analysis are

$$\left\{\omega_0 = 4.2\times10^{-3}, 1/S_{\text{thr}} = 7.465\times10^{3}, \lambda_1 = 1.67\times10^{-2}, \lambda_2 = 2.037\times10^{3}, \lambda_3 = 1\times10^{5}\right\} \tag{4.70}$$

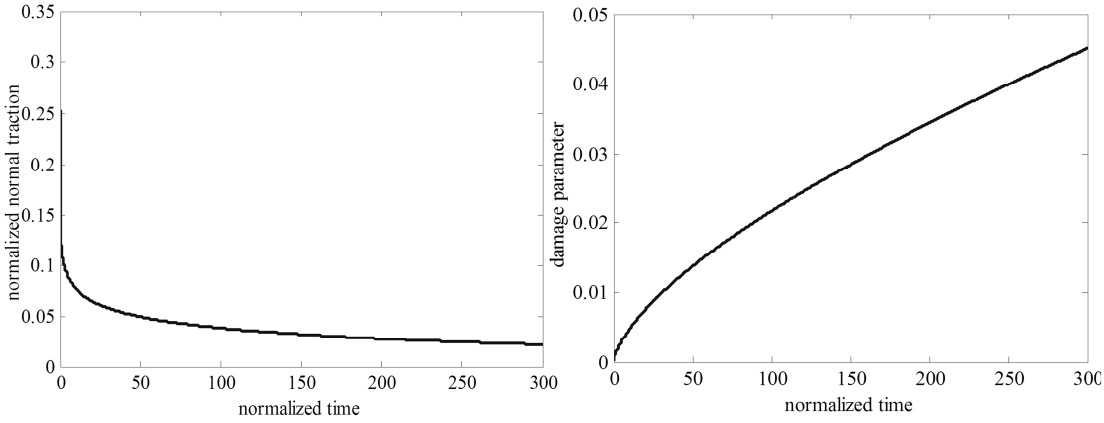

(a) (b)

Figure 4.2 Grain boundary cavitation without nucleation. (a) Normal traction versus time (b) Damage parameter versus time

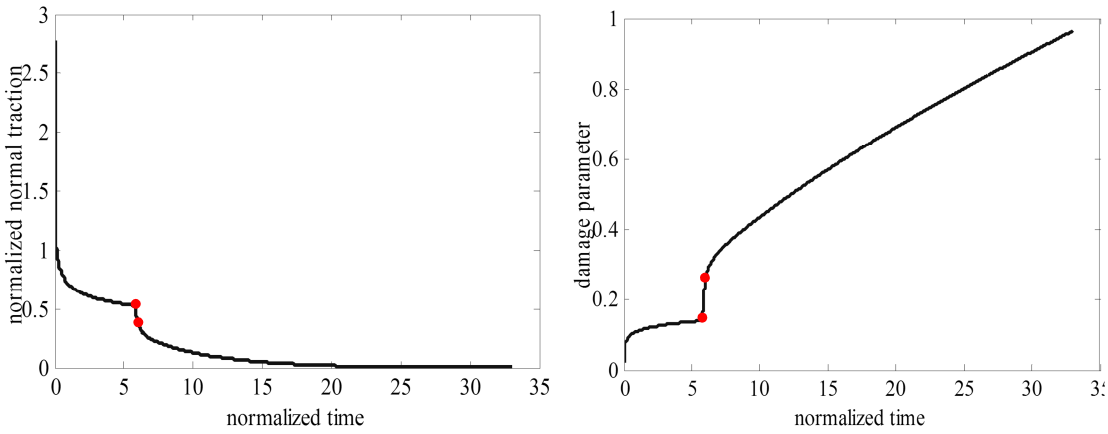

(a) (b)

Figure 4.3 Grain boundary cavitation with nucleation (a) Normal traction versus time (b) Damage parameter versus time

In summary, we have carried out a detailed analytical and numerical calculation for the special case of an infinite grain boundary separated at a constant rate and showed that stress decays to zero at a critical separation.

4.5 Finite Element Model

A typical two-dimensional (2D) microstructure and the finite element model used in this work are shown in Figure 4.4(a) and Figure 4.4(b) respectively. All calculations are performed under plane strain deformation. The 2D microstructure has 1000 random sized grains and is generated and meshed using a modified MATLAB script from Cornell Fracture Group (CFG). Grain boundary elements are generated by connecting the two grain elements on either side of a boundary. The finite element model consists of 19752 quadratic triangular grain elements and 5366 grain boundary elements. Grains are modeled as elastic-power law creeping material using ABAQUS user subroutine UMAT (ABAQUS 2008). Grain boundary separation and grain boundary sliding are modeled by cohesive zone elements based on equations (4.18)-(4.29). We have written an ABAQUS user subroutine UEL to implement these cohesive zone elements.

In this paper, F_{n} is chosen in such a way that nucleation occurs at most of the grain boundaries at the end of loading time. η is chosen based on the analytical results of Raj (1971) for steady state sliding of a grain boundary with sinusoidal shape under shear stress. Using Table 4.1, we found

$$\left\{\omega_0 = 4.2\times10^{-3}, 1/S_{\mathrm{thr}} = 6\times10^{2}, \lambda_1 = 1.67, \lambda_2 = 2.517\times10^{5}\right\} \tag{4.71}$$

We carried out two type of simulations in this work: relaxation test and uniaxial creep test (Figure 4.5(a),(b)). For the relaxation test, periodic displacement boundary condition (PBC) was used since the effective properties of a RVE are more accurately

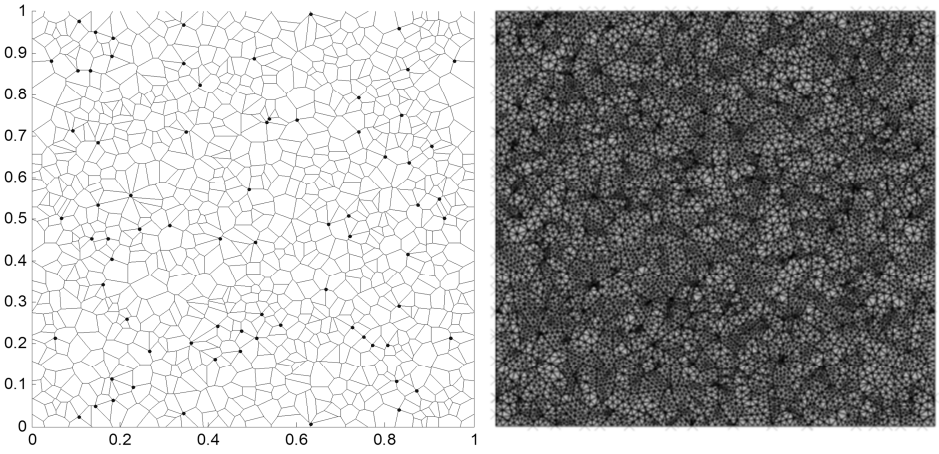

(a) (b)

Figure 4.4 (a) 2D microstructures with 1000 random sized grains. (b) 2D finite element model.

Table 4.1 Material parameters for power law creep, grain boundary sliding, grain boundary cavity nucleation and growth

Parameters	Values
Reference stress Σ_0	300 MPa
Creep Exponent n	5
Elastic power law creep coefficient B	4.115×10^{-20} $\mathrm{MPa^{-5}s^{-1}}$
Elastic Modulus E	189 GPa
Poisson's ratio ν	0.285
Grain boundary diffusivity parameter D	$7.238\times10^{-19}\,\mathrm{MPa^{-1}\cdot s^{-1}\cdot mm^{3}}$
Grain boundary viscosity η_b	$1\times10^{11}\,\mathrm{MPa\cdot s\cdot mm^{-1}}$
Initial cavity radius a_0	$3.35\times10^{-5}\,\mathrm{mm}$
Initial half cavity spacing b_0	$1.6\times10^{-2}\,\mathrm{mm}$
Grain boundary facet width $2R_I$	0.1 mm
Initial cavity density N_I	$40/\pi R_I^2$ $\mathrm{mm^{-2}}$
Nucleation activity F_n	$6\times10^{2}\,N_I$ $\mathrm{mm^{-2}}$
Characteristic time τ_c	10^7 s

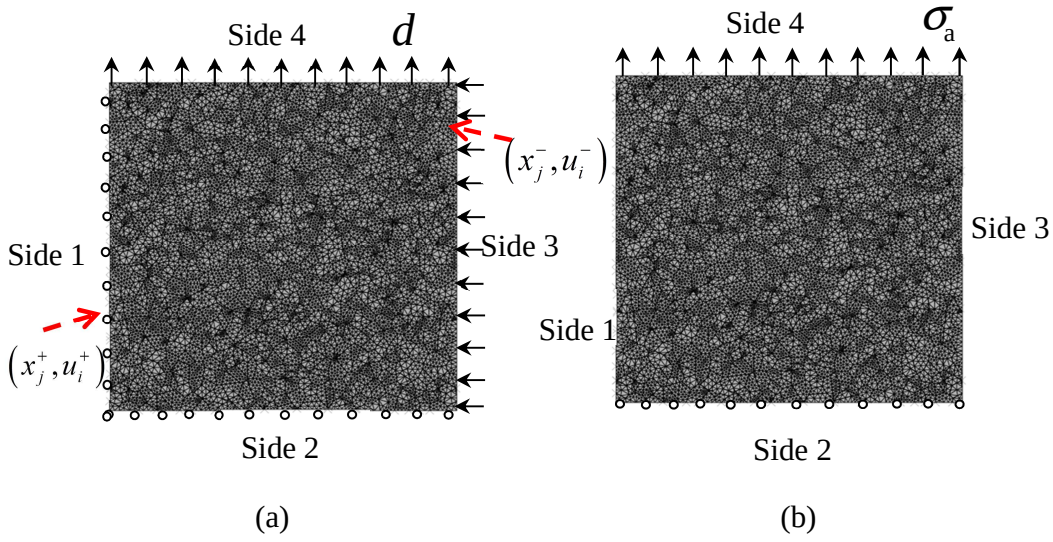

Figure 4.5 Boundary condition (a) Relaxation test (b) Uniaxial tension test

predicted compared to the case when essential or natural boundary conditions are used in homogenization analyses (Ostoja-Starzewski 2006). The PBC has the form of

$$u_i^+ - u_i^- = \varepsilon_{ij}^0 \left(x_j^+ - x_j^- \right) \tag{4.72}$$

where +, − indicates two opposite sides of the RVE. In Figure 4.5(a), side1 and side 3, side 2 and side 4 are considered two opposite sides. x_j^+, x_j^- represents the nodal coordinates at side + and - respectively, u_i^+, u_i^- are the corresponding nodal displacement vectors. ε_{ij}^0 is a constant strain tensor. To implement the periodic boundary condition in Eq (4.72). In ABAQUS, a dummy node is used where its degrees of freedom represent different components of ε_{ij}^0. In that way, the nodal displacements along the opposite sides of RVE can be coupled to the degrees of freedom of the dummy node using multiple constraints equations. The very left bottom corner node of the RVE is constrained along both the horizontal and vertical directions to avoid rigid body motion. In our simulation, relaxation test is carried out by applying $\varepsilon_{22}^0 = 0.001$, $\varepsilon_{11}^0 = -\nu\varepsilon_{22}^0 = -2.85\times10^{-4}$.

The boundary condition for the uniaxial creep test is shown in Figure 4.5(b), side 2 of the RVE is constrained in the vertical direction. Both side 1 and side 3 of the RVE are traction free, a normal surface traction $\bar{\sigma}_a = 0.1$ is applied on side 4.

The loading form for the relaxation test and uniaxial tension test is shown in Figure 4.6. The characteristic time in our simulation is $t_c = 10^7 s = 2778$ hours .We apply a total loading time $\bar{t}_{total} = 10^{-2}$ which corresponds to a time of 27.78 hours.

4.6 Results and Analysis of Relaxation Test

We present simulation results for relaxation test in this section. Recall the coupling between grain boundary sliding, grain boundary diffusion and power law creep are controlled by the dimensionless parameter λ_1 and λ_2 respectively, therefore, we can

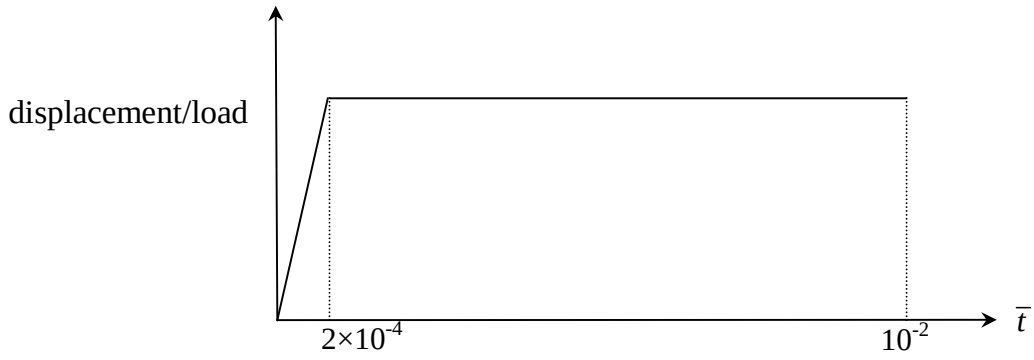

Figure 4.6 Loading history of the relaxation/creep test

study the effect of these mechanisms on the creep behavior by varying λ_1 and λ_2 while fixing the rest of the parameters, i.e., $\omega_0 = 4.2\times10^{-3}, 1/S_{\text{thr}} = 6\times10^{2}$. The parameters λ_1 and λ_2 used in our simulations are summarized in Table 4.2. In all three cases, the values of λ_2 are chosen so that cavity growth is controlled mainly by diffusion rather than by power law creep. Case 3 has the slowest cavity growth rate among the three cases.

Stress (σ_{22}) relaxation curves for all three cases are presented in Figure 4.7. We also plot the stress relaxation curve where grains deform by elastic power law creep only and grain boundary sliding and cavitation are not allowed. As shown in Figure 4.7, these damage mechanisms reduce the average stress and caused much faster stress relaxation. The average normal stress and hence the deformation inside a typical grain goes down as most of the imposed strain is accommodated by the opening and sliding of the grains. Contour plots of vertical displacement fields (u_2) of the RVE at time $\bar{t} = 10^{-2}$ are shown in Figure 4.8 for these cases. The deformation is magnified by 200 times and the range of the u_2 contour plot is $[-2.46\times10^{-6}, 1\times10^{-3}]$. The following features of the deformed RVE are observed:

(1) The grain boundary facets perpendicular to vertical displacement direction have more pronounced separations for all three cases. This is due to the higher normal stress on the grain boundary facets perpendicular to vertical displacement direction compared to other inclined grain boundaries.

(2) Case 2 shows much more pronounced cavity growth along horizontal boundary facets than case 1 and case 3. This result is expected for case 3 since diffusion is slower in this case. However, it seems counterintuitive that case 1 has less pronounced cavity growth than case 2, which indicates for the same grain boundary diffusivity, grain boundary cavities grow faster in a RVE with sliding resistant grain boundaries. The explanations for this result are:

Table 4.2 Varying dimensionless parameters for creep rupture simulations

Case	λ_1	λ_2
Case 1	1.67	2.517×10^5
Case 2	16.7	2.517×10^5
Case 3	16.7	2.517×10^4

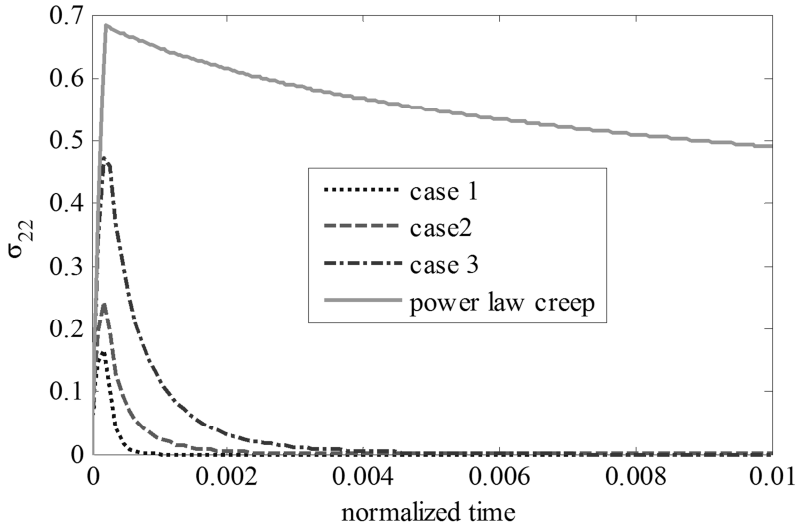

Figure 4.7 Normalized stress $\bar{\sigma}_{22}$ versus time for relaxation test. The solid line is for a pure elastic power law creeping material. Dash lines are for the three cases listed in Table 4.2.

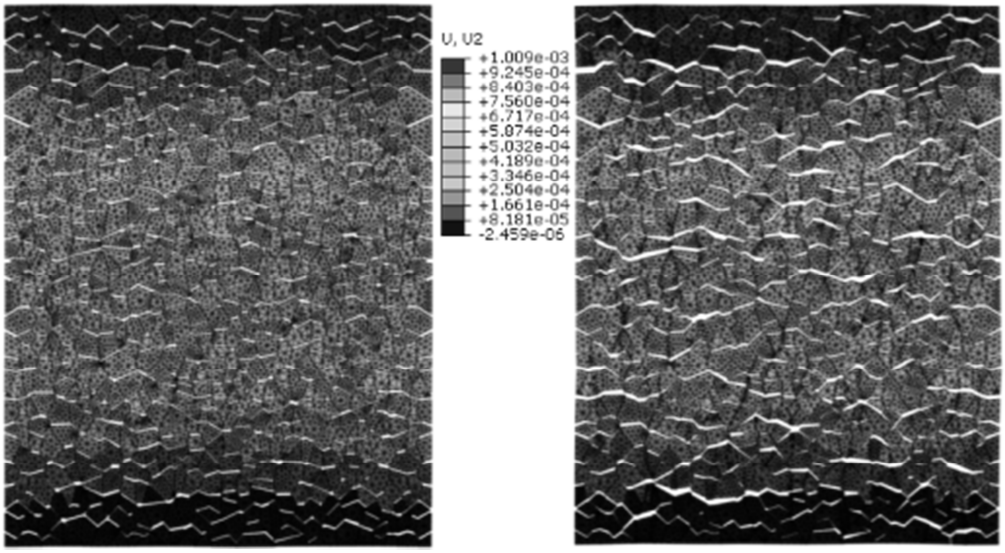

(a) Case 1 (b) Case 2

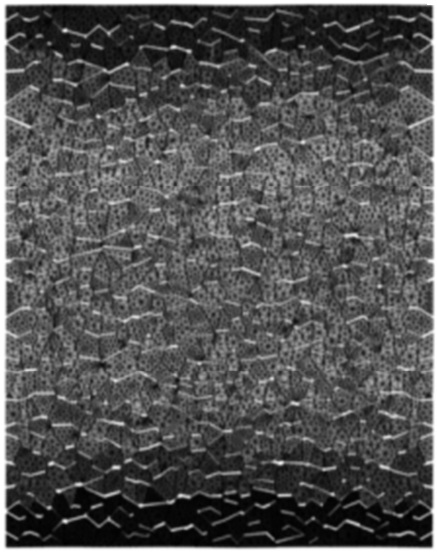

(c) Case 3

Figure 4.8 Vertical displacement (u_2) contour plot for the three cases listed in Table 4.2.

(1) The prescribed displacement boundary condition in the vertical direction and the randomness of the grain geometry tend to favor grain boundary separation on the horizontal facets.

(2) The boundary condition $\varepsilon_{11}^{0} < 0$ tends to force inclined grain boundary facets to slide. Assuming that approximately the same amount of sliding is needed to accommodate the applied strain, a higher shear stress $\bar{\tau}$ will be induced along these inclined grain boundaries in case 2. According to Riedel and others (Riedel 1987; Davies and Dutton 1966; Davies and Williams 1969), the shear stress along the inclined boundaries can enhance the cavity growth rate along the horizontal facets under transverse compression and the cavity growth rate is found to be proportional to $\bar{\tau}$. This argument suggested that higher $\bar{\tau}$ along inclined boundaries in case 2 leads to more grain boundary separation along horizontal facets. Finally, we note that similar results were obtained by Du et al (2010) in their simulations with constant strain rate applied.

For a RVE with multiple grain boundaries, it can be shown that the overall strain of the RVE, $\varepsilon_{ij}^{\mathrm{RVE}}$, is given by (see details in Appendix 4.1)

$$\varepsilon_{ij}^{\mathrm{RVE}} = \bar{\varepsilon}_{ij} + \varepsilon_{ij}^{\mathrm{gb}} \tag{4.73}$$

where $\bar{\varepsilon}_{ij}$ the average strain within the continuous bulk grains, $\varepsilon_{ij}^{\mathrm{gb}}$ is the average strain due to grain boundary separation and sliding,

$$\varepsilon_{ij}^{\mathrm{gb}} \equiv \frac{1}{2A}\sum_{k}\int_{S^k}\left(\left[u_i\right]n_j + \left[u_j\right]n_i\right)ds \tag{4.74}$$

where k is the number of grain boundaries with displacement discontinuity, $\left[u_i\right] = u_i^{+} - u_i^{-}, i = 1,2$ is the displacement jump across the grain boundary S^k, n_j^{-}, n_j^{+} are the unit normal vectors on each side of a grain boundary (see Figure 4.9) and A is the area of the 2D representative volume element. Equation (4.74) states that the overall strain of RVE has two contributions: grain deformation and grain boundary

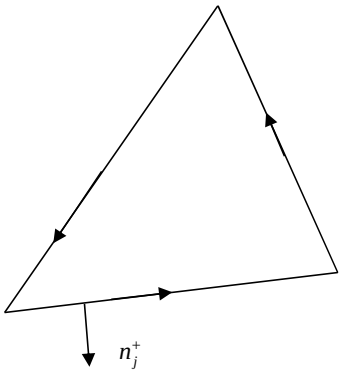

Figure 4.9 Definition of positive orientation of the boundary of a triangular grain (counterclockwise), the orientation of the unit normal vector to a boundary (only one indicated in figure) is defined by the right hand rule

sliding and separation. Thus, for a given macroscopic strain ε_{ij}^{0} , (4.74) predicts that the averages strain within the grains $\overline{\varepsilon}_{ij}$ can be significantly reduced by the sliding and separation of grain boundaries. Our finite element results verified that the grain deformation contribution to the overall ε_{22} is very small, less than 10^{-5} (about 1% of ε_{22}^{0}) for all three cases. This indicates that the major contribution to the strain comes from grain boundary displacement discontinuity due to cavity nucleation and grain boundary sliding.

4.7 Results and Analysis of Uniaxial Creep Test

In this section, uniaxial creep test results are presented for the three cases in Table 4.2. A normalized applied tensile stress $\overline{\sigma}_{\mathrm{a}} = 0.1$ along the loading axis is used for all cases (see Figure 4.5(b)). Finite element results show that case 1 has the maximum vertical displacement (u_2), indicating that grain boundary sliding and cavitation play a major role in the overall deformation of the RVE. This can be quantified by plotting the inelastic strain ($\varepsilon_{22}^{\mathrm{I}}$) versus time as shown in Figure 4.10. As a comparison, we also plot the inelastic strain of a pure elastic power law creeping material in the absence of grain boundary sliding and cavitation. It has been known for a long time that grain boundary sliding enhances creep deformation at low stresses. For example, Ghahremani (1980) simulated the tensile response of a regular array of two dimensional hexagonal power-law creeping grains with sliding grain boundaries and showed that the overall strain rate, in uniaxial plane strain deformation, is given by

$$\dot{\varepsilon} = B\left(f\sigma\right)^{n} \tag{4.75}$$

where *f* is a stress-enhancement factor. In general, *f* is a function of the applied stress σ and power law creep exponent *n*. For sufficiently low stresses (i.e., $\lambda_1 < 1$ in our notation) and freely sliding grains, Gharemani (1980) showed that f is approximately

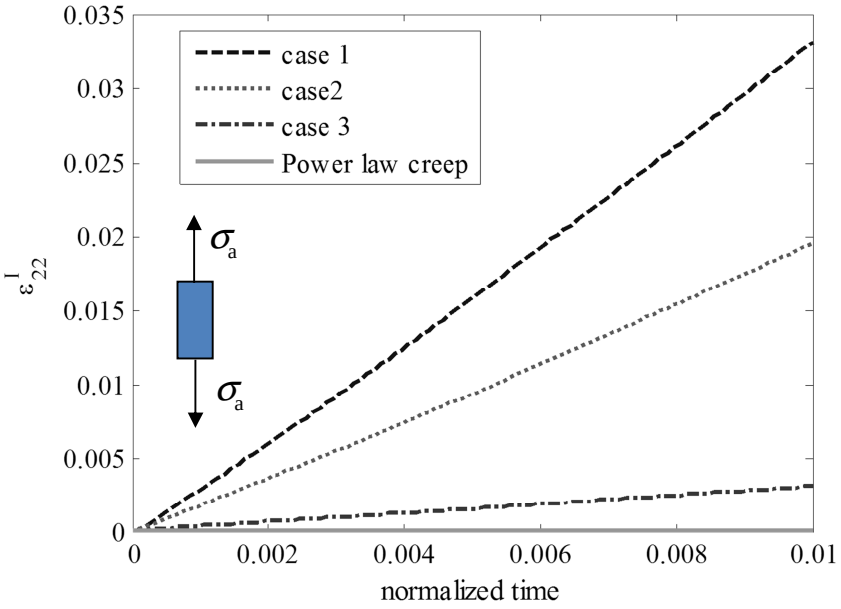

Figure 4.10 Inelastic strain ε_{22}^{I} versus time for uniaxial tension test. The solid line is for a pure elastic power law creeping material. Dash lines are the results for the three cases listed in Table 4.2.

independent of σ with values ranging from 1.16 to 1.19 for *n =1* to 4 . A summary of the reported values of f based on different models can be found in Beere (1982)'s paper and the references within. Gharemani's analysis did not account for cavity growth. Cavity growth by diffusion was included in the analysis of Anderson and Rice (1985), who numerically studied the coupling of cavity growth with free sliding grain boundaries using a 3D periodic polycrystalline model where the grains deform by power law creep and all the grain boundary facets oriented approximately normal to the applied tension load are uniformly cavitated. As noted out by Riedel (1987), cavity growth enhances the creep rate by an additional factor of 3.34×3.1^{n} . It is difficult to compare our results with Anderson and Rice's since they used a 3D model with regular size grains and assumes that grain boundary cavitation occurs at the grain boundary facets with certain orientation. In our case, we use a 2D random grain model and the presence and growth of cavities on a grain boundary facet depends on the nucleation condition. The overall enhancement factor in case 1, 2 and 3 are found to be $213,126,21$ respectively. Note that this enhancement factor depends on the parameters $\omega_0, S_{\text{thr}}, \lambda_1, \lambda_2$ as well as the applied stress.

Figure 4.10 shows that the inelastic strain increases linearly with time, however, the slopes of the inelastic strain versus time are different, indicating that creep strain rate is enhanced by damage due to cavitation and sliding. Figure 4.10 does not show tertiary creep behavior due to the relatively short time used in our calculation which corresponds to an actual time of 28 hours. Tertiary creep like behavior is noticeable if our calculations are carried out using high grain boundary diffusivity and low grain boundary viscosity. Plots of inelastic strain versus normalized time for two cases are shown in Figure 4.11. As shown in this figure, the creep strain starts to increase very rapidly soon after loading and tertiary creep like behavior takes over at $\bar{t} = 10^{-4}$.

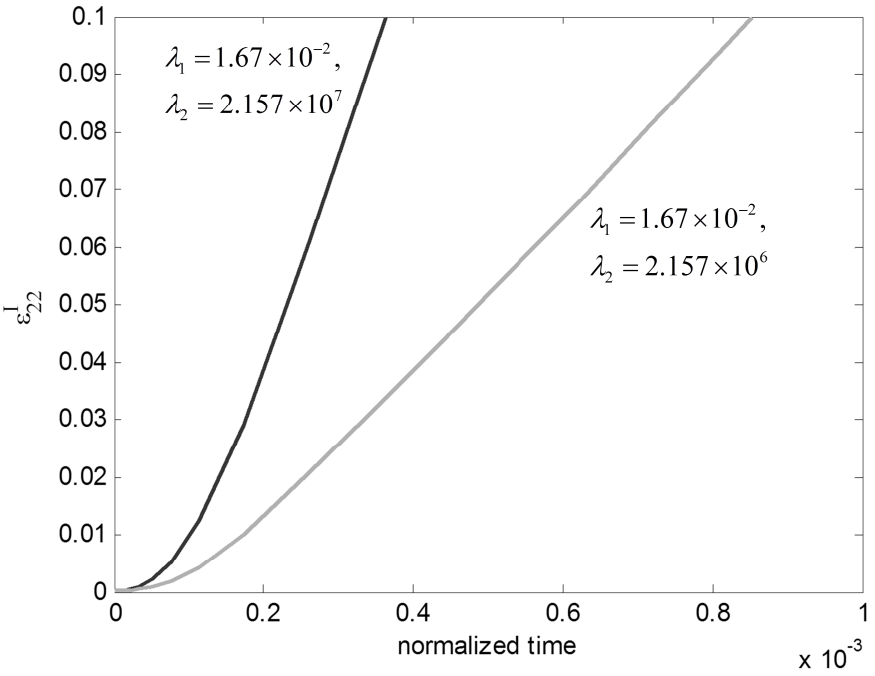

Figure 4.11 Inelastic strain $\varepsilon_{22}^{\mathrm{I}}$ versus time for two cases with high grain boundary diffusivity and low viscosity.

It is interesting to plot the separation $\bar{\delta}$ versus traction $\bar{\sigma}_n$ of a typical grain boundary in our simulations. These results for the grain boundary element 24531 are shown in Figure 4.12 for all three cases. The peak stress $\bar{\sigma}_n^{peak}$ occurs when the cavity nucleation is satisfied ($\bar{\sigma}_n^2 \varepsilon_e^C \geq S_{thr}$). Finite element results show the effective creep strain (ε_e^C) in neighboring grain elements of grain boundary element 24531 is the highest in case 2, lowest in case 3. This leads to the lowest $\bar{\sigma}_n^{peak}$ in case 2. For the same simulation time, the work done by the normal traction is highest in case 1 and lowest in case 3, although the peak normal traction for case 1 and 3 are quite similar. Figure 4.12 shows more grain boundary separation occurs in case 1 than in case 2. This is to be expected, since sliding of the grain boundary relaxes the geometry constraints at grain junctions, allowing for the grain boundaries that are normal to the loading axis to separate in a uniform manner. On the other hand, our results in Figure 4.13, which plot the evolution of the damage parameter $\omega = a/b$, show that cavity growth by diffusion plays a significant role in determining the total amount of grain boundary separation.

4.8 Summary and Discussion

A numerical model based on finite element method is developed to study the damage evolution of a two dimensional array of random grains loaded in plane strain. The grains deform by elastic power law creep and the grain boundaries can slide and separate. The separation for a grain boundary facet is determined by cavity nucleation and growth which is controlled by grain boundary diffusion and power law creep. Grain boundary sliding is decoupled from grain boundary separation and both are incorporated into a time dependent cohesive zone model.

If an infinite grain boundary is separated at a constant rate, we show analytically that the normal traction will vanish when the damage parameter approaches 1. To study creep in more realistic structure, we implemented this CZM in a commercial

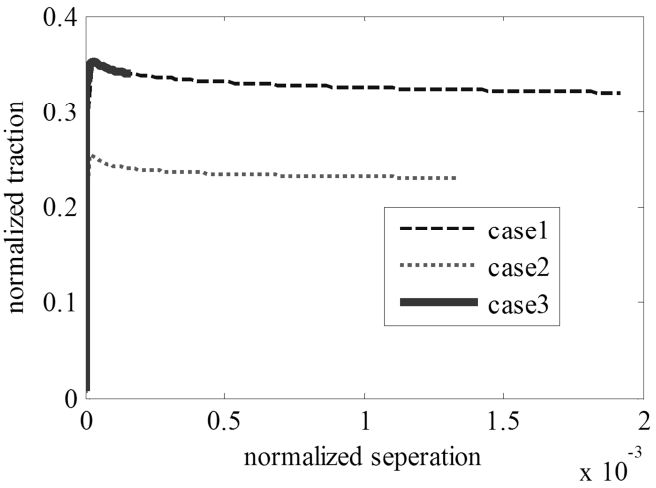

Figure 4.12 Normal traction versus separation curve for grain boundary element 24531. Results are obtained based on uniaxial tension test for the three cases listed in Table 4.2.

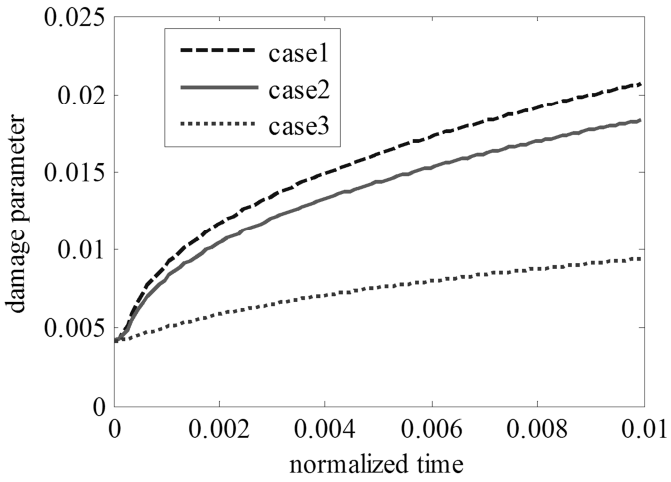

Figure 4.13 Damage parameter versus time for grain boundary element 24531. Results are obtained based on uniaxial tension test for the three cases listed in Table 4.2.

finite element program ABAQUS using a user defined subroutine. We used this method to simulate stress relaxation and creep of a RVE subjected to uniaxial deformation. These calculations depend on four dimensionless parameters, S_{thr}, ω_0, λ_1, and λ_2. In all simulations, S_{thr} and ω_0 are fixed. The results of the relaxation test show that most of the imposed strain is accommodated by the separation and sliding of the grain boundaries. Thus, these creep damage mechanisms cause faster stress relaxation than power law creep. We also found that in a relaxation test, more grain boundary separation occurs in a RVE with sliding resistant grain boundaries than in a RVE with more freely sliding grain boundaries. For the case of uniaxial creep test, the overall strain rate of a microstructure is enhanced by grain boundary cavitation and grain boundary sliding significantly.

There are obvious limitations in our analysis. For example, identical material properties are assigned to all grains and crystallographic orientation dependence of creep deformation is not investigated. As pointed out by Westwood et al (2004), the cavity model used in this work tends to overestimate the damage caused by cavity diffusion. The grain boundary sliding model used in this chapter is based on a result of Raj (1971) where there are very limited experimental data. However, we are not aware of other theories on grain boundary sliding that can be readily used for computation modeling. The weakest link in our model is the criterion for void nucleation. There is no consensus on this subject, so we used a model that is purely phenomological.

Appendix 4.1 Derivation of Equation (4.73)

For a RVE with grains and grain boundaries, we define the overall strain of the RVE as

$$\varepsilon_{ij}^{\mathrm{RVE}} \equiv \frac{1}{2A}\int_S \left(u_i n_j + u_j n_i\right) ds \tag{4.76}$$

where S is the external boundary of the RVE, A is the area of the RVE, u_i is the displacement, n_j is the outward normal.

By definition, the average strain within grains in the RVE is,

$$\bar{\varepsilon}_{ij} = \frac{1}{A}\sum_{i=1}^{N}\int_{D_i}\varepsilon_{ij}dA \tag{4.77}$$

where D_i represents the region occupied by the i^{th} grain, ε_{ij} is the microscopic strain field and N is the total number of grains in the RVE. ε_{ij} is continuous within each grain, apply divergence theorem on (4.77), we get

$$\int_{D_i}\varepsilon_{ij}dA = \frac{1}{2}\int_{S_i}\left(u_i n_j + u_j n_i\right)ds \tag{4.78}$$

where S_i are oriented boundaries (by convention, we assume all closed paths are positively oriented so that the direction of the path is counterclockwise. This orientation defines the direction of the unit normal vector associated with the path, which follows the right hand rule (see Figure 4.9).

Equations (4.77) and (4.78) imply that

$$\bar{\varepsilon}_{ij} = \frac{1}{2A}\sum_{i=1}^{m}\int_{S_i}\left(u_i n_j + u_j n_i\right)ds \tag{4.79}$$

In (4.79) , S_i consists of both the external and internal boundaries. m is the total number of boundaries in the RVE. According to (4.76), the sum of the external boundaries is represented by S, we rewrite (4.79) as

$$\bar{\varepsilon}_{ij} = \frac{1}{2A}\int_{S}\left(u_i n_j + u_j n_i\right)ds + \frac{1}{2A}\sum_{k}\int_{S_k^I}\left(u_i n_j + u_j n_i\right)ds \tag{4.80}$$

where S_k^I in the second integral in (4.80) denotes an internal boundary k. Define the interface displacement discontinuity as

$$\left[u_i\right] = u_i^+ - u_i^-, \quad i = 1,2 \tag{4.81}$$

Using this notation, (4.80) can be rewritten as

$$\bar{\varepsilon}_{ij} = \varepsilon_{ij}^{\mathrm{RVE}} + \frac{1}{2A}\sum_{k}\int_{S_I^k}\left([u_i]n_j + \left[u_j\right]n_i\right)ds \tag{4.82}$$

where $n_j \equiv n_j^+$. The quantity inside the square bracket is evaluated on the k^{th} internal boundary or interface. Let us denote second term in (4.82) as ε_{ij}^{gb} and it is the strain caused by grain boundary discontinuities, i.e.,

$$\varepsilon_{ij}^{gb} \equiv -\frac{1}{2A}\sum_{k}\int_{S_I^k}\left([u_i]n_j + \left[u_j\right]n_i\right)ds \tag{4.83}$$

Equation (4.82) can be written as

$$\varepsilon_{ij}^{\mathrm{RVE}} = \bar{\varepsilon}_{ij} + \varepsilon_{ij}^{\mathrm{gb}} \tag{4.84}$$

Thus, the overall strain of the RVE $\varepsilon_{ij}^{\mathrm{RVE}}$, consists of two parts: the average strain within the grains and the strain caused by discontinuities on the internal boundaries such as grain boundary sliding and separation.

REFERENCES

ABAQUS (2008) version 6.8-3. Dassault Systemes SIMULIA Corp.

Anderson P, Rice J (1985) Constrained creep cavitation of grain boundary facets. Acta Metall 33:409-422

Ashby M, Gandhi C, Taplin D (1979) Overview No. 3 Fracture-mechanism maps and their construction for fcc metals and alloys. Acta Metall 27:699-729

Beere W (1982) Stress redistribution due to grain-boundary sliding during creep. Met Sci 16:223-228

Bower AF, Wininger E (2004) A two-dimensional finite element method for simulating the constitutive response and microstructure of polycrystals during high temperature plastic deformation. J Mech Phys Solids 52:1289-1317

Budiansky B, Hutchinson J, Slutsky S (1982) Void growth and collapse in viscous solids. Mech Solids:13-45

CFG http://www.cfg.cornell.edu/.

Chen IW, Argon A (1981) Diffusive growth of grain-boundary cavities. Acta Metall 29:1759-1768

Chuang TJ, Kagawa KI, Rice JR, Sills LB (1979) Overview no. 2: non-equilibrium models for diffusive cavitation of grain interfaces. Acta Metall 27:265-284

Davies P, Dutton R (1966) Cavity growth mechanisms during creep. Acta Met 14:1138-1140

Davies P, Williams K (1969) Cavity Growth by Grain-Boundary Sliding during Creep of Copper. Met Sci 3:220-221

Du N, Bower AF, Krajewski PE (2010) Numerical simulations of void growth in aluminum alloy AA5083 during elevated temperature deformation. Mater Sci Eng: A 527:4837-4846

Dyson B (1976) Constraints on diffusional cavity growth rates. Met Sci 10:349-353

Evans H (1971) The growth of creep cavities by grain boundary sliding. Philos Mag 23:1101-1112

Fields R, Weerasooriya T, Ashby M (1980) Fracture-mechanisms in pure iron, two austenitic steels, and one ferritic steel. Metall Mater Trans A 11:333-347

Gandhi C, Ashby M (1979) Overview no. 5: Fracture-mechanism maps for materials which cleave: FCC, BCC and HCP metals and ceramics. Acta Metall 27:1565-1602

Ghahremani F (1980) Effect of grain boundary sliding on steady creep of polycrystals. Int J Solids Struct 16:847-862

Van der Giessen E, Tvergaard V (1991) A creep rupture model accounting for cavitation at sliding grain boundaries. Int J Fracture 48:153-178

Hancock J (1976) Creep cavitation without a vacancy flux. Met Sci 10:319-325

Hull D, Rimmer D (1959) The growth of grain-boundary voids under stress. Philos Mag 4:673-687

Iesulauro E, Ingraffea AR, Arwade S, Wawrzynek PA. Simulation of Grain Boundary Decohesion and Crack Initiation in Aluminum Microstructure Models. Fatigue and Fracture Mechanics: 33rd Volume, In ASTM STP 1417, W.G. Reuter and R.S. Piascik, Eds., American Society for Testing and Materials, West Conshohocken, PA, 715-728, 2002.

Kanit T, Forest S, Galliet I, Mounoury V, Jeulin D (2003) Determination of the size of the representative volume element for random composites: statistical and numerical approach. Int J Solids Struct 40:3647-3679

Larson F, Miller J (1952) A time-temperature relationship for rupture and creep stresses. Trans ASME 74:765-775

Larsson F, Runesson K, Saroukhani S, Vafadari R (2011) Computational homogenization based on a weak format of micro-periodicity for RVE-problems. Comput Meth Appl Mech Eng 200:11-26

Needleman A, Rice J (1980) Plastic creep flow effects in the diffusive cavitation of grain boundaries. Acta Metall 28:1315-1332

Onck P, Van der Giessen E (1998) Growth of an initially sharp crack by grain boundary cavitation. J Mech Phys Solids 47:99-139

Onck P, Van der Giessen E (1997) Microstructurally-based modelling of intergranular creep fracture using grain elements. Mech Mater 26:109-126

Ostoja-Starzewski M (2006) Material spatial randomness: From statistical to representative volume element. Probab Eng Mech 21:112-132

Raj R, Ashby M (1971) On grain boundary sliding and diffusional creep. Metall Mater Trans B 2:1113-1127

Riedel H (1984) Cavity nucleation at particles on sliding grain boundaries. A shear crack model for grain boundary sliding in creeping polycrystals. Acta Metall 32:313-321

Riedel H (1987) Fracture at high temperatures. Springer-Verlag,

Sham TL, Needleman A (1983) Effects of triaxial stressing on creep cavitation of grain boundaries. Acta Metall 31:919-926

Terada K, Hori M, Kyoya T, Kikuchi N (2000) Simulation of the multi-scale convergence in computational homogenization approaches. Int J Solids Struct 37:2285-2311

Van der Giessen E, Tvergaard V (1994) Development of final creep failure in polycrystalline aggregates. Acta Metall Mater 42:959-973

Westwood C, Pan J, Crocombe A (2004) Nucleation, growth and coalescence of multiple cavities at a grain-boundary. Eur J Mech A/Solid 23:579-597

Wray P (1969) Strain - Rate Dependence of the Tensile Failure of a Polycrystalline Material at Elevated Temperatures. J Appl Phys 40:4018-4029

CHAPTER 5

PLANAR DEFORMATION OF RANDOM SIZED POWER LAW CREEPING GRAINS WITH SLIDING AND CAVITATING GRAIN BOUNDARIES

PART II: INTERFACE EMBRITTLEMENT

5.1 Introduction

Most high temperature materials contain nonmetallic impurities such as oxygen and hydrogen which are insoluble to the host material. Such impurities can segregate to grain boundaries which would affect the creep rupture properties of these materials or further lead to intergranular brittle fracture (Eberhart et al. 1985; McMahon and Marchut 1978; Edwards et al. 1976; Woodford 1981; Woodford and Bricknell 1981). For example, Helium is precipitated into small bubbles at grain boundaries of stainless steel and cause severe loss of ductility (Riedel 1987). Oxygen can cause grain boundary embrittlement in Nickel and some nickel-based super alloys at temperatures above 1000^0C (Bricknell and Woodford 1982; Pandey et al. 1984).

Several micromechanical based theories have been proposed to study the exact cause for grain boundary embrittlement due to the presence of impurities; however currently no consensus has been reached. For example, Troiano (1960) proposed that impurities form bonds with the host material along grain boundaries which are weaker than the host-host bonds and grain boundary decohesion is more likely to occur at these newly formed bonds. Messmer and Briant's (1982) calculation on cluster of four metal atoms surrounding one interstitial impurity show that the impurity along grain boundaries weakens the nearby host-host bonds and therefore fracture occurs at the bulk materials close to the grain boundary. Goodwin et al. (1988) carried out quantum-mechanical calculations of the fracture energy of Al[111] surface with and without

impurities. Their results do not support the decohesion models of impurity-promoted grain boundary embrittlement since the presence of Ge and As impurities are found to enhance the interlayer cohesion of Al[111]. Another class of theories is based on the thermodynamic and kinetics aspects of interface decohesion due to embrittling impurities. Rice (1976) and Hirth and Rice (1980) studied the thermodynamic process of impurity segregation into a grain boundary and reducing its cohesion in detail for the limiting case of slow and fast interface separation. Mishin et al. (2002) extended the work to a more general case which is applicable to any separation rate. Most of the thermodynamic-based interface embrittlement analysis relates grain boundary cohesion with the impurity concentration. However, the stress-driven diffusion of the impurities along the grain boundary is not incorporated.

The absence of a well-established mechanical model for interface embrittlement makes it difficult to study the creep damage in high temperature materials due to grain boundary cavitation and impurity embrittlement. Hence there is little literature on this subject. Deng et al. (2005) established a combined creep and oxygen embrittlement model in which the rate of damage growth consists of two components, one due to creep deformation and one due to accelerated cavity nucleation caused by oxygen embrittlement which occurs when the first principal stress of the applied stress state exceeds a threshold. However, only one dimensional analysis is carried out in their work to quantify the damage evolution in the creep test and no full-field solution for creep response of 2D or 3D microstructure and the interaction between cavitation and embrittlement is studied.

In this chapter, we propose a unified model where creep damage caused by grain boundary separation due to grain boundary cavitation and interface embrittlement is incorporated in an additive way. The cohesive zone model in Chapter 4 is extended to account for grain boundary embrittlement. Specifically, we assume a critical stress in

which embrittlement can occur and a work of cohesion which is required to fail a unit area of grain boundary facet without cavities. We study the interaction of interface embrittlement and grain boundary cavitation and their effect on the overall creep behavior of the material.

The outline of this chapter is as follows. In section 5.2 we briefly review the cohesive zone model where cavity nucleation and growth leads to grain boundary separation. A unified model allowing for boundary decohesion due to embrittlement is proposed in section 5.3. Details of finite element analysis based on the extended cohesive zone model and numerical results are presented in section 5.4 and section 5.5 respectively. Finally, summary and discussion are given in section 5.6.

5.2 Brief review

In a previous chapter, we studied the opening of a grain boundary due to nucleation and growth of creep cavities using the model summarized by Onck and Van der Giessen(1998). Briefly, they proposed that a grain boundary facet can nucleate cavities if the condition

$$S = \left(\frac{\sigma_n}{\Sigma_0} \right)^2 \varepsilon_{\mathrm{e}}^{\mathrm{C}} > S_{\mathrm{thr}} \equiv \frac{N_{\mathrm{I}}}{F_{\mathrm{n}}} \tag{5.1}$$

is satisfied. Here ε_e^C is the effective creep strain, N_I is the initial cavity density upon nucleation, σ_{n} is the normal stress along the grain boundary, Σ_0 is a stress normalization factor, F_{n} is a material parameter which indicates the nucleation activity, it has the same unit as N_I. As long as there are voids on the boundary (e.g. pre-existing cavities in Figure 4.1), the separation is denoted by $\delta = V / \pi b^2$ and the rate of separation $\dot{\delta}$ rate of a material point on the boundary is approximated by smearing out the cavities,

$$\dot{\delta} = \frac{\dot{V}}{\pi b^2} - \frac{2V}{\pi b^2}\frac{\dot{b}}{b} \tag{5.2}$$

where $2b$ denotes the average spacing between two adjacent cavities, a is the cavity radius, 2ψ is the dihedral angle of the cavity, $V = \frac{4}{3}\pi a^3 h(\psi)$ denotes the volume of a cavity with

$$h(\psi) = (\frac{1}{1+\cos\psi} - \frac{1}{2}\cos\psi)\frac{1}{\sin\psi} \tag{5.3}$$

Recall that the separation $\delta = V/\pi b^2$ can be written as a function of a and b only.

The second term in (5.2) vanishes if (5.1) is not satisfied, otherwise

$$\frac{\dot{b}}{b} = -\frac{1}{2}\frac{\dot{N}}{N} \tag{5.4}$$

where

$$\dot{N} = F_{\mathrm{n}}\left(\frac{\sigma_{\mathrm{n}}}{\Sigma_0}\right)^2 \dot{\varepsilon}_{\mathrm{e}}^{\mathrm{C}} \tag{5.5}$$

where $\dot{\varepsilon}_e^C$ is the effective creep strain rate defined by the power law creep (Equation (4.3)). The cavity growth rate $\dot{V}$ in (5.2) consists of a contribution from vacancy diffusion and from deformation due to power law creep (Budiansky et al. 1982; Sham and Needleman 1983; Dyson 1976; Needleman and Rice 1980; Tvergaard 1984), i.e.,

$$\dot{V} = \dot{V}_1 + \dot{V}_2 \tag{5.6}$$

where

$$\dot{V}_1 = 4\pi D\left[\frac{\sigma_{\mathrm{n}} - (1-f)\sigma_{\mathrm{s}}}{q(f)}\right], q(f) = 2\ln(1/f) - (3-f)(1-f) \tag{5.7}$$

$$f = \max\left[\left(\frac{a}{b}\right)^2, \left(\frac{a}{a+1.5L}\right)^2\right],\ L = \left(D\sigma_{\mathrm{e}}/\dot{\varepsilon}_{\mathrm{e}}^{\mathrm{C}}\right)^{1/3} \tag{5.8}$$

$$\dot{V}_2 = \begin{cases} 2\pi a^3 \dot{\varepsilon}_e^C h(\psi) \left[\frac{3}{2n} \left| \frac{\sigma_m}{\sigma_e} \right| + \frac{(n-1)(n+0.4319)}{n^2} \right]^n & \left| \frac{\sigma_m}{\sigma_e} \right| > 1 \\ 2\pi a^3 \dot{\varepsilon}_e^C h(\psi) \left[\frac{3}{2n} + \frac{(n-1)(n+0.4319)}{n^2} \right] \frac{\sigma_m}{\sigma_e} & \left| \frac{\sigma_m}{\sigma_e} \right| \le 1 \end{cases} \tag{5.9}$$

where D is the grain boundary diffusivity, σ_s is the sintering stress which is usually small and it is neglected in our analysis, n is the creep exponent in the elastic power law formulation, L is the diffusive length which defines the interaction of power law creep and grain boundary diffusion, σ_e, σ_m are the effective stress and mean stress respectively. All variables such as effective stress, mean stress, creep strain and creep strain rate are evaluated at distances far from the cavities but still close to the grain boundary.

Linear grain boundary sliding model where relative grain boundary sliding rate $\dot{u}_s$ is directly proportional to the shear stress τ along the grain boundary is used (Raj and Ashby 1975) i.e.,

$$\dot{u}_s = \frac{\tau}{\eta_b} \tag{5.10}$$

where η_b is the grain boundary viscosity.

5.3 A Unified Model Allowing for Boundary Decohesion

The grain boundary cavitation model in (5.1)-(5.9) can be interpreted as a rate dependent cohesive zone model. The separation of a grain boundary depends on the history of normal traction as well as the effective stress and creep strain of the adjacent power-law-creeping grains. In section 4.4, we studied a special case where an infinite grain boundary between two infinite power law creeping material is subjected to a constant separation rate v and found that the traction along this boundary goes to zero as the damage parameter ω ($\omega = a/b$) approaches 1. In addition, our analysis showed that the normal traction along the grain boundary can become very large at fast

loading rate or low cavity concentration. These high stresses can facilitate the decohesion of an impurity embrittled grain boundary facet.

The previous rate dependent cohesive zone model can be extended to incorporate grain boundary embrittlement. Specifically, we propose that the total grain boundary separation consists of contributions from grain boundary cavitation and from interface embrittlement, i.e.,

$$\delta_{\mathrm{n}} = \delta(a,b) + \delta_{\mathrm{b}}(\sigma_{\mathrm{n}}) H(\sigma_{\mathrm{n}} - \sigma^{*}) \tag{5.11}$$

$\delta(a,b)$ is the grain boundary separation due to cavity nucleation and growth. The additional term $\delta_{\mathrm{b}}(\sigma_{\mathrm{n}})$ is the grain boundary separation due to grain boundary embrittlement. $\delta_{\mathrm{b}}(\sigma_{\mathrm{n}})$ is non-zero if the normal grain boundary stress exceeds a threshold value σ^{*}. σ^{*} is interpreted as the critical normal stress to decohere the interface. Specifically, the interface will not decohere in a brittle fashion as long as $\sigma_{\mathrm{n}} < \sigma^{*}$, that is,

$$\delta_{\mathrm{b}} = 0 \qquad \sigma_{\mathrm{n}} < \sigma^{*} \tag{5.12}$$

Once σ_{n} reaches σ^{*}, decohesion due to embrittlement occurs and $\delta_{\mathrm{b}} > 0$, in this regime, we assume

$$\delta_{\mathrm{b}} = -\delta^{*} \ln\left(\sigma_{\mathrm{n}} / \sigma^{*}\right) \tag{5.13}$$

or

$$\sigma_{\mathrm{n}} = \sigma^{*} e^{-\delta_{\mathrm{b}}/\delta^{*}} \tag{5.14}$$

Equation (5.14) indicates the normal traction decays exponentially as a grain boundary separates due to interface embrittlement (see Figure 5.1). Equations (5.13) and (5.14) can be motivated by imagining a situation where there are no voids on the grain boundary so that $\delta_{\mathrm{n}} = \delta_{\mathrm{b}}$. For this case, the work to decohere a unit area of the grain boundary is

$$G_{\mathrm{c}} = \int_{0}^{\infty} \sigma^{*} e^{-\delta_{\mathrm{n}}/\delta^{*}} d\delta_{\mathrm{n}} = \sigma^{*}\delta^{*} \tag{5.15}$$

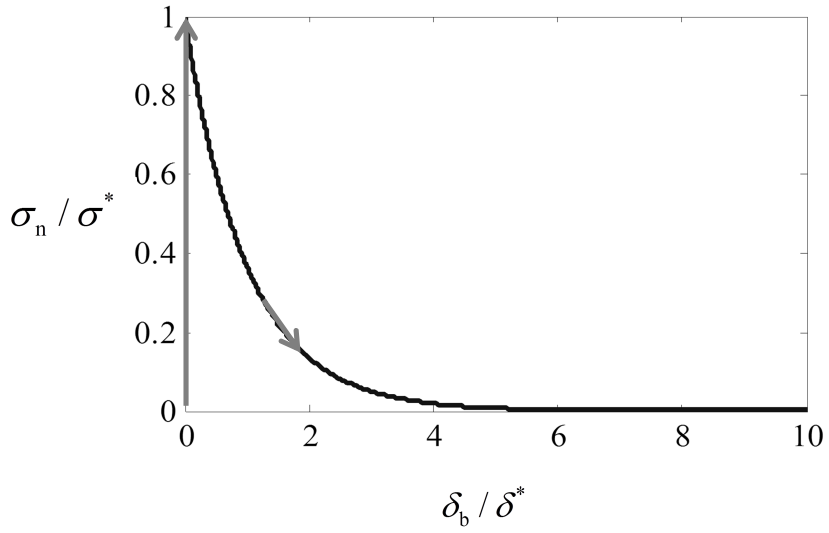

Figure 5.1 Traction-separation relation for grain boundary embrittlement model

Equation (5.15) implies $\delta^* = G_c / \sigma^*$.

A simple way to understand the extended cohesive zone model is to subject an infinite grain boundary separated by two infinite power law creeping to a constant separation rate, that is , $\delta_n = vt + \delta_0$. According to our previously analysis (see section 4.4), the initial normal traction is infinite when δ_0 becomes very small (e.g. very large initial void spacing or no cavities) or when $v \to \infty$. However, the additional term δ_b in the extended model (Equation(5.11)) would eliminate this possibility since the grain boundary cannot support a normal stress greater than σ^*. Of course, new cavities can still nucleate on such an interface (since nucleation condition is most likely to be satisfied at large normal traction) which will give rise to a non-zero δ. As a result, grain boundary cavitation and interface embrittlement both contribute to the total grain boundary separation δ_n.

A qualitative analysis of the extended model is carried out below. Using the same normalization as in section 4.3,

$$\begin{aligned} &\bar{\sigma} = \frac{\sigma}{\Sigma_0}, \bar{t} = \frac{t}{t_c}, \bar{N} = \frac{N}{N_I}, \bar{F}_n = \frac{F_n}{N_I}, \bar{a} = \frac{a}{a_0}, \\ &\bar{b} = \frac{b}{b_0}, \bar{V} = \frac{V}{V_0}, \bar{\delta} = \frac{\delta}{\delta_0}, \bar{L} = \frac{L}{a_0}, \bar{u}_s = \frac{u_s}{R_I} \end{aligned} \tag{5.16}$$

where t_c is the characteristic time given by $1/B\Sigma_0^n$, B is the power law creep coefficient , $2R_I$ is the typical width of a grain boundary facet, N_I is the initial cavity density given by $40/\pi R_I^2$, a_0, $2b_0$, V_0 are the initial cavity radius, spacing and volume respectively, δ_0 is the initial separation of the grain boundary due to preexisting voids given by $V_0 / \pi b_0^2$.

The relevant dimensionless parameters in the constant separation test are

$$\left\{ S_{thr}, \omega_0 = \frac{a_0}{b_0}, \lambda_2 = \frac{3Dt_c\Sigma_0}{a_0^3 h(\psi)}, \lambda_3 = \frac{vt_c}{\delta_0}, \bar{\sigma}^* = \frac{\sigma^*}{\Sigma_0}, \bar{\delta}^* = \frac{\delta^*}{\delta_0} \right\} \tag{5.17}$$

In the following, all normalized quantities are labeled with a bar on top. Following the same line of analysis as in section 4.4, the normalized grain boundary separation $\bar{\delta}_{\mathrm{n}}$ is

$$\lambda_3 \bar{t} + 1 = \bar{a}^3 \left[1 + \frac{H(\bar{t} - \bar{t}_{\mathrm{N}})}{S_{\mathrm{thr}}} \int_{\bar{t}_{\mathrm{N}}}^{\bar{t}} \bar{\sigma}^{n+2}(\tau) d\tau \right] - \bar{\delta}^* \ln\left(\bar{\sigma} / \bar{\sigma}^*\right) H(\bar{\sigma} - \bar{\sigma}^*) \qquad (5.18)$$

where $\bar{t}_{\mathrm{N}}$ is the time when nucleation occurs. The initial stress $\bar{\sigma}_{\mathrm{ini}} = \bar{\sigma}\left(\bar{t} = 0\right)$ can be determined by

$$\left(\lambda_3 \bar{t} + 1\right) \alpha_{\mathrm{n}} \bar{\sigma}^n + \frac{\lambda_2}{q(f)} \bar{\sigma} = \lambda_3 \qquad (5.19)$$

$$\alpha_{\mathrm{n}} = \frac{1}{2} \left[\frac{3}{2n} + \frac{(n-1)(n+0.4319)}{n^2} \right]^n \qquad (5.20)$$

There are two possibilities:

(1) If $\bar{\sigma}_{\mathrm{ini}} < \bar{\sigma}^*$, interface embrittlement will not be activated since the normal traction $\sigma(t)$ decreases monotonically from $\bar{\sigma}_{\mathrm{ini}}$ to zero as damage parameter $\omega = a / b$ increases from ω_0 to 1. In this scenario, only grain boundary cavity nucleation and growth contributes to the grain boundary separation. We have studied this in previous analysis (section 4.4). It should be noted that this situation will occur for very large decohesion stress.

(2) If $\bar{\sigma}_{\mathrm{ini}} > \bar{\sigma}^*$, $\sigma(t)$ will drop to σ^* instantaneously and interface embrittlement occurs. In this scenario, $\sigma(t)$ is expected to relax to zero much faster than in scenario (1) given the exponential decay of $\sigma(t)$ as $\bar{\delta}_{\mathrm{b}}$ increases. As a consequence, interface embrittlement would slow down the cavity growth rate since cavities grow under normal tension. These predictions are verified in the numerical example shown in Figure 5.2. The six dimensionless parameters used in the analysis are

$$\omega_0 = 4.2 \times 10^{-3}, \frac{1}{S_{\mathrm{thr}}} = 7.465 \times 10^3, \lambda_2 = 2.037 \times 10^6, \lambda_3 = 5 \times 10^4, \bar{\sigma}^* = 0.4487, \bar{\delta}^* = 400 \qquad (5.21)$$

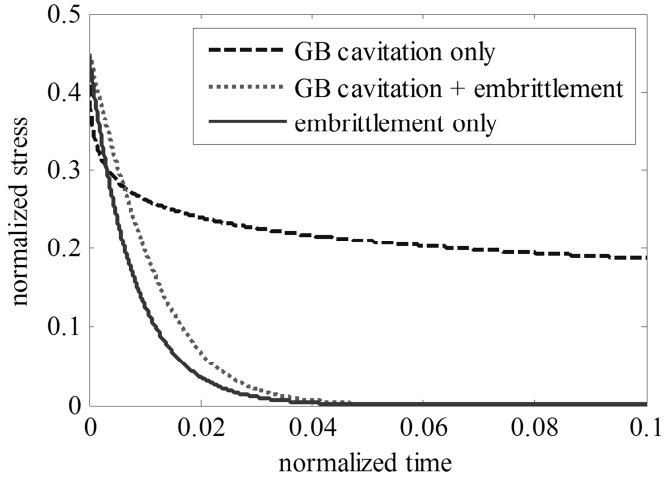

(a)

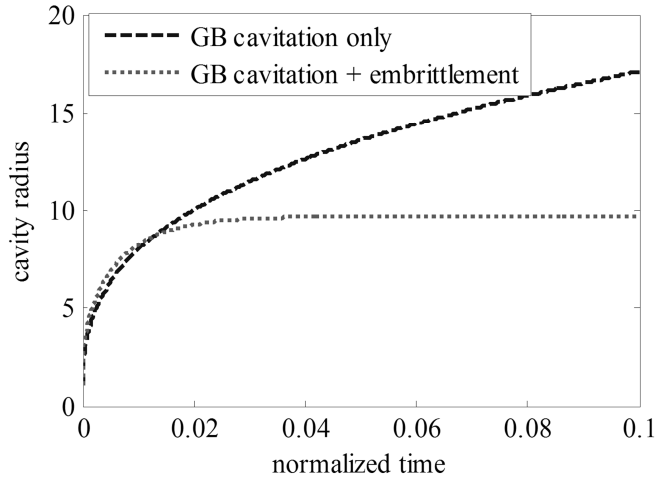

(b)

Figure 5.2 Numerical results for constant separation test. (a) Normal traction versus time (b) Cavity radius versus time

As shown in Figure 5.2(a), the normal traction $\sigma(t)$ relaxation due to grain boundary embrittlement is very prominent and it vanishes at a much earlier time compared to the case where only grain boundary cavitation occurs. This leads to a constant cavity radius (zero cavity growth rate) at long times (see Figure 5.2(b)).

5.4 Finite Element Model

In this section, a two dimensional microstructure consisting of random sized grains loaded in plane strain is used to study the grain boundary damage evolution (see Figure 5.3(a)). Specifically, grains are modeled as elastic-power law creeping material using ABAQUS user subroutine UMAT (ABAQUS 2008). Grain boundary separation and sliding are modeled using cohesive zone elements. The previous ABAQUS user subroutine UEL in section 4.5 is modified to allow for grain boundary decohesion due to embrittlement where normal traction along grain boundaries decrease exponentially with separation.

All material parameters are assigned according to Table 5.1. Two new independent material parameters are assigned for the extended cohesive zone model: the work of cohesion G_c and the decohesion stress σ^* ,

$$G_c = 1 \text{ J/m}^2, \sigma^* = 63.4 \text{ MPa}, \delta^* = G_c / \sigma^* = 0.016 \text{ μm} \tag{5.22}$$

The numbers chosen for our simulation are broadly consistent with previous studies (Deng et al. 2005; Goodwin et al. 1988). G_c is chosen as a typical number for specific energy per unit area of a grain boundary facet in Nickel alloys (Chuang et al. 1979a; Hirth and Lothe 1978). σ^* is chosen based on a typical cavity nucleation stress observed experimentally for high temperature alloys (Riedel 1987). Once these material parameters are assigned, the normalized parameters are specified.

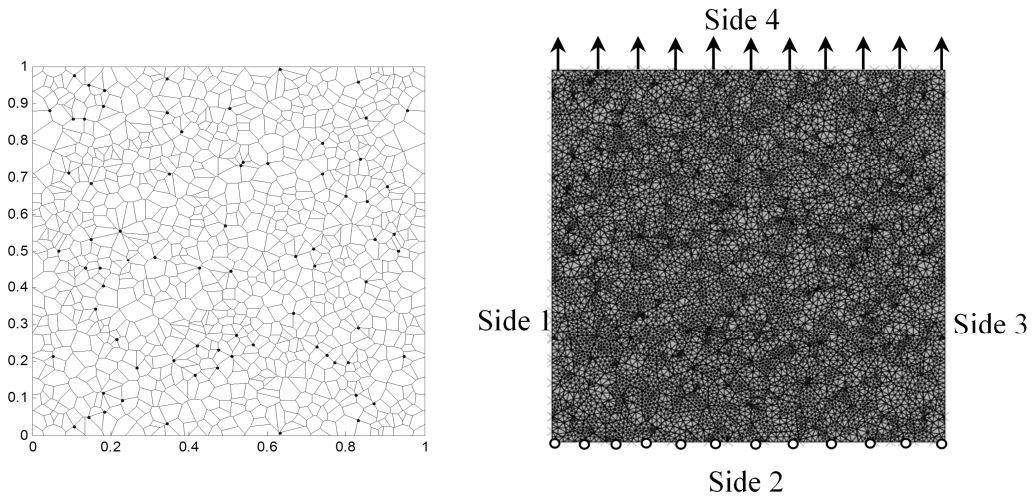

(a) (b)

Figure 5.3 (a) 2D microstructures with 1000 random sized grains. (b) Boundary condition for uniaxial tension test

Table 5.1 Material parameters for power law creep, grain boundary sliding, grain boundary cavity nucleation and growth, interface embrittlement

Parameters	Values
Reference stress Σ_0	300 MPa
Creep Exponent n	5
Elastic power law creep coefficient B	4.115×10^{-20} $\mathrm{MPa^{-5}s^{-1}}$
Elastic Modulus E	189 GPa
Poisson's ratio ν	0.285
Grain boundary diffusivity parameter D	$7.238\times10^{-19}\,\mathrm{MPa^{-1}\cdot s^{-1}\cdot mm^{3}}$
Grain boundary viscosity η_b	$1\times10^{11}\,\mathrm{MPa\cdot s\cdot mm^{-1}}$
Initial cavity radius a_0	3.35×10^{-5} mm
Initial half cavity spacing b_0	1.6×10^{-2} mm
Grain boundary facet width $2R_I$	0.1 mm
Initial cavity density N_I	$40/\pi R_I^2$ $\mathrm{mm^{-2}}$
Nucleation activity F_n	$6\times10^{2}\,N_I$ $\mathrm{mm^{-2}}$
Characteristic time τ_c	10^7 s
Decohesion stress σ^*	63.4 MPa
Work of cohesion, G_c	1 $\mathrm{J/m^2}$

Use the same normalization in (5.16), the dimensionless parameters used in the finite element simulation are:

$$\left\{ n, \bar{E} = \frac{E}{\Sigma_0}, \upsilon, S_{\text{thr}}, \omega_0 = \frac{a_0}{b_0}, \lambda_1 = \frac{\eta_b R_I}{\Sigma_0 t_c}, \lambda_2 = \frac{3Dt_c\Sigma_0}{a_0^3 h(\psi)}, \bar{\sigma}^* = \frac{\sigma^*}{\Sigma_0}, \bar{\delta}^* = \frac{\delta^*}{\delta_0} \right\} \quad (5.23)$$

λ_1 is a ratio of the creep strain due to power law creep over the strain caused by grain boundary sliding. For example, $\lambda_1 \to 0$ corresponds to free sliding at the grain boundary, whereas $\lambda_1 \to \infty$ means no grain boundary sliding is allowed. λ_2 is the ratio of cavity growth rate due to diffusion over that due to power law creep. A small λ_2 indicates that cavity growth is controlled by power law creep and a large λ_2 indicates that cavity growth is controlled by diffusion. ω_0 is the square root of the initial area fraction occupied by voids and can be considered as an initial damage parameter. S_{thr} controls the ease of cavity nucleation. Finally, $\bar{\sigma}^*$ is the normalized decohesion stress and $\bar{G}_c = \bar{\sigma}^* \bar{\delta}^*$ represents the amount of energy needed to completely fail a unit area of a grain boundary with no ductility.

We carry out uniaxial tension tests on the two dimensional finite element model shown in Figure 5.3(b). The boundary conditions are applied as follows: Side 2 of the RVE is constrained in the vertical direction. Both side 1 and side 3 of the RVE are traction free, a normal surface traction $\bar{\sigma}_a = 0.1$ is applied on side 4.

5.5 Results and Analysis

In this section, we present uniaxial plane strain creep test results for power law creeping grains of random sizes with sliding and cavitating boundaries where interface embrittlement is incorporated into grain boundary separation law. We study creep rupture behavior of the microstructure and the interaction of interface embrittlement and grain boundary cavitation. We compare simulation results with the previous cohesive zone model (section 4.7) where grain boundary separation is determined by

Table 5.2 Varying dimensionless parameters for creep rupture simulations

Case	λ_1	λ_2
Case 1	1.67	2.517×10^5
Case 2	16.7	2.517×10^5
Case 3	16.7	2.517×10^4

cavity nucleation and growth. Comparisons are carried out by assigning the same set of grain boundary sliding and cavitation parameters in both simulations. Specifically, we vary λ_1 and λ_2 while fixing the rest of the parameters (see(5.23)), $\omega_0 = 4.2\times10^{-3}$, $1/S_{\text{thr}} = 6\times10^{2}, \bar{\sigma}^{*} = 0.21, \bar{\delta}^{*} = 0.03$. The parameters λ_1 and λ_2 used in our simulations are summarized in Table 5.2. Briefly, it is easier for grain boundaries to slide in case 1 (small λ_1) compared to the other two cases . Case 3 has the slowest cavity growth rate among the three cases (small λ_2).

The inelastic normal strain ($\varepsilon_{22}^{\text{I}}$) of the RVE versus time is shown in Figure 5.4. The symbols indicate the results where only grain boundary cavitation is allowed for interface separation. The dash lines are the results obtained using the extended cohesive zone model. The straight line with the smallest inelastic strain rate is the result of a pure elastic power law creeping material in the absence of grain boundary sliding, separation and embrittlement. As expected, damage mechanisms (grain boundary sliding, grain boundary cavitation, interface embrittlement) greatly enhance the inelastic strain rate. An interesting result is that the symbols and the dash lines for all three cases lie on top of each other, indicating that for the parameters used in these simulations, the inelastic strain rate enhancement due to grain boundary cavitation and embrittlement is almost the same as the enhancement due to grain boundary cavitation alone. This implies that for this special case, the additional damage caused by interface embrittlement is almost equal to the reduction in damage caused by grain boundary cavitation. In appendix 5.1, we present results where the inelastic strain rates of the RVE are quite different for cases with and without grain boundary embrittlement.

To study how grain boundary cavitation and grain boundary sliding affect interface embrittlement, we plot the ratio of grain boundary elements with interface embrittlement over the total number of grain boundary elements versus time for the three cases in Figure 5.5. As shown in the figure, interface embrittlement is activated

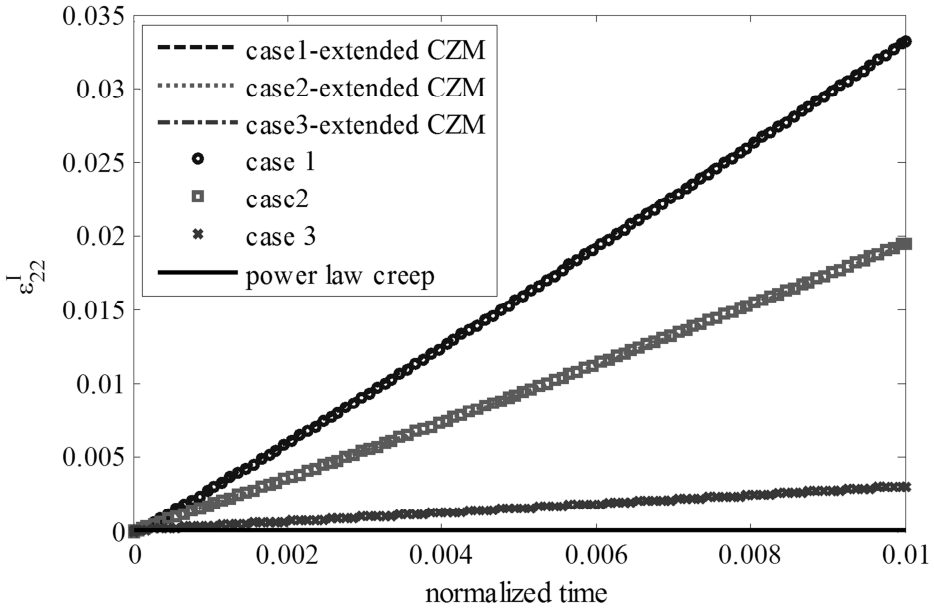

Figure 5.4 Inelastic strain ε_{22}^{I} versus time for uniaxial tension test. The symbols are for CZM with grain boundary cavitation. The dash lines are for the extended CZM. The straight line (practically horizontal) is for a pure elastic power law creeping material.

at approximately 35% of the grain boundary elements in case 3, compare to 12% and 5% in case 1 and case 2 respectively. Recall the interface embrittlement occurs when the normal traction along a grain boundary exceeds the maximum stress the grain boundary can support (σ^*). It is expected that grain boundary sliding would cause stress concentration at triple junctions. This will lead to a higher percentage of grain boundary elements with interface embrittlement in case 1 compared to case 2 due to a smaller λ_1 (more grain boundary sliding). Grain boundary cavitation tends to relax the normal traction along a grain boundary. Hence, more grain boundaries are embrittled in case 3 since a smaller λ_2 (slower grain boundary cavity growth rate) is assigned to this case compare to the other two.

Not all embrittled grain boundaries will fail. A noticeable feature in Figure 5.5 is that interface embrittlement occurs at an early stage of the loading in case 1. This indicates the effect of rate-dependent deformation on embrittlement (even though the model for embrittlement is rate independent). For example, case 1 and case 2 have the same grain boundary diffusion parameter λ_2 but case 1 has a higher grain boundary sliding rate. Based on the analysis in section 4.7, grain boundary sliding facilitate cavity growth rate in an uniaxial tension test. Hence, we expect the faster cavity growth rate in case 1 leads to faster stress relaxation, this will cause embrittlement to stop at a shorter time despite there is more embrittled grain boundaries in case 1. Consistent with this explanation, the difference between case 3 and case 1 is more substantial since stress relaxation occurs even faster due to faster cavity growth and sliding in case 1.

To study the interplay between grain boundary cavitation and embrittlement on a grain boundary, we plot the traction ($\bar{\sigma}_n$) versus separation ($\bar{\delta}_n$) curve (see Figure 5.6) in case 2 for a typical grain boundary element, #24531. Similar results are obtained for case 1 and case 3, hence they are not presented here. The solid line is the

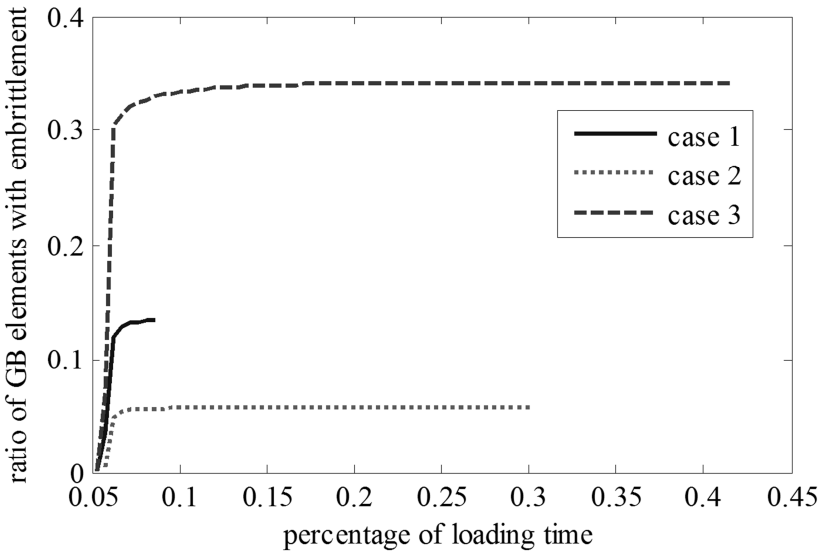

Figure 5.5 Ratio of GB elements with interface embrittlement over the total number of GB elements versus time for the three different cases listed in Table 5.2 .

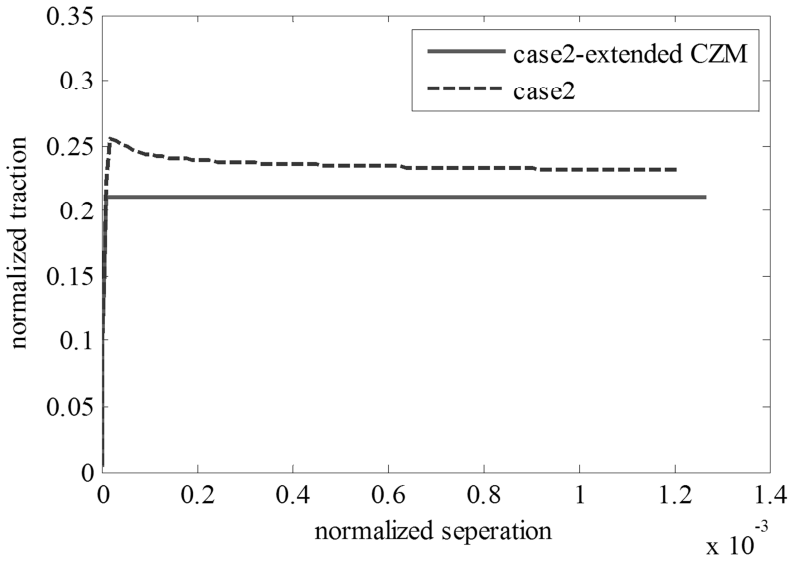

Figure 5.6 Normal traction versus separation for grain boundary element 24531 for case 2 with $\lambda_1 = 16.7, \lambda_2 = 2.157 \times 10^5$.

extended cohesive zone model whereas the dash line is for the cohesive zone model without embrittlement. As expected, $\bar{\sigma}_{\mathrm{n}}$ is reduced by interface embrittlement compared to the case where only grain boundary cavitation occurs. However, the grain boundary separation $\bar{\delta}_{\mathrm{n}} = \bar{\delta} + \bar{\delta}_{\mathrm{b}}$ in the extended cohesive zone model only increases slightly due to embrittlement. Specifically, grain boundary separation contribution from embrittlement is very small, $\delta_{\mathrm{b}} / \delta_{\mathrm{n}} \approx 0.02$. Therefore, the normal traction remains approximately constant on this interface. This is consistent with the prediction based on (5.14).

Plots of the damage parameter $\omega = a / b$ versus grain boundary separation $\bar{\delta}_{\mathrm{n}}$ for element 24531 are presented in Figure 5.7 for all three cases. Notice that the damage due to grain boundary cavitation is reduced by interface embrittlement, which agrees with the analysis based on Figure 5.4. Furthermore, it is consistent with the experimental observation that impurities along grain boundaries reduce the grain boundary diffusion and decelerate diffusive cavity growth (Schneibel et al. 1982).

5.6 Summary and Discussion

We have developed a 2D finite element model to study the effect of grain boundary sliding, cavitation and decohesion on creep deformation of a RVE consisting of random size power-law creeping grains. Grain boundary sliding and separation is incorporated into a cohesive zone model. The previous cohesive zone model in Chapter 4 which determines grain boundary separation based on cavity nucleation and growth has been extended to account for grain boundary decohesion. In this extension, grain boundary decohesion is modeled by assuming that when the normal traction on a grain boundary exceeds the decohesion stress, it decreases exponentially with separation.

Our results show that grain boundary cavitation and interface embrittlement are

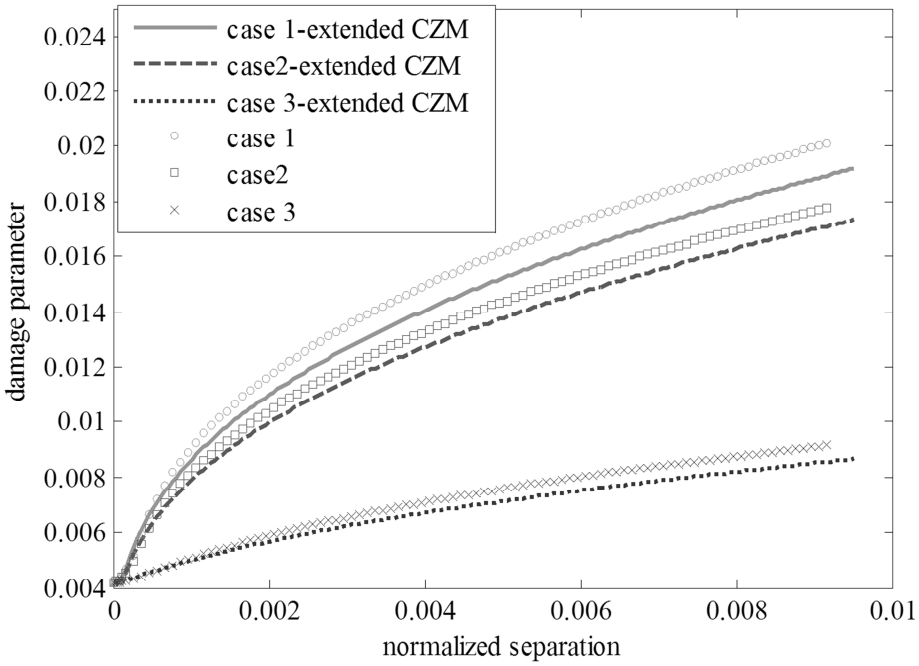

Figure 5.7 Grain boundary cavitation damage parameter versus time for grain boundary element 24531. The symbols are for CZM with grain boundary cavitation. The lines are for the extended CZM.

two competing mechanisms for creep failure, in the sense that stress relaxation due to cavitation can reduce local stresses leading to retardation of decohesion. The proposed unified model for grain boundary separation can be viewed as a first step in a more comprehensive study of creep rupture.

Appendix 5.1 Grain Boundary Embrittlement Dominated Creep Damage

In this section, we present uniaxial tension test results where the inelastic strain rates of the RVE are greatly enhanced by interface embrittlement. The following dimensionless parameters are used to carry out simulations shown in Figure 5.8

$$\omega_0 = 4.2\times10^{-3}, 1/S_{\text{thr}} = 6\times10^{2}, \bar{\sigma}^{*} = 0.21, \bar{\delta}^{*} = 0.03, \lambda_1 = 1.67, \lambda_2 = 2.157\times10^{3} \quad (5.24)$$

Note that compare to Table 5.2, the parameters used in this section are assigned in a way such that the grain boundary separation is mainly caused by interface embrittlement. As shown in Figure 5.8, the inelastic strain rate is much higher when grain boundary embrittlement is incorporated into the CZM compared to the case where only grain boundary cavitation is accounted for. This indicates the contribution to creep damage along grain boundaries is mainly from interface embrittlement.

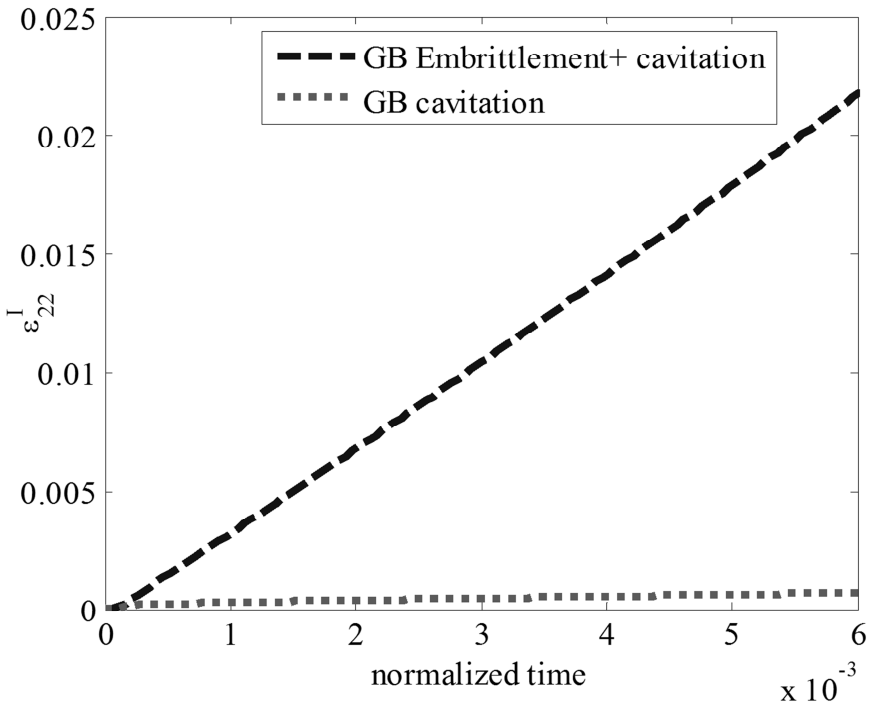

Figure 5.8 Inelastic strain ε_{22}^{I} versus time for uniaxial tension test using parameters assigned in (5.24)

REFERENCES

ABAQUS (2008) version 6.8-3. Dassault Systemes SIMULIA Corp.

Budiansky B, Hutchinson J, Slutsky S (1982) Void growth and collapse in viscous solids. Mech Solids:13-45

Chuang T, Kagawa K, Rice J, Sills L (1979) Non-equilibrium models for diffusive cavitation of grain interfaces. Acta Metall 27:265-284

Deng X, Ma F, Sutton MA (2005) A damage mechanics model for creep and oxygen embrittlement in metals. Int J of Damage Mech 14:101-126

Dyson B (1976) Constraints on diffusional cavity growth rates. Met Sci 10:349-353

Eberhart ME, Latanision R, Johnson K (1985) Overview no. 44: The chemistry of fracture: A basis for analysis. Acta Metall 33:1769-1783

Edwards B, Bishop H, Riviere J, Eyre B (1976) An AES study of temper embrittlement in a low alloy steel. Acta Metall 24:957-967

Goodwin L, Needs R, Heine V (1988) Effect of impurity bonding on grain-boundary embrittlement. Phys Rev Lett 60:2050-2053

Hirth JP, Lothe J (1978) Theory of dislocations. McGraw-Hill, New York

Hirth JP, Rice J (1980) On the thermodynamics of adsorption at interfaces as it influences decohesion. Metall Mater Trans A 11:1501-1511

McMahon C, Marchut L (1978) Solute segregation in iron‐based alloys J Vac Sci Technol 15:450-466

Messmer R, Briant C (1982) The role of chemical bonding in grain boundary embrittlement. Acta Metall 30:457-467

Mishin Y, Sofronis P, Bassani J (2002) Thermodynamic and kinetic aspects of interfacial decohesion. Acta materialia 50:3609-3622

Needleman A, Rice J (1980) Plastic creep flow effects in the diffusive cavitation of grain boundaries. Acta Metall 28:1315-1332

Onck P, Van der Giessen E (1998) Growth of an initially sharp crack by grain boundary cavitation. J Mech Phys Solids 47:99-139

Raj R, Ashby M (1975) Intergranular fracture at elevated temperature. Acta Metall 23:653-666

Rice J, Thompson A, Bernstein I (1976) Effect of hydrogen on behavior of materials. AIME, New York:455-466

Riedel H (1987) Fracture at high temperatures. Springer-Verlag,

Schneibel J, White C, Padgett R (1982) Influence of traces of Sb and Zr on creep and creep fracture of Ni-20% Cr. Oak Ridge National Lab., TN (USA),

Sham TL, Needleman A (1983) Effects of triaxial stressing on creep cavitation of grain boundaries. Acta Metall 31:919-926

Troiano AR (1960) The role of hydrogen and other interstitials in the mechanical behavior of metals. trans ASM 52:54-80

Tvergaard V (1984) On the creep constrained diffusive cavitation of grain boundary facets. J Mech Phys Solids 32:373-393

Woodford D (1981) Environmental damage of a cast nickel base superalloy. Metall Mater Trans A 12:299-308

Woodford D, Bricknell R (1981) Air embrittlement of a cobalt-base superalloy. Metall Mater Trans A 12:1945-1949

CHAPTER 6

CONCLUSIONS AND FUTURE WORK

In Chapter 2, we use a dynamical system approach to study the creep fatigue behavior of a viscoplastic material using a constitutive model proposed by Chaboche (1989). We establish a condition for the existence of a periodic solution in a cyclic loading test. We study the dependence of the accumulated inelastic strain per cycle on the material and loading parameters such as stress ratio and yield stress. Our results show that low yield stress and large valley stress reduce ratcheting.

In Chapter 3, the asymptotic stress and strain field near the tip of a plane strain Mode I stationary crack in a viscoplastic material (Chaboche 1989) are investigated. We find that within the small scale creep regime, the near tip stress field of the viscoplastic material has the same HRR (Hutchinson 1968; Rice and Rosengren 1968) singularity as an elastic power law creep material. However, the amplitude of the HRR field vanishes at long times. We study the time dependent behavior of these crack tip fields under cyclic loading. The strain accumulated per cycle is found to decrease with stress ratio.

In Chapter 4, we carry out finite element simulations on a two dimensional representative volume element where the grains are modeled as an elastic-power law creeping material, and grain boundary behavior is incorporated into a cohesive zone model where they can slide and separate due to cavity nucleation and growth. For the grain boundary cavitation model, we show analytically that the normal traction along a grain boundary vanishes when the damage parameter approaches 1 if it is separated at a constant rate. Our relaxation results show that most of the imposed strain is accommodated by the separation and sliding of the grain boundaries and such creep damage mechanisms cause much faster stress relaxation. We also find that overall

strain rate of a microstructure is enhanced by grain boundary cavitation and grain boundary sliding significantly during uniaxial creep test.

In Chapter 5, we incorporate impurity-induced interface embrittlement into grain boundary separation by extending the cohesive zone model in Chapter 4. We study the interaction of embrittlement and deformation caused by creep, cavities growth and grain boundary sliding. Our results show that stress concentration caused by grain boundary sliding leads to more grain boundary embrittlement, stress relaxation due to cavity growth and creep inhibit interface embrittlement, interface embrittlement slows down the cavity growth rate.

Much more work needs to be done in order to establish a reliable computational model for creep rupture. To analyze engineering structures, it is necessary to extend the 2D finite element model in this work to 3D models. As pointed out by Westwood et al (2004), the cavity growth model used in Chapter 4 and 5 tends to overestimate the damage caused by cavity diffusion. Modification on the current grain boundary cavitation model is necessary for more accurate prediction of creep rupture life. More realistic creep models such as crystal visco-plasticity based models should be implemented for loading histories that are non-monotonic. Recall that the cavity growth model in this work is based on elastic-power-law creeping grains. Some aspects of the micromechanical models for cavity growth need to be modified if crystal visco-plasticity model are used to describe grain deformation. Also, with enough computational power, one can model discrete cavities on grain boundaries and study their growth and interaction.

Many creep damage mechanisms are not well understood at the present. The only grain boundary sliding model we are aware of that can be readily used for computation modeling is based on a result of Raj and Ashy (1971) where there is very limited experimental data. The current theories of cavity nucleation do not match

experimental data well (see Chapter 5 in Riedel (1987)'s book and the references within). For example, there is a large gap between the observed and calculated critical nucleation stress. Therefore an empirical description of cavity nucleation is adopted in this dissertation. The role of impurity segregation in cavity nucleation needs to be modeled. It has been known for a long time that impurities along grain boundaries could reduce the grain boundary diffusion (Schneibel et al. 1982) and increase the cavity nucleation rate (Tipler and Hopkins 1976; Thomas and Gibbons 1979). These mechanisms need to be quantified and incorporated into a creep damage model in future works.

REFERENCES

Chaboche JL (1989) Constitutive equations for cyclic plasticity and cyclic viscoplasticity. Int J Plast 5:247-302

Hutchinson J (1968) Singular behaviour at the end of a tensile crack in a hardening material. J Mech Phys Solids 16:13-31

Raj R, Ashby M (1971) On grain boundary sliding and diffusional creep. Metall Mater Trans B 2:1113-1127

Rice J, Rosengren G (1968) Plane strain deformation near a crack tip in a power-law hardening material. J Mech Phys Solids 16:1-12

Riedel H (1987) Fracture at high temperatures. Springer-Verlag, Berlin Heidelberg

Schneibel J, White C, Padgett R (1982) Influence of traces of Sb and Zr on creep and creep fracture of Ni-20% Cr. Oak Ridge National Lab., TN (USA),

Thomas G, Gibbons T (1979) Influence of Trace Elements on Creep and Stress-Rupture Properties of Nimonic 105. Met Technol 6:95-101

Tipler H, Hopkins B (1976) The creep cavitation of commercial and high-purity Cr-Mo-V steels. Met Sci 10:47-56

Westwood C, Pan J, Crocombe A (2004) Nucleation, growth and coalescence of multiple cavities at a grain-boundary. Eur J Mech A-Solid 23:579-597